pennsylvania
DEPARTMENT OF TRANSPORTATION

Superpave In-Situ Stress/Strain Investigation – Phase II

FINAL REPORT
Vol. IV: Mechanistic Analysis and Implementation

May 2009

By Shelley M. Stoffels, Mansour Solaimanian, and Hao Yin

The Thomas D. Larson
Pennsylvania Transportation Institute

PENNSTATE
1855

COMMONWEALTH OF PENNSYLVANIA
DEPARTMENT OF TRANSPORTATION

CONTRACT No. 999012
PROJECT No. HA2006-02

Technical Report Documentation Page

1. Report No. FHWA-PA-2009-009-999012 HA 2006-02	**2. Government Accession No.**	**3. Recipient's Catalog No.**
4. Title and Subtitle SuperPave In-Situ Stress/Strain Investigation, Phase II Volume IV: Mechanistic Analysis and Implementation		**5. Report Date** May 2009 **6. Performing Organization Code**
7. Author(s) Shelley M. Stoffels, Mansour Solaimanian, and Hao Yin		**8. Performing Organization Report No.** PTI 2009-19
9. Performing Organization Name and Address The Thomas D. Larson Pennsylvania Transportation Institute Transportation Research Building The Pennsylvania State University University Park, PA 16802-4710		**10. Work Unit No. (TRAIS)** **11. Contract or Grant No. 999012** Project HA2006-02
12. Sponsoring Agency Name and Address The Pennsylvania Department of Transportation Bureau of Planning and Research Commonwealth Keystone Building 400 North Street, 6th Floor Harrisburg, PA 17120-0064		**13. Type of Report and Period Covered** Final Report 6/23/2006 – 11/30/2008 **14. Sponsoring Agency Code**
15. Supplementary Notes COTR: Mr. Michael Long, johlong@state.pa.us		

16. Abstract

The SISSI data were utilized in the Mechanistic-Empirical Pavement Design Guide (MEPDG), and the predicted condition parameters were compared to those measured in the field. Overall, it was found that the MEPDG only made somewhat reasonable predictions for rutting. It is therefore essential to perform local calibration. The SISSI data provide a valuable source of both response and performance data for that purpose. In order to further understand the sources of differences between measured and predicted performance, it is important to evaluate the differences in mechanistic responses. Therefore, independent mechanistic analysis was conducted in order to compare the responses from finite element analysis to those measured from the instrumentation in the field. In order to correct the finite element responses to correspond to field conditions under a variety of environmental and loading conditions, a site-specific procedure was developed to extrapolate the results. Finite element analysis was also utilized to model loading with the falling weight deflectometer. A comparison of the responses from embedded instrumentation devices during the FWD loading was also made. For surface deflections, the average prediction errors were 9 and 12 percent when using backcalculated and laboratory AC moduli, respectively. For the strain and stress responses, the predicted responses consistently exceeded the measured responses, with a prediction error of 30 to 50 percent. Finally, parametric studies were conducted to examine possible sources of error in the SISSI experiment. The variation of loading pulse with depth was examined and correction procedures were utilized. An additional concern was that the strain gages themselves might alter the pavement structure and affect the overall response. Therefore, detailed finite element analysis was performed to examine the potential magnitude of the strain gage effects. It was found that the strain gages might result in an error of up to about 80 percent, depending upon other conditions.
As the Pennsylvania Department of Transportation moves to adopt and implement the MEPDG, these analyses provide a basis for utilizing the SISSI data in its understanding and calibration. The present report is one of four volumes, Volume I: Summary Report; Volume II, Materials Characterization; Volume III: Field Data Collection and Summary; Volume IV: Mechanistic Analysis and Implementation.

17. Key Words SISSI, pavement, asphalt, instrumentation, finite element, rutting, mechanistic, performance, prediction, FWD		**18. Distribution Statement** No restrictions. This document is available from the National Technical Information Service, Springfield, VA 22161	
19. Security Classif. (of this report) Unclassified	**20. Security Classif. (of this page)** Unclassified	**21. No. of Pages** 124	**22. Price**

Form DOT F 1700.7 **(8-72)** **Reproduction of completed page authorized**

This work was sponsored by the Pennsylvania Department of Transportation and the U.S. Department of Transportation, Federal Highway Administration. The contents of this report reflect the views of the authors, who are responsible for the facts and the accuracy of the data presented herein. The contents do not necessarily reflect the official views or policies of the Federal Highway Administration, the U.S. Department of Transportation, or the Commonwealth of Pennsylvania at the time of publication. This report does not constitute a standard, specification, or regulation.

TABLE OF CONTENTS

LIST OF FIGURES

LIST OF TABLES

CHAPTER 1: INTRODUCTION

In 2001, the Pennsylvania Department of Transportation (PennDOT) sponsored a 5-year research project for the full evaluation of Superpave called the Superpave In-Situ Stress/Strain Investigation (SISSI) to produce data needed for calibration and validation of asphalt pavement performance prediction models. The first phase (Phase I) of the SISSI project was completed in May 2006. A second phase (Phase II) was then initiated to continue data collection from the installed instrumentation, monitoring of pavement condition, laboratory and field testing for materials characterization, and analysis of the data.

This report is one of four volumes of the final report for Phase II of the SISSI project. Separate volumes have been prepared for an overall summary, materials characterization, and field data collection for the SISSI sites. This volume documents the mechanistic analysis conducted.

Accurate pavement performance prediction is widely recognized by the pavement community as one of the most important, complex, and difficult tasks to pursue. The importance of such a goal cannot be emphasized enough because it will result in the saving of millions of dollars. Proper selection of pavement materials and layer thicknesses can be optimized using performance-based specifications. The basic requirement is the availability of an accurate pavement performance prediction methodology.

Many highway agencies use the current AASHTO Guide for Design of Pavement Structures to design their pavement systems. The limitation inherent in this method is the empirical nature of the decision process, which was derived from the road test conducted almost 45 years ago in Ottawa, Illinois. The AASHTO design method established a relationship between the number of load cycles, pavement structural capacity, and performance, which were measured in terms of serviceability. The concept of serviceability was introduced in the AASHTO method as an indirect measure of the pavement's ride quality. The serviceability index is based on surface distresses commonly found in pavements. The major advantage of these methods is the mathematical simplicity that does not require advanced computational capabilities or extensive material characterization for the design of pavement structures; however, with all of these advantages, the empirical methods are not without some serious limitations. The major limitation is that they cannot provide accurate predictions for material, environment, and traffic conditions that differ from those for which the models were originally developed. Mechanistic methods generally use the linear-elastic theory of mechanics to compute structural responses in combination with empirical models to predict number of loads to failure for flexible pavements. The dilemma is that pavement materials do not exhibit the simple behavior assumed in isotropic linear-elastic theory. Nonlinearities, time and temperature dependency, and anisotropy are some examples of complicated features often observed in pavement materials. In this case, advanced modeling is required to mechanistically predict performance.

The mechanistic design procedure is based on the theories of mechanics that relate pavement structural behavior and performance to traffic loading and environmental influences. It is well understood that the pavement responses, such as the stresses and strains in the system, are directly related to the pavement layer material properties. Thus, characterization of these

materials is an important factor for the response prediction. Progress has been made in recent years on isolated pieces of the mechanistic-performance prediction problem, but the reality is that fully mechanistic methods are not yet available for practical pavement design.
The mechanistic-empirical procedure is the consolidation of the two sides. Empirical models are used to fill in the gaps that exist between the theory of mechanics and the performance of pavement structures. Simple mechanistic responses are easy to compute with assumptions and simplifications (e.g., homogeneous material, small strain analysis, and static loading as typically assumed in linear elastic theory), but they by themselves cannot be used to predict performance directly; some type of empirical model (transfer functions) is required to make the appropriate correlation (Newcomb et al. 1983, Timm and Newcomb 2003). Mechanistic-empirical methods are considered an intermediate step between empirical and fully mechanistic methods.

The newly released *Mechanistic-Empirical Pavement Design Guide* (MEPDG), based on NCHRP 1-37A (ERES 2004), has adopted a mechanistic-empirical pavement design procedure in which pavement distresses are calculated through calibrated distress prediction models based on material properties determined from laboratory tests and local traffic and climate conditions. The calibrated distress prediction models are based on the critical pavement responses mechanistically calculated by a structural model and coefficients determined through national calibration efforts using the LTPP database. A great deal of design input related to structures, materials, environment, and traffic are considered in the MEPDG in analyzing and designing a pavement. With the performance-related design concept, a pavement designer has the capability and flexibility to incorporate several design features and material properties to a certain pavement site and its conditions to meet the key distresses and smoothness performance requirements.

Parametric studies are an important step in any implementation of the MEPDG as a new pavement design standard in highway agencies. The results and conclusions are useful for developing knowledge about the design procedure, finding weaknesses and problems within the local agencies' practices that need to be addressed, and defining priorities for the implementation and calibration tasks. The objective of the sensitivity study presented in this report is to provide useful and relevant data analyses of performance prediction sensitivity to site-specific parameters of the SISSI project. Identified sensitive parameters will, therefore, be used to develop a probabilistic-based approach for performance predictions.

CHAPTER 2: OVERVIEW OF THE MEPDG

The various versions of the AASHTO Pavement Design Guide have served the pavement engineering community well for several decades. However, the low traffic volumes, dated vehicle characteristics, short test duration, narrow range of material types, single climate, and other limitations of the original AASHTO Road Test have called into question the continuing use of the empirical AASHTO Design Guide as the nation's primary pavement design procedure. These perceived deficiencies were the motivation for the development of the MEPDG. The MEPDG provides a state-of-the-practice tool for the design of new and rehabilitated pavement structures based on mechanistic-empirical principles. Because the mechanistic procedures are able to better account for climate, aging, present-day materials, and present-day vehicle loadings, variation in performance, in relation to design life, should be reduced. This capability will reduce life cycle costs significantly over an entire highway network.

The only comprehensive documentation for the MEPDG now available to the general public is the Web-based version provided by the Transportation Research Board at http://www.trb.org/mepdg/. Version 1.0 of the MEPDG software is also available for downloading from this site. In this section, a brief review on some key considerations and features in the MEPDG, focusing on flexible pavements, is provided.

General Considerations

The MEPDG considers truck traffic loadings in terms of the full axle load spectra: single, tandem, tridem, and quad axles. The equivalent single axle load (ESAL) concept is no longer used as a direct design input. The MEPDG considers the number of heavy trucks as an overall indicator of the magnitude of truck traffic loadings (FHWA class 4 and above).

Environmental conditions have a significant effect on the performance of flexible pavement. The interaction of the climatic factors with pavement materials and loading is complex. Factors such as precipitation, temperature, freeze-thaw cycles, and water table depth affect pavement and subgrade temperature and moisture content, which, in turn, directly affect the load-carrying capacity of the pavement layers and ultimately pavement performance. With available climate data from weather stations, the MEPDG uses the EICM to predict temperature and moisture within each pavement layer and the subgrade. The temperature and moisture predictions from the EICM are used to estimate material properties for the foundation and pavement layers on a semi-monthly or monthly basis throughout the design life. The frost depth is determined, and the proper moduli are estimated above and below this depth.

For the pavement structure, the surface AC layer is divided into sublayers to account for temperature and aging gradients. Asphalt aging is modeled only for the top sublayer. The largest change in stiffness due to aging occurs only in the top half-inch, and the aging gradient for layers other than the top layer is not significant. The top layer is more susceptible to aging since long-term aging is strongly affected by oxidation. Irrespective of the thickness of the top AC layer, it is always divided in two sublayers (12.7 mm and the remaining thickness). Unbound base layers thicker than 152 mm and unbound subbase layers thicker than 203 mm are sublayered for analysis purposes. For the base layer (first unbound layer), the first sublayer is always 51 mm. The remaining thickness of the base layer and any subbase layers that are sublayered are divided into sublayers with a minimum thickness of 102 mm. For compacted and natural subgrades, the minimum sublayer thickness is 305 mm. A pavement structure is sublayered only to a depth of 2.4 m. Any remaining subgrade is treated as an infinite layer. If bedrock is present, then the remaining subgrade is treated as one layer beyond 2.4 m; bedrock is not sublayered and is always treated as an infinite layer.

The material properties of each pavement layer are used to characterize material behavior within the specific response model. Bound materials generally display a linear, or nearly linear, stress-strain relationship. Unbound materials display stress-dependent properties. Granular materials are generally "stress hardening" and show an increase in modulus with an increase in stress. Fine-grained soils are generally "stress softening" and display a modulus decrease with increased stress. Material properties associated with pavement distress criteria are normally linked to some measure of material stiffness/strength (dynamic modulus, resilient modulus, and tensile strength).

Hierarchical Input Level

One unique feature of the MEPDG is that pavement designers have a great deal of flexibility in obtaining the design input for a design project based on the critical nature of the project and the available resources through the Hierarchical Input Level (HIL). The HIL can be applied to various aspects: traffic, materials, and environmental input. In general, there are three HILs.

Level 1 input results in the highest level of accuracy and, thus, would have the lowest level of uncertainty or error. Input at this level would typically be used for designing heavily trafficked pavement or wherever there are safety concerns or serious economic consequences of early failure. Level 1 material input requires laboratory or field testing, such as the DSR testing of asphalt binder, the complex modulus testing of AC, and site-specific axle load spectra. Consequently, obtaining Level 1 input requires more resources and time.

Level 2 input results in an intermediate level of accuracy. This level could be used when resources or testing equipment are not available for tests required for Level 1. Level 2 input typically would be user-selected, possibly from an agency database, could be derived from a limited testing program, or could be estimated through correlations. Examples would be estimating the dynamic modulus of AC mixtures from binder, aggregate, and mixture properties or using site-specific traffic volume and traffic classification data in conjunction with agency-specific axle load spectra.

Level 3 input results in the lowest level of accuracy. This level might be used for designs where there are minimal consequences of early failure (e.g., lower volume roads). Input typically would be user-selected values or typical averages for the region. Examples include default unbound materials resilient modulus values or default AC mixture properties estimated from aggregate gradation and binder grade.

For this study, all input still has to be obtained by using a mix of three HILs although comprehensive data have been collected for the SISSI project. Available HILs for the SISSI data are given in Table 1.

Table 1. Available hierarchical input levels of SISSI data

Category	Input	Availability	Hierarchical Input Level
Traffic	Initial AADTT	Y	1
	Monthly Adjustment Factor	Y	1
	Vehicle Class Distribution	Y	1
	Hourly Truck Distribution	Y	1
	Traffic Growth Factor	Y	1
	Axle Load Distribution Factor	Y	1
	Lateral Traffic Wander	N	3
	Number of Axles for Each Vehicle Class	Y	1
	Axle Configuration	N	3
	Axle Spacing	Y	1
	Wheelbase	N	3
Climate	Weather Data	Y	1
	Ground Water Table Depth	N	3
Structure	Layer Thickness	Y	1
Material	AC Mixture	Y	1
	Binder	Y	1
	AC General	Y	1*
	PCC	N	3
	Granular	N	3
Thermal Cracking	Creep Compliance	Y	1
	Tensile Strength	Y	1
	Coefficient of Thermal Contraction	N	3

* Except for Poisson's ratio, unit weight, and thermal properties

Performance Models

Fatigue Cracking

To characterize the fatigue mechanism in AC layers, numerous models can be found in the existing literature. The fatigue-cracking model, which calculates the number of cycles to failure, only expresses the stage of fatigue cracking described as the crack initiation stage. The second stage, or vertical crack propagation stage, is accounted for in these models by using the field adjustment factor. Other models in the literature use two different equations to express each stage of the fatigue cracking. For example, Lytton et al. (1993) used fracture mechanics based on the Paris law to model the crack propagation stage in the development of the theoretical Superpave Model. Finally, a third stage of fatigue fracture is associated with the growth in longitudinal area in which fatigue cracking occurs. In general, true field fatigue failure is associated with a percentage of fatigue cracking along the roadway.

The MEPDG approach first calculates the fatigue damage at critical locations that may be either at the surface and result in longitudinal (top-down) cracking or at the bottom of the AC layer and result in alligator (bottom-up) cracking. The fatigue damage is then correlated using a calibration factor to the fatigue cracking. Estimation of fatigue damage is based on Miner's Law, which states that damage is given by the following relationship:

$$D = \sum_{i=1}^{T} \frac{n_i}{N_i} \quad (1)$$

where D is damage, T is the total number of analysis periods, n_i is actual traffic for analysis period i, and N_i is traffic allowed under conditions prevailing in i. The relationship used for the prediction of the number of repetitions to fatigue cracking is expressed as:

$$N_f = 0.00432 * k'_1 * (10^{[V_b/(V_a+V_b)-0.69]}) * (\frac{1}{\varepsilon_t})^{3.9492} * (\frac{1}{E})^{1.281} \quad (2)$$

where V_b is the effective binder content, V_a is the air voids, and k_1 is introduced to provide a correction for different asphalt layer thickness (h_{AC}) effects. For alligator cracking:

$$k'_1 = \frac{1}{0.000398 + \frac{0.003602}{1+e^{(11.02-3.49*h_{AC})}}} \quad (3)$$

For longitudinal cracking:

$$k'_1 = \frac{1}{0.01 + \frac{12.00}{1+e^{(15.676-2.8186*h_{AC})}}} \quad (4)$$

In the MEPDG, the mathematical relationship used for fatigue characterization is of the following form. For alligator cracking (percent of total lane area):

$$FC_A = [\frac{6000}{1+e^{(C_1+C_2*\log10(D*100))}}] * (\frac{1}{60}) \quad (5)$$

where FC_A is alligator cracking, percent lane area, D is alligator damage, C_1 = -2* C_2, $C_2 = -2.40874 - 39.748 * (1 + h_{AC})^{-2.856}$, and h_{AC} is the total thickness of AC layers, in.

For longitudinal cracking (percent of total lane area):

$$FC_L = [\frac{1000}{1 + e^{(7.0 - 3.5*\log 10(D*100))}}] * 10.56 \quad (6)$$

where FC_L is longitudinal cracking, ft/mile, and D is longitudinal damage. The MEPDG considers that bottom-up fatigue cracking results in "alligator cracking" distress alone, and surface-down fatigue cracking is associated with "longitudinal cracking."

Rutting

Rutting, or permanent deformation, is a load-related distress caused by cumulative applications of loads at moderate to high temperatures, when the asphalt concrete mixture has the lowest stiffness. It can be divided into three stages. Primary rutting develops early in the service life and is caused predominantly by densification of the mixture (compaction effort by passing traffic) and with decreasing rate of plastic deformations. In the secondary stage, rutting increments are smaller at a constant rate, and the mixture is mostly undergoing plastic shear deformations. The tertiary stage is when shear failure occurs, and the mixture flows to rupture. In the MEPDG, only rutting in the primary and secondary stages is predicted. Total rutting is the summation of rut depths from all layers, AC, base/subbase, and subgrade.

$$RD_{total} = RD_{AC} + RD_{Base} + RD_{Subgrade} \quad (7)$$

The asphalt concrete layer is sub-divided into sublayers, and the total predicted rut depth for the AC layer is given by:

$$RD_{AC} = \sum_{i=1}^{n} [(\varepsilon_r * k_1 * 10^{-3.4488} T^{1.5606} N^{0.479244})_i * h_{ACi}] \quad (8)$$

where RD_{AC} is rut depth in the AC layer, n is number of sublayers, ε_r is vertical resilient strain at the middle of the sublayer i for a give load, k_1 is depth correction factor, T is temperature, N is number of repetitions for a given load, and h_{ACi} is the thickness of sublayer i.

$$k_1 = C * 0.328196^D \quad (9)$$

where D is depth to the point of strain calculation, and C is calculated as:

$$C = (-0.1039 * h^2{}_{AC} + 2.4868 * h_{AC} - 17.342) + (0.0172 * h^2{}_{AC} - 1.7331 * h_{AC} + 27.428) * D \quad (10)$$

The MEPDG also divides all unbound granular materials into sublayers, and the total rutting for each layer is the summation of the rut depth of all sublayers. The predicted rut depth for the unbound granular base/subbase is as follows:

$$RD_G = \sum_{i=1}^{n} \beta * a * [e^{-(\frac{b}{N})^c}] * \varepsilon_v * h_i \tag{11}$$

where RD_G is rut depth in the unbound granular layer, β is calibration factor, a, b, and c are material properties, N is number of traffic repetitions, and h_i is the thickness of sublayer i.

$$\log c = -0.61119 - 0.017638 * W_c \tag{12}$$

$$\log a = \frac{e^{b^c} * 0.15 + e^{(b/10^9)^c}}{2} \tag{13}$$

$$b = 10^9 * (\frac{-4.89285}{1-10^{9c}})^{1/c} \tag{14}$$

$$W_c = 51.712 * [(\frac{E_r}{2555})^{1/0.64}]^{-0.3586*GWT^{0.1192}} \tag{15}$$

where W_c is percent water content, E_r is resilient modulus of the unbound granular layer/sublayer, psi, and GWT is ground water table depth, ft. The calibration factors, β, for base/subbase and subgrade are 1.673 and 1.35, respectively.

Thermal Cracking

Thermal cracking is a consequence of heating/cooling cycles occurring in the asphalt concrete. The pavement surface cools down faster and with more intensity than the core of the pavement structure, which causes thermal cracking to occur at the surface of flexible pavements. Thermal cracks extend in the transverse direction across the width of the pavement. The thermal cracking model (TCMODEL) incorporated in the MEPDG converts data directly from the Superpave Indirect Tensile Test (IDT) into viscoelastic properties, specifically the creep compliance function that is further converted to the relaxation modulus through Laplace Transformation. The relaxation modulus is then coupled with the temperature data from the Enhanced Integrated Climatic Model (EICM) to predict thermal stresses through the convolution integral, assuming AC to be LVE and thermorheologically simple:

$$\sigma(\xi) = \int_0^{\xi} E(\xi - \xi') \frac{d\varepsilon}{d\xi'} d\xi' \tag{16}$$

where $\sigma(\xi)$ = stress at reduced time, ξ; ξ' = integration variable; $E(\xi - \xi')$ = relaxation modulus at reduced time, $\xi - \xi'$; ε = strain at reduced time; $\xi = \alpha(T(\xi') - T_0))$; α = linear coefficient of thermal contraction of AC mixtures; $T(\xi')$ = pavement temperature at reduced time, ξ'; and T_0 = initial pavement temperature.

The growth behavior of the thermal crack is computed using Paris's law:

$$\Delta C = 10^{k*(4.389-2.52*\log(10000*\sigma_m*n))}\Delta K^n \tag{17}$$

where ΔC = change in the crack depth due to a cooling cycle, ΔK = change in the stress intensity factor due to a cooling cycle, k = regression coefficient determined through field calibration, σ_m = undamaged strength of AC mixtures, and n = fracture parameter for the AC mixture. The indirect tensile strength, measured at -10ºC, is used as undamaged strength σ_m. The TCMODEL uses the m value from the creep compliance master curve to compute the fracture parameter, $n = 0.8*(1+1/m)$. Finally, the amount of thermal cracking can be predicted:

$$TC = 400 * N(\frac{\log C / h_{AC}}{\sigma}) \tag{18}$$

where TC = amount of thermal cracking, $N()$ is standard normal distribution evaluated at (), and σ is standard deviation of the log of the depth of cracks in the pavement.

Smoothness

The IRI over the pavement life depends on the initial as-constructed longitudinal profile of the pavement from which the initial IRI is computed and on the subsequent incremental development of distresses over time. These distresses include rutting, alligator cracking, longitudinal cracking, and thermal cracking for flexible pavements. In addition, smoothness loss due to soil movements and other climatic factors (depressions, frost heave, and settlement) are considered in the prediction of smoothness through the use of a "site factor" term (represented by a cluster based on foundation and climatic properties). The models for predicting IRI of flexible pavements with a granular base are a function of the base type as described below:

$$\begin{aligned} IRI = IRI_0 &+ 0.0463*[SF*(e^{\frac{age}{20}}-1)] + 0.00119*TC_{LT} \\ &+ 0.1834*COV_{RD} + 0.00384*FC_T \end{aligned} \tag{19}$$

where IRI is IRI at any given time, m/km, IRI_0 is initial IRI, m/km, SF is site factor, $e^{\frac{age}{20}}-1$ is age term (where age is expressed in years), COV_{RD} is coefficient of variation of the rut depths, percent, TC_{LT} is total length of transverse cracks at all severity levels, m, and FC_T is fatigue cracking (alligator plus longitudinal) in the wheel path, percent of total lane area.

CHAPTER 3: EVALUATING THE SENSITIVITY OF MEPDG TO SISSI DATA

Introduction

The objective of the sensitivity study was to evaluate the input parameters related to AC material properties, traffic, and climate that significantly or insignificantly influence the predicted performance for two specific SISSI flexible pavements: Warren and Blair. To achieve this objective, the sensitivity analysis of five MEPDG performance measures (longitudinal cracking, alligator cracking, AC rutting, subgrade rutting, and smoothness) was conducted by either varying the magnitudes or the distribution of a single input parameter. Although reflection cracking is arguably the most important distress in rehabilitated flexible and composite pavements, it is not included in the present study because the reflection cracking model in the current MEPDG is intended only as a very rough placeholder until a more accurate, reliable reflection cracking model can be developed; this work is currently under way in NCHRP Project 1-41.

Analysis Parameters

A thorough literature review suggests that over 50 MEPDG input parameters exhibit considerable sensitivity on various performance measures of flexible pavements, typically using Level 3 input with national calibrations. Noteworthy recent publications related to this topic include: Masad and Little 2004, Galal and Chehab 2005, Freeman et al. 2005, Kim et al. 2005, El-Basyouny and Witczak 2005, El-Basyouny et al. 2005a and 2005b, Yin et al. 2006, Sadasivam and Morian 2006, Carvalho and Schwartz 2006, Timm 2006, and Yin et al. 2006. With the research approach of this study, uncertainties associated with site-specific parameters will be only incorporated into the empirical part of performance predictions. In other words, only parameters required by transfer functions will be considered. Therefore, a total of 14 site-specific input parameters were selected as varied parameters for the sensitivity study. As shown in Tables 1 and 2, selected parameters can be categorized as follows:

- Climate: ground water table depth (*GWT*).
- Structure: layer thickness (h).
- Material: effective binder content (V_b) and air voids (V_a) of bound materials and resilient modulus (E_r) of unbound materials.

The correlations among input parameters were not within the scope of this analysis. To investigate the effect of a particular pavement input parameter, the other input parameters are held constant. While one design parameter was being examined at multiple variation levels (such as 10 percent, 20 percent, and 30 percent), an “as constructed” value was assigned for the other input parameters.

Analysis Results

For the purpose of having comparable results, the sensitivity degree of each varied parameter was computed in terms of a ratio between percent changes of the parameter itself and percent changes of performance predictions (e.g., rut depth) at the end of analysis time period. For example, a sensitivity ratio (*SR*) of 1.0 means that the amount of variation in the varied parameter will result in, at most, the same amount of variation in the performance measure. Sensitivity analysis results are summarized in Tables 1 and 2 for Warren and Blair, respectively.

Average *SRs* at all variation levels are also reported. Since SR values vary between two SISSI sites, selected analysis parameters were further classified for individual performance measures in accordance to their averaged *SRs* at all variation levels (Table 3) such that general conclusions can be made:

- Insensitive (*IS*): *SR* < 0.5
- Sensitive (*S*): 0.5 ≤ *SR* < 1.0
- Very Sensitive (*VS*): *SR* ≥ 1.0

The following sections provide discussions for each performance measure.

Longitudinal Cracking

As demonstrated in Figure 1, the MEPDG predictions for longitudinal cracking are very sensitive to the effective binder content of upper AC layers. This observation is reasonable because the effective binder content is an important source of variability in construction and among the most influential parameters determining the mixture stiffness and, hence, performance measures. Longitudinal cracks may be also caused by high tensile strains at the top of the surface AC layer due to load-related effects and the effects of age-hardening of AC materials. However, the binder layer thickness for both Warren and Blair exhibits some sensitivity on longitudinal cracking predictions. Part of this observation could be due to the immature nature of the MEPDG model; an enhanced top-down cracking model is the expected product from NCHRP Project 1-42A, which is currently under way.

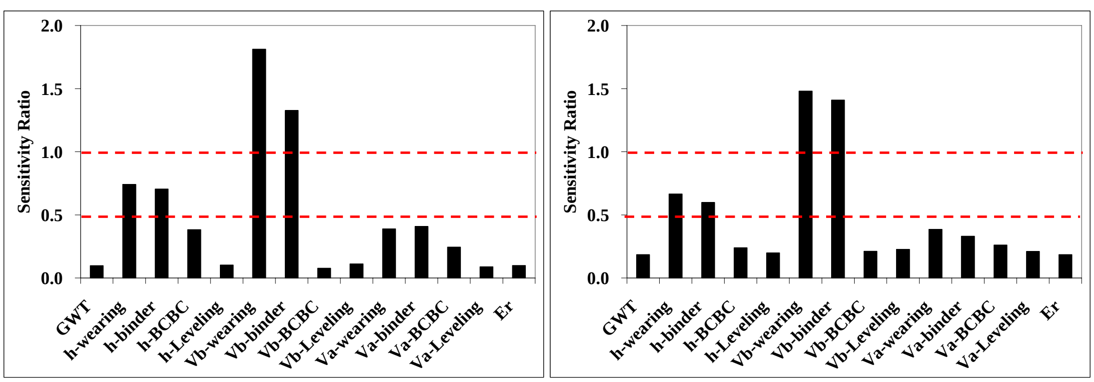

(a) Warren (b) Blair

Figure 1. Sensitivity of longitudinal cracking to analysis parameters

Table 2. Sensitivity ratios at different variation levels for Warren

Category	Analysis Parameter		Longitudinal Cracking				Alligator Cracking				AC Rutting				Subgrade Rutting				Smoothness			
			10%	20%	30%	Ave	10%	20%	30%	Ave	10%	20%	30%	Ave	10%	20%	30%	Ave	10%	20%	30%	Ave
Climate	GWT	Subgrade	0.09	0.11	0.10	0.10	0.33	0.27	0.41	0.30	0.00	0.00	0.00	0.00	1.05	1.43	1.58	1.35	0.20	0.35	0.43	0.33
Structure	*h*	Wearing	0.62	0.75	0.85	0.74	0.69	0.77	0.79	0.75	1.07	1.31	1.36	1.24	0.00	0.00	0.00	0.00	0.61	0.64	0.69	0.64
		Binder	0.61	0.62	0.89	0.70	0.77	0.95	0.96	0.89	1.08	1.26	1.36	1.23	0.00	0.00	0.00	0.00	0.73	0.84	0.85	0.80
		BCBC	0.21	0.45	0.49	0.38	0.55	0.87	0.92	0.78	1.00	1.15	1.42	1.19	0.00	0.00	0.00	0.00	0.58	0.65	0.77	0.66
		Leveling	0.06	0.11	0.13	0.10	0.53	0.57	0.94	0.68	1.22	1.39	1.43	1.34	0.00	0.00	0.00	0.00	0.69	0.82	0.84	0.78
Material	*Vb*	Wearing	1.76	1.79	1.89	1.81	0.66	0.74	0.77	0.72	1.47	1.58	1.59	1.54	0.00	0.00	0.00	0.00	0.80	0.84	0.96	0.87
		Binder	1.15	1.18	1.65	1.33	0.61	0.61	0.73	0.65	1.09	1.78	1.81	1.56	0.00	0.00	0.00	0.00	0.51	0.60	0.74	0.62
		BCBC	0.06	0.08	0.10	0.08	0.22	0.36	0.43	0.34	0.52	0.58	0.81	0.64	0.00	0.00	0.00	0.00	0.80	0.92	0.93	0.89
		Leveling	0.07	0.13	0.14	0.11	0.08	0.13	0.14	0.12	0.23	0.27	0.34	0.28	0.00	0.00	0.00	0.00	0.55	0.88	0.95	0.79
	Va	Wearing	0.30	0.41	0.46	0.39	0.07	0.08	0.13	0.09	2.15	2.19	2.95	2.43	0.00	0.00	0.00	0.00	0.58	0.61	0.90	0.70
		Binder	0.40	0.41	0.42	0.41	0.10	0.11	0.15	0.12	2.66	2.73	2.78	2.72	0.00	0.00	0.00	0.00	0.84	0.92	0.98	0.91
		BCBC	0.22	0.26	0.26	0.25	0.02	0.06	0.08	0.05	1.27	1.30	1.37	1.31	0.00	0.00	0.00	0.00	0.62	0.65	0.94	0.74
		Leveling	0.06	0.07	0.14	0.09	0.12	0.13	0.15	0.13	1.10	1.12	1.23	1.15	0.00	0.00	0.00	0.00	0.84	0.90	0.97	0.90
	Er	Granular	0.08	0.10	0.12	0.10	0.07	0.08	0.14	0.10	0.00	0.00	0.00	0.00	1.08	1.26	1.41	1.25	0.40	0.43	0.44	0.42

Table 3. Sensitivity ratios at different variation levels for Blair

Category	Analysis Parameter		Longitudinal Cracking				Alligator Cracking				AC Rutting				Subgrade Rutting				Smoothness			
			10%	20%	30%	Ave	10%	20%	30%	Ave	10%	20%	30%	Ave	10%	20%	30%	Ave	10%	20%	30%	Ave
Climate	*GWT*	Subgrade	0.12	0.22	0.22	0.19	0.14	0.38	0.47	0.26	0.00	0.00	0.00	0.00	1.47	1.63	1.80	1.64	0.14	0.25	0.27	0.22
Structure	*h*	Wearing	0.53	0.70	0.76	0.67	0.56	0.95	0.96	0.83	1.17	1.27	1.28	1.24	0.00	0.00	0.00	0.00	0.62	0.65	0.78	0.68
		Binder	0.51	0.55	0.74	0.60	0.77	0.79	0.93	0.83	1.38	1.44	1.45	1.42	0.00	0.00	0.00	0.00	0.78	0.81	0.95	0.85
		BCBC	0.16	0.21	0.34	0.24	0.79	0.96	0.97	0.91	1.08	1.20	1.47	1.25	0.00	0.00	0.00	0.00	0.67	0.70	0.97	0.78
Material	*Vb*	Wearing	1.06	1.56	1.83	1.48	0.74	0.98	0.99	0.90	1.51	1.71	1.78	1.67	0.00	0.00	0.00	0.00	0.75	0.76	0.82	0.78
		Binder	1.14	1.34	1.74	1.41	0.75	0.89	0.96	0.87	1.06	1.49	1.79	1.45	0.00	0.00	0.00	0.00	0.65	0.66	0.84	0.72
		BCBC	0.17	0.19	0.28	0.21	0.14	0.29	0.37	0.27	0.53	0.69	0.74	0.65	0.00	0.00	0.00	0.00	0.58	0.71	0.82	0.71
	Va	Wearing	0.34	0.34	0.47	0.38	0.13	0.19	0.22	0.18	2.04	2.26	2.35	2.22	0.00	0.00	0.00	0.00	0.51	0.53	0.74	0.59
		Binder	0.27	0.32	0.40	0.33	0.16	0.17	0.25	0.19	2.45	2.91	2.98	2.78	0.00	0.00	0.00	0.00	0.58	0.72	0.90	0.73
		BCBC	0.16	0.17	0.46	0.26	0.17	0.18	0.20	0.18	1.32	1.37	1.42	1.37	0.00	0.00	0.00	0.00	0.56	0.70	0.76	0.68
	Er	Granular	0.11	0.18	0.27	0.19	0.14	0.17	0.18	0.16	0.00	0.00	0.00	0.00	1.05	1.07	1.19	1.10	0.59	0.61	0.80	0.67

Table 4. Sensitivity classification of analysis parameters

Category	Analysis Parameter		Sensitivity Classification				
			Longitudinal Cracking	Alligator Cracking	AC Rutting	Subgrade Rutting	Smoothness
Climate	*GWT*	Subgrade	*IS/IS*[a]	*IS/IS*	*IS/IS*	*VS/VS*	*IS/IS*
Structure	*h*	Wearing	*S/S*	*S/S*	*VS/VS*	*IS/IS*	*S/S*
		Binder	*S/S*	*S/S*	*VS/VS*	*IS/IS*	*S/S*
		BCBC	*IS/IS*	*S/S*	*VS/VS*	*IS/IS*	*S/S*
		Leveling[b]	*IS*	*S*	*VS*	*IS*	*S*
Material	*Vb*	Wearing	*VS/VS*	*S/S*	*VS/VS*	*IS/IS*	*S/S*
		Binder	*VS/VS*	*S/S*	*VS/VS*	*IS/IS*	*S/S*
		BCBC	*IS/IS*	*IS/IS*	*S/S*	*IS/IS*	*S/S*
		Leveling[b]	*IS*	*IS*	*IS*	*IS*	*S*
	Va	Wearing	*IS/IS*	*IS/IS*	*VS/VS*	*IS/IS*	*S/S*
		Binder	*IS/IS*	*IS/IS*	*VS/VS*	*IS/IS*	*S/S*
		BCBC	*IS/IS*	*IS/IS*	*VS/VS*	*IS/IS*	*S/S*
		Leveling[b]	*IS*	*IS*	*VS*	*IS*	*S*
	Er	Granular	*IS/IS*	*IS/IS*	*IS/IS*	*VS/VS*	*IS/S*

[a] Warren/Blair, [b] Warren

Alligator Cracking

It can be concluded from Figure 2 that the MEPDG predictions for alligator cracking are very sensitive to the layer thickness and effective binder content, particularly for upper AC layers. The total AC layer thickness not only influences strain and stress magnitude but is directly linked to the location where fatigue cracks initiate as well as under the specific mode of loading (constant stress or strain) under which fracture occurs. Increasing the AC thickness reduces the tensile strains at the bottom of the AC layer and consequently mitigates alligator (bottom-up) cracking. This feature is evident for both the Warren and Blair sites. Effective binder content also has a pronounced impact on top-down cracking. Mixtures rich in binder generally have better tensile strength and better cracking resistance.

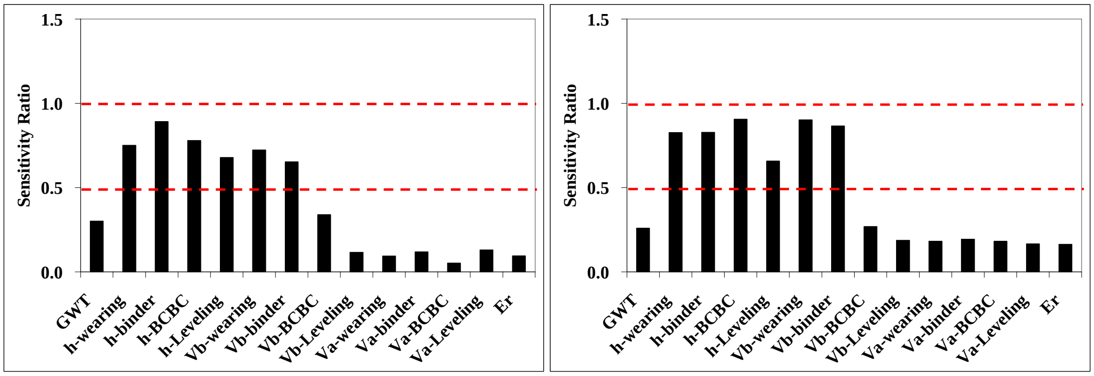

(a) Warren (b) Blair

Figure 2. Sensitivity of alligator cracking to analysis parameters

AC Rutting

Rutting was found to be sensitive or very sensitive to most of the analysis parameters. Figure 3 suggests that air voids have a more significant impact on rut depth than other parameters. Lack of adequate field compaction results in high air voids, which generates premature permanent deformations as the mixture becomes more dense under traffic. The MEPDG computes the total AC rutting depth from the permanent deformation of individual AC layers; therefore, it is expected that the layer thickness would play an important role in rutting predictions. Nevertheless, this feature is not very clear in the two pavement structures considered in this study.

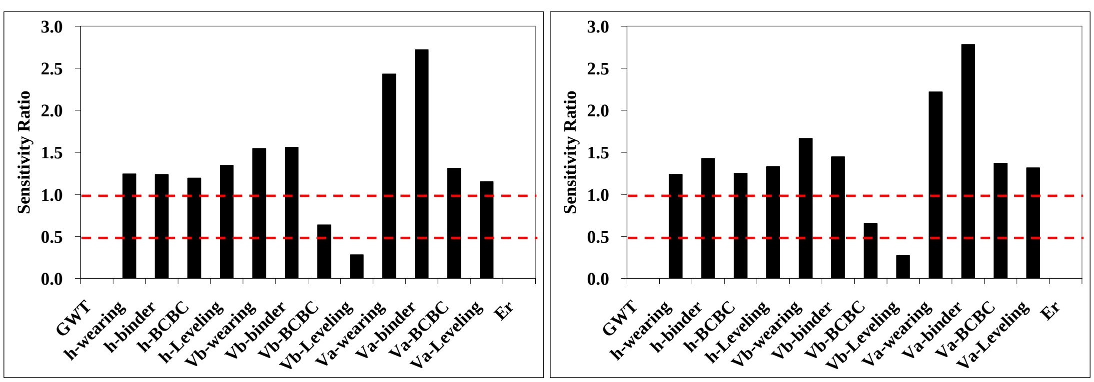

(a) Warren (b) Blair

Figure 3. Sensitivity of AC rutting to analysis parameters

Subgrade Rutting

Figure 4 reveals the sensitivity of subgrade rutting to unbound material-related analysis parameters, ground water table depth, and resilient modulus, which is what was expected. Compared to low resilient modulus, ground water table depth seems to weaken the subgrade more and, accordingly, causes a poorer subgrade rutting performance.

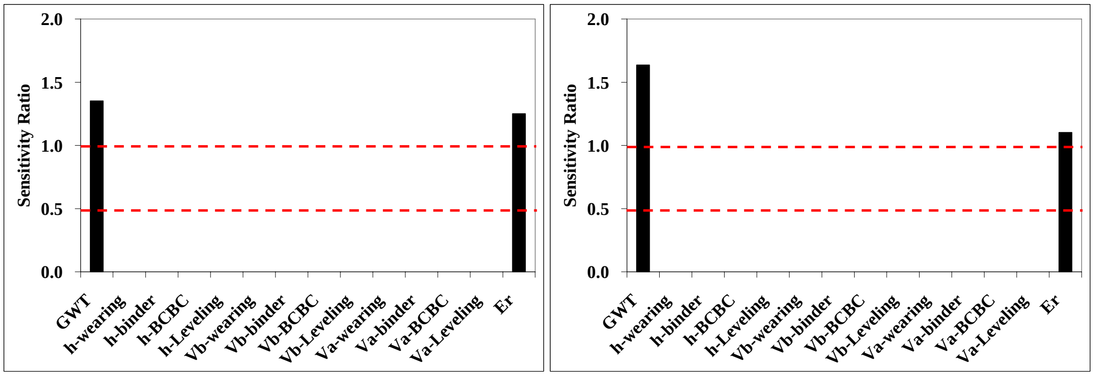

(a) Warren (b) Blair

Figure 4. Sensitivity of subgrade rutting to analysis parameters

Smoothness

Interestingly, there is no input parameter that has an *SR* above 1.0 for either Warren or Blair. This examination indicates that a pavement designer using the MEPDG for flexible pavement design should recognize the interactive effects among input parameters to obtain the predicted functional performance for satisfying the design criteria. Among all analysis parameters selected for the sensitivity study, only resilient modulus of unbound materials shows a discrepancy in terms of sensitivity classifications in the projected smoothness (Figure 5) for Warren and Blair. This discrepancy might be attributed to the variations in traffic, climate, and the material components in the structures of the two investigated flexible pavements.

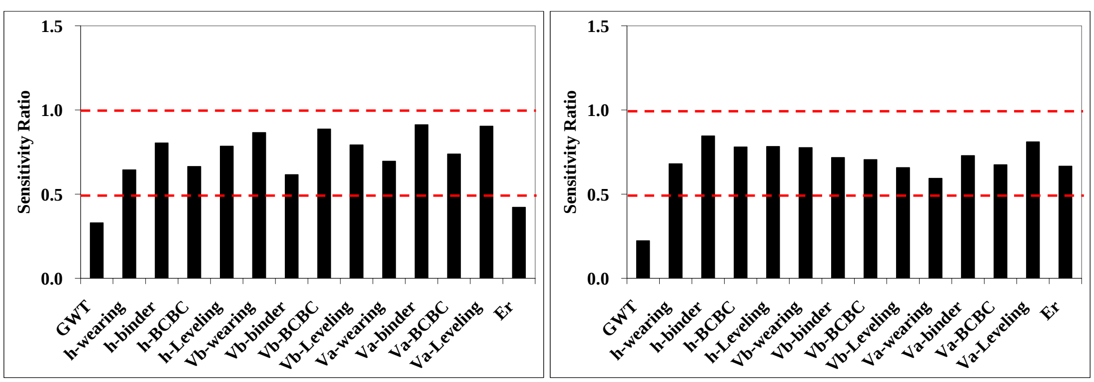

(a) Warren (b) Blair

Figure 5. Sensitivity of smoothness to analysis parameters

Summary

The sensitivity study detailed in this report provides a better understanding of how the design parameters affect flexible pavement performance. Similar conclusions can be drawn for both Warren and Blair:

- Longitudinal cracking predictions are sensitive to the layer thickness and effective binder content of AC layers.
- Alligator cracking predictions are sensitive to the layer thickness and effective binder content of AC layers.
- AC rutting predictions are sensitive to most of the analysis parameters, especially air voids.
- Subgrade rutting predictions are sensitive to ground water table depth and resilient modulus of unbound materials.
- No parameter has a significant impact on smoothness.

From the sensitivity study, it may be concluded that a small amount of change in some design parameters will result in a large difference in the predicted pavement performance. Consequently, if the predicted performance results are used in a design procedure, some quite different budget planning and rehabilitation activities would be needed. This means that uncertainties in estimating these parameters as design input variables introduce a dilemma for a pavement designer in deciding which prediction is accurate and which preservation actions should be taken in a given year. Therefore, accurate prediction of pavement performance is one of the most important tasks in having a reasonable road network system for pavement maintenance/rehabilitation alternative strategies. In other words, the efficiency of the budget plan and the expected pavement service life depend mainly on the accuracy of the pavement performance prediction. Therefore, each of the sensitive and very sensitive parameters, such as AC layer thickness, should be considered as a random variable following a certain probability distribution. In turn, it is appropriate to develop a probabilistic-based approach for pavement performance predictions.

CHAPTER 4: MEPDG APPLICATION TO THE SISSI SITES

Since the MEPDG software was used as a tool to predict pavement performance, this section presents the relevant details of running the MEPDG software. The sensitivity analysis in the previous section was conducted using version 0.9; however, the applications in the section were performed using version 1.0, which had by then become available. It is not anticipated that significant differences in the key sensitive parameters occurred between the two versions.

Description of MEPDG Input

A 20-year design life was assumed for all SISSI sites. Dates of pavement construction and traffic opening were obtained from previous SISSI reports. Initial IRI values were input as measured during the first profiling activity. A default reliability level of 90 percent was assumed for all performance criteria. The pavement will have no more than:

- an IRI of 2.7 m/km,
- longitudinal cracking of 190 m/km,
- alligator cracking of 25 percent,
- AC thermal fracture (transverse cracking) of 190 m/km, and
- 19-mm rut depth in the total pavement.

These criteria were kept the same for all SISSI sites. The MEPDG input is grouped under separate modules: traffic, climate, and structure. Some different kinds of input are highlighted in the following sections.

Traffic Module

MEPDG-required traffic inputs were determined from SISSI WIM data. These inputs include general traffic information (initial two-way annual average daily truck traffic (AADTT), percent of trucks in design direction, percent of trucks in design lane, and operational speed), traffic volume adjustment (monthly adjustment factors, AADTT distribution by vehicle class, hourly AADTT distribution), axle load distribution factors, number of axles per truck, lateral traffic wander, axle spacing, and wheelbase. Table 5 summarizes general traffic information for all SISSI sites. No traffic growth was observed for the SISSI sites based on the historical traffic data after the base year. Figure 6 shows the operational speed variation at the Tioga site as an example.

Table 5. Summary of general traffic information

SISSI Site	Initial AADTT	Trucks in design direction, %	Trucks in design lane, %	Operational speed, kph
Tioga	866	53	89	106
Mercer*	4724	48	81	108
Warren	400	50	89	93
Perry	1281	44	84	107
Delaware	905	41	79	77
Somerset	1994	40	98	100
Blair	175	48	81	68

*Mercer East and Mercer West share the same traffic condition

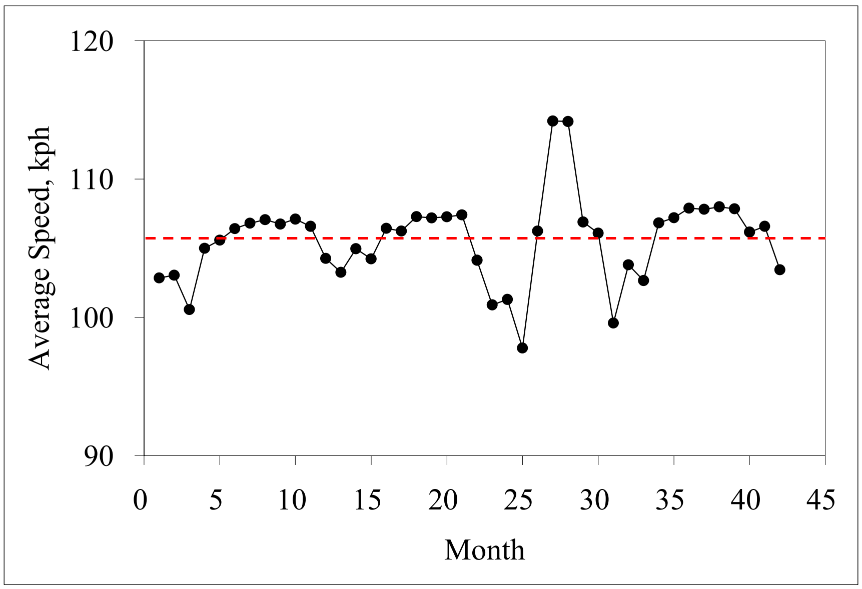

Figure 6. Operational speed at Tioga site

Climate Module

Depending upon the extent of information available, regardless of the pavement type, there are several methods of inputting climate data into the MEPDG software. For the SISSI project, a new climate data file was generated for each SISSI site. By specifying latitude and longitude (as shown in Table 6), the software lists the six closest weather stations in the climate database that are within a radius of 160 km to the site. It also shows the amount of climate data (i.e., 60 months) stored at each weather station. A ground water table depth (*GWT*) of 3 m was assumed, and all six weather stations were selected to interpolate climate data. The software automatically creates a climate data file that contains the sunrise time, sunset time, and radiation for each day of the design life period. In addition, for each 24-hour period in each day of the design life, the temperature, rainfall, air speed, sunshine, and *GWT* are also listed in the climate file. EICM was integrated in the MEPDG software to calculate the pavement temperature for AC materials and moisture content for granular materials. Researchers (Ongel and Harvey 2004, Yin et al. 2006) reported that the MEPDG software repeats climatic data to fill out the design period. For instance, if the design period is 20 years, but only 5 years of climatic data are available, the MEPDG software determines the temperature profiles for the available 5 years and then reuses the results four times to fill out the design period.

Table 6. Latitude and longitude for each SISSI site

SISSI Site	Latitude	Longitude
Tioga	N 41°40'	W 77°10'
Mercer*	N 41°12'	W 80°04'
Warren	N 40°51'	W 79°18'
Perry	N 40°30'	W 77°06'
Delaware	N 39°54'	W 75°33'
Somerset	N 39°60'	W 79°01'
Blair	N 40°26'	W 78°25'

*NOTE: Mercer East and Mercer West share the same climate condition

Structure Module

The structure module includes structural and material input. The subgrade layer was automatically divided into two sublayers by the software, as required by EICM. The MEPDG software calls for different input for different HILs, as shown in Table 1. For this study, all material properties of AC layers were input as Level 1, while fractured JPCP and granular materials were input as Level 3. For Level 1 AC material properties, the software requires the test temperatures in the range of -10^{o}C and 52^{o}C and the value of dynamic modulus ($|E^*|$) between 69 and 34474MPa regardless of frequency. Since the minimum and maximum temperatures selected in the complex modulus tests are 4 and 40^{o}C, $|E^*|$ values were extrapolated from sigmoidal-fitted dynamic modulus master curves. For test temperatures and frequencies resulting in extreme low and high values of dynamic modulus, $|E^*|$ values were adjusted by dropping or increasing 5% to 20%. Final $|E^*|$ values input in the MEPDG software are summarized in Appendix A.

The structure module also asks the user to provide all input required to predict thermal cracking. The software uses the tensile strength, creep compliance, and coefficient of thermal contraction of AC mixtures to predict thermal cracking. These kinds of input can all be either user input, or the software uses default values that are calculated from the AC material properties entered for the surface layer in the pavement structure. For the SISSI project, all material properties for thermal cracking prediction were input as Level 1 except for the coefficient of thermal contraction. Final creep compliance and tensile strength values are given in Appendix B.

Evaluation of MEPDG Predictions

After all input is provided, the MEPDG software begins the analysis process to predict the performance over the design life of the pavement. At the end of the analysis, the software creates a summary file and other output files. The summary file contains an input summary sheet, computed material modulus values, and distress summaries for all predicted distresses in a tabular format. Further, the predicted distresses and IRI over time are reported. During Phase II of the SISSI project, multiple distress surveys were scheduled for all sites except for Somerset. The condition data collected from the most recent distress surveys were considered in this study.

As shown in Table 7, the MEPDG software only predicts comparable rut depth among all distresses; therefore, the evaluation of MEPDG predictions is limited to rutting in this study. Graphic representations are provided in Figures **7** through 13. Two observations can be made through careful inspection of these figures:

- The MEPDG software predicts more reasonable rut depth for full-depth pavements than that for overlay ones.
- Excessive rutting occurred at full-depth pavements during the first few months after the section was opened to traffic. This phenomenon may have resulted from a combined effect of the initial traffic compaction and the low values of resilient moduli of granular layers in the summer.

Summary

This section presents performance predictions for all SISSI sites using the MEPDG software. Details on running the MEPDG software are also provided. Predicted pavement performance was evaluated using available field condition data. Overall, the MEPDG software provides reasonable performance predictions only for rutting. The discrepancy observed between the predictions and field conditions is perhaps due to the national calibration coefficients in the empirical performance models. It is believed that with the availability of large amounts of field condition data, the MEPDG models could be more accurately calibrated locally.

Table 7. Summary of performance predictions and field conditions

SISSI site	Distress	MEPDG Prediction	Field Condition	
Tioga (Nov 2007)	Longitudinal Cracking (m/km)	0	0	
	Alligator Cracking (%)	0	0	
	Transverse Cracking (m/km)	0.2	0	
	Rutting (mm)	2.9	Left Wheelpath	Right Wheelpath
			4.7	6.5
	Terminal IRI (mm/km)	1.967	N/A	
Mercer East (Oct 2007)	Longitudinal Cracking (m/km)	0	0	
	Alligator Cracking (%)	0	0	
	Transverse Cracking (m/km)	0.2	0	
	Rutting (mm)	3.0	Left Wheelpath	Right Wheelpath
			4.2	3.7
	Terminal IRI (mm/km)	0.982	N/A	
Mercer West (Oct 2007)	Longitudinal Cracking (m/km)	0	0	
	Alligator Cracking (%)	0	0	
	Transverse Cracking (m/km)	0.2	0	
	Rutting (mm)	2.8	Left Wheelpath	Right Wheelpath
			4.2	3.2
	Terminal IRI (mm/km)	1.184	N/A	
Warren (Mar 2007)	Longitudinal Cracking (m/km)	0	2340	
	Alligator Cracking (%)	0	0.2	
	Transverse Cracking (m/km)	0.2	103.3	
	Rutting (mm)	2.8	Left Wheelpath	Right Wheelpath
			5.2	3.5
	Terminal IRI (mm/km)	1.304	N/A	
Perry (Jul 2008)	Longitudinal Cracking (m/km)	0	0	
	Alligator Cracking (%)	0	0	
	Transverse Cracking (m/km)	0.2	0	
	Rutting (mm)	1.0	Left Wheelpath	Right Wheelpath
			5.5	2.9
	Terminal IRI (mm/km)	1.551	N/A	
Delaware (Oct 2008)	Longitudinal Cracking (m/km)	0	213	
	Alligator Cracking (%)	0	10	
	Transverse Cracking (m/km)	0.2	240.4	
	Rutting (mm)	0.8	Left Wheelpath	Right Wheelpath
			2.4	8.6
	Terminal IRI (mm/km)	1.671	N/A	
Somerset	Longitudinal Cracking (m/km)	0	N/A	
	Alligator Cracking (%)	0	N/A	
	Transverse Cracking (m/km)	185	N/A	
	Rutting (mm)	5.3	Left Wheelpath	Right Wheelpath
			N/A	N/A
	Terminal IRI (mm/km)	1.766	N/A	
Blair (Apr 2008)	Longitudinal Cracking (m/km)	0	0	
	Alligator Cracking (%)	0	0	
	Transverse Cracking (m/km)	0	0	
	Rutting (mm)	3.6	Left Wheelpath	Right Wheelpath
			3.8	5.6
	Terminal IRI (mm/km)	1.853	N/A	

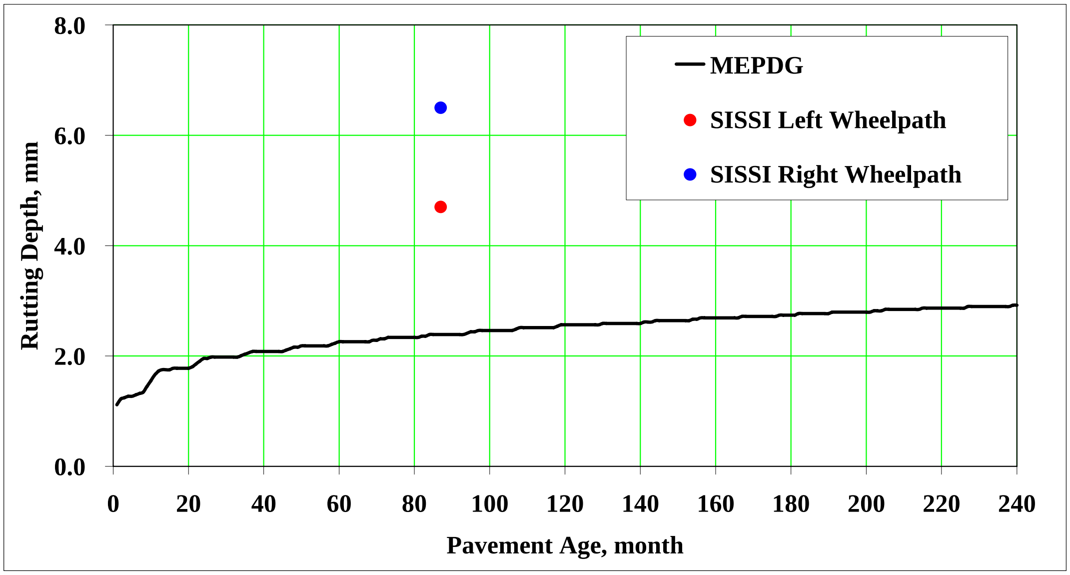

Figure 7. Comparison between predicted and observed rut depth at Tioga site

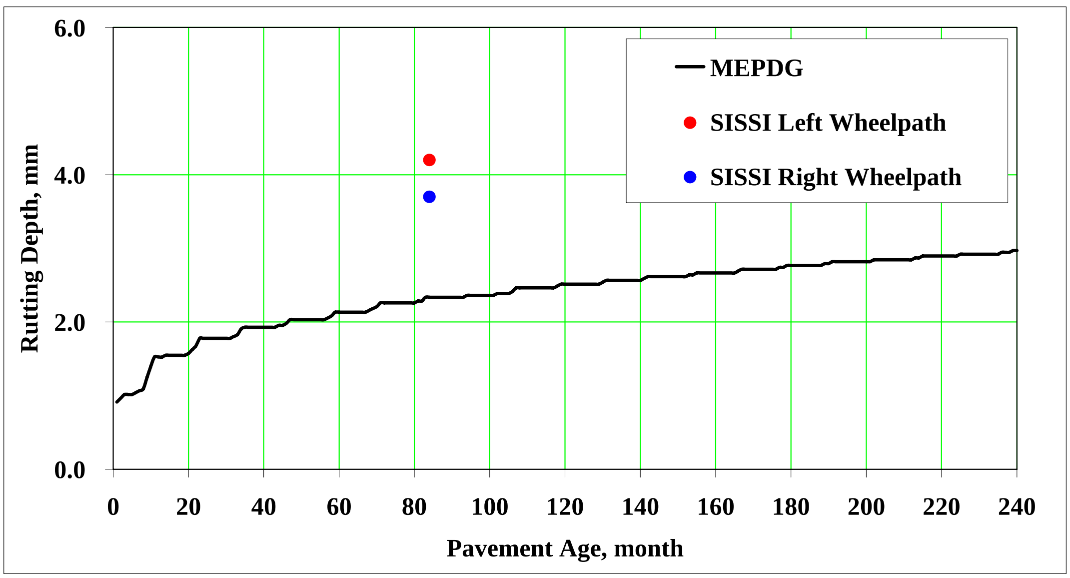

Figure 8. Comparison between predicted and observed rut depth at Mercer East site

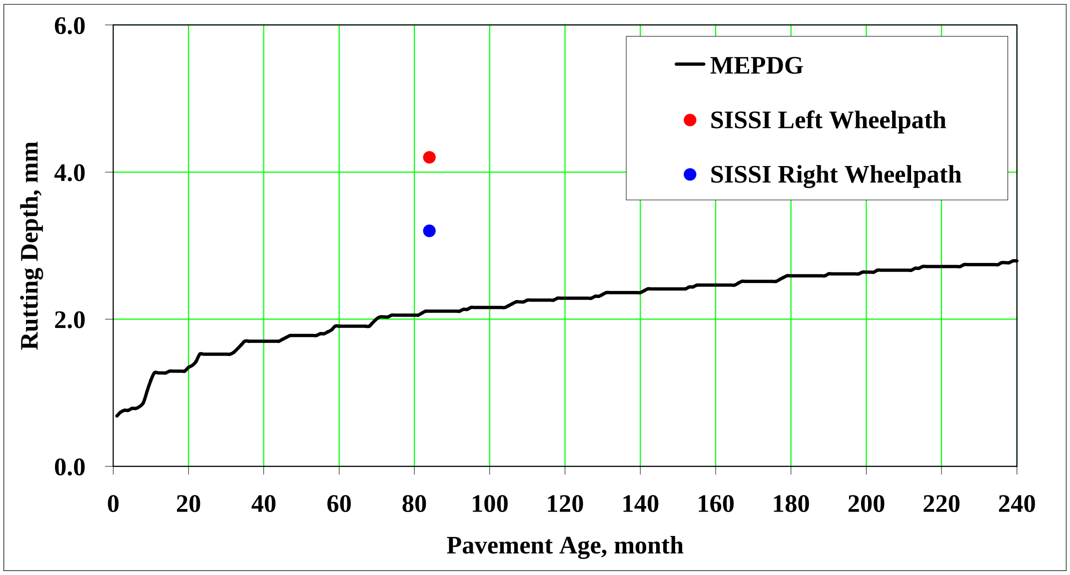

Figure 9. Comparison between predicted and observed rut depth at Mercer West site

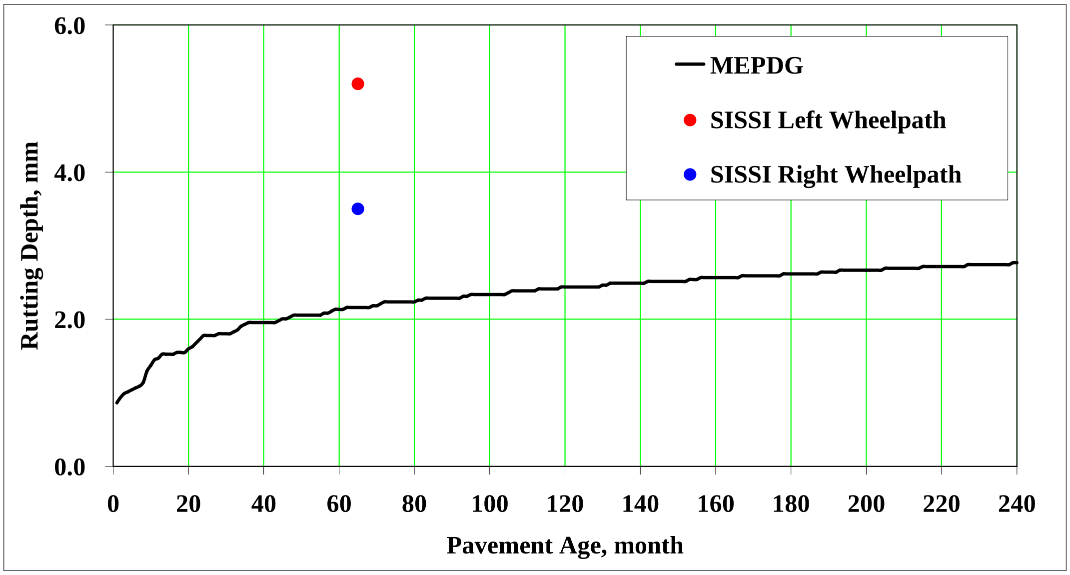

Figure 10. Comparison between predicted and observed rut depth at Warren site

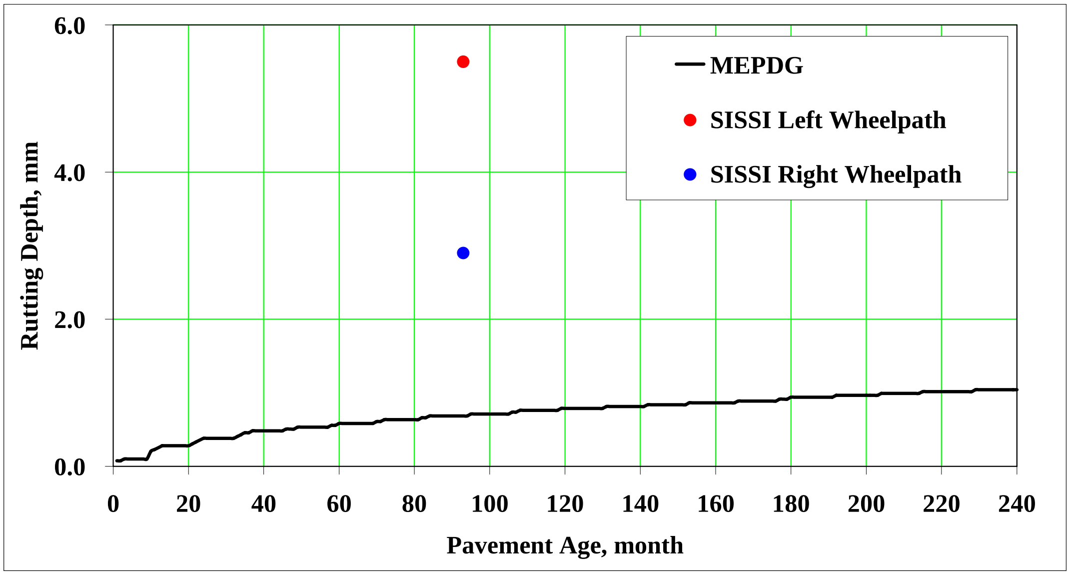

Figure 11. Comparison between predicted and observed rut depth at Perry site

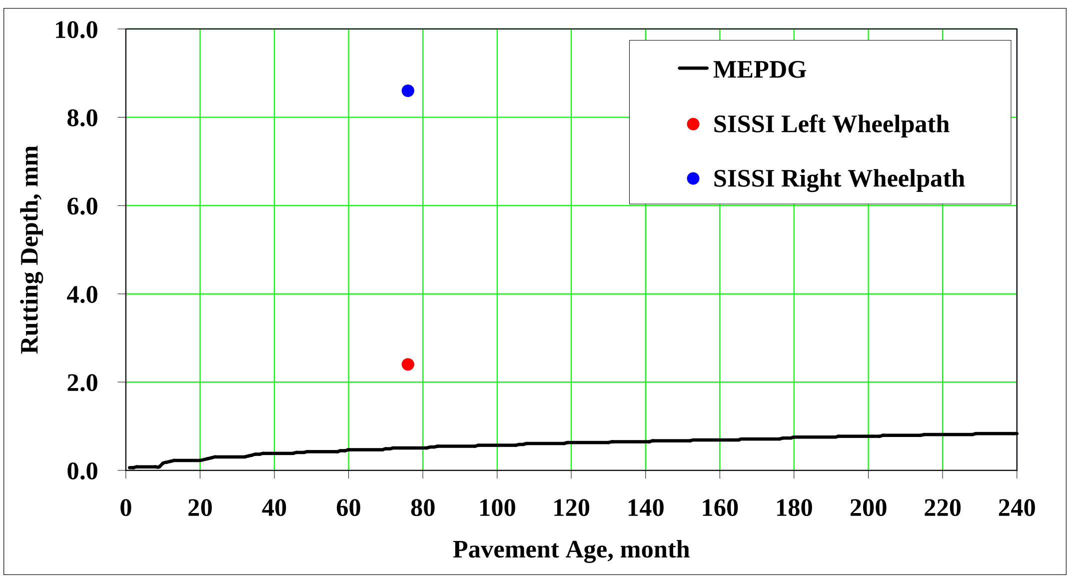

Figure 12. Comparison between predicted and observed rut depth at Delaware site

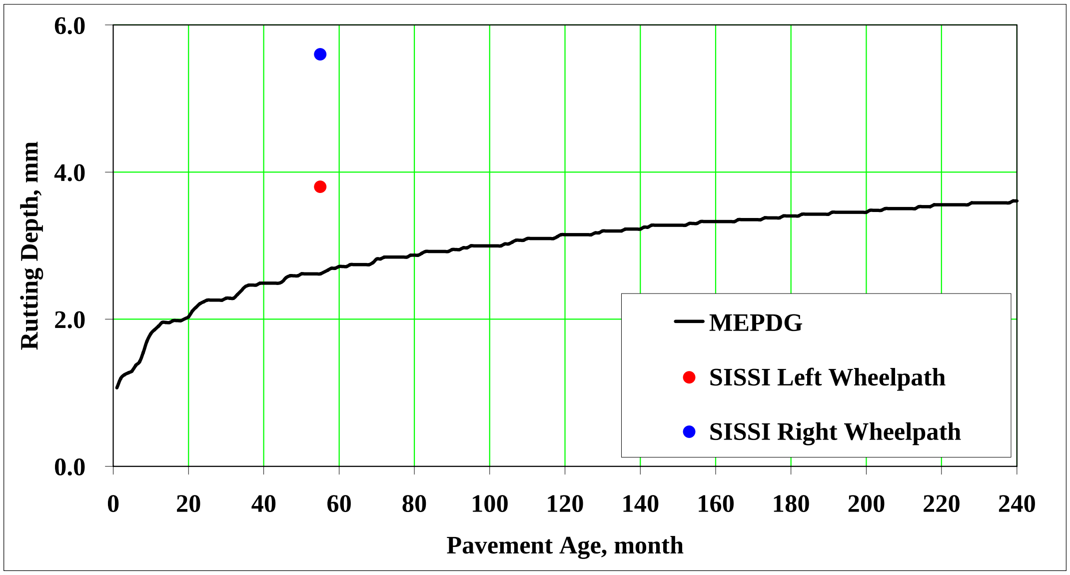

Figure 13. Comparison between predicted and observed rut depth at Blair site

CHAPTER 5: SIMULATION OF PAVEMENT RESPONSE USING 3-D FINITE ELEMENT MODELING

The effectiveness of any mechanistic-based pavement design depends on the accuracy of employed mechanistic parameters, such as stress and strain. There are three common approaches that can be used to compute the stresses and strains in pavement structures: layered elastic analysis, two-dimensional (2-D) finite element (FE) modeling, and three-dimensional (3-D) finite element modeling.

Layered elastic analysis (LEA) has been widely used to solve pavement engineering problems, in which each layer is treated as a horizontally continuous, isotropic, homogenous, and elastic medium. Elastic modulus and Poisson's ratio are important in controlling material behavior. A uniformly distributed vertical tire pressure around a circular or rectangular area is assumed. The thickness of each individual layer and material properties may vary from one layer to the next; however, continuity conditions at the interface are satisfied. In other words, the two adjacent layers have the same level of vertical stress, deflection, shear stress, and radial displacement. Several programs such as KENLAYER (Huang 1993) and BISAR (De Jong et al. 1973) calculate stresses and strains in pavement structures using this type of analysis. Although theoretical calculations using the layered theory are relatively inexpensive and easy, typical assumptions, such as that materials must be homogenous and linearly elastic within each layer and that the wheel loads applied on the surface must be axis-symmetric, significantly affect the reliability of analysis results. This effect becomes more pronounced when predicting pavement response under complex loading and environmental conditions; hence, a more advanced theoretical analysis tool, such as the FE method, would be needed.

The limitations of layered elastic analysis are the strengths of finite element analysis. In theory, the FE method allows a system to be analyzed as an assemblage of discrete bodies referred to as finite elements, and approximate solutions of governing partial differential equations are developed to describe the response at specific locations on each body, called nodes or nodal points. Complete system responses are computed by assembling individual element responses while satisfying continuity at the interconnected boundaries of each element. The FE method is by far the most universally applied numerical technique for flexible pavements (MEPDG 2004). It provides a modeling alternative that is well suited for applications involving pavement systems with inelastic materials, unusual boundary constraints, or complex loading conditions. Generally, the computational time for LEA increases with number of layers and with number of required stress computation points (e.g., to determine the critical locations for the critical response parameters and for superposition of multi-wheel loading cases). In contrast, an FE solution (assuming a sufficiently fine mesh) will not require significant additional computation time as the number of layers and/or stress computation points increases. The FE meshing already divides the pavement structure into many thin layers (theoretically, each layer of elements in the mesh could be assigned properties corresponding to different pavement layers), and the FE algorithms automatically determine the stresses and strains at all element integration points.

In 2-D FE modeling, plane strain or axis-symmetric conditions are generally assumed. Compared to the layered elastic analysis, the practical applications of 2-D FE modeling are greater because they can rigorously handle material anisotropy, material nonlinearity, and a variety of boundary conditions. Unfortunately, 2-D FE models cannot accurately capture spatial response under multiple wheel loads. Discrete vertical discontinuities are important three-dimensional geometric features in some flexible and composite pavement rehabilitation scenarios, in particular with regard to reflection cracking, which was not considered in this study. To overcome the limitations inherent in 2-D FE modeling approaches, 3-D FE models have gained increasing attention; however, computational cost and time increase with 3-D models as model dimensions, material properties, and mesh generation become more complicated.

Finite Element Modeling

Finite element analysis is a general tool for solving structural mechanics problems, with its earliest application to civil engineering problems dating back to the 1960s. The basic concept of FEA is the subdivision of a problem into a set of discrete or finite elements. The geometry of each finite element is defined in the simplest case by the coordinates of the corners; these points are called nodes. The variation of displacements within an element is then approximated in terms of the displacements of the nodes and a set of interpolation functions. Bilinear interpolation functions are the simplest for rectangular elements. Equation 20 gives the relationship between element nodal displacements and strains:

$$E = SU \tag{20}$$

where E is the strain vector, S is a suitable linear operator, and U is the nodal displacement vector. The element stiffness matrices are computed using:

$$K^e = \int B^T DBdv \tag{21}$$

where B is a matrix of linear operators (derivatives of shape functions), and D is the constitutive matrix. The element stiffness matrices are assembled for all elements, the boundary conditions are introduced, and the resulting equations are solved for incremental displacements, strains, and stresses. These are accumulated over the load increments to give the total displacements, strains, and stresses as functions of load level. An implicit FE formulation was used in this study, which means the loading is divided into relatively coarse increments, and an iterative technique is employed at the end of each increment to bring the internal stresses into equilibrium with the external applied loads.

The FE method is well suited for analyzing pavement engineering problems involving material nonlinearities and complex loading conditions. Such analysis proceeds by defining the characteristics of each pavement layer. The capabilities of the 3-D FE method for flexible pavement structural analysis are already well established in the literature (Zaghoul and White 1993, Chen et al. 1995, Cho et al. 1996, Hjelmstad et al. 1997, Shoukry 1998a, Uddin 1998, and White 1998).

The general purpose finite element software ABAQUS (version 6.6) was used in this study because of its capability in reducing the computation time through the use of 3-D reduced integration elements. ABAQUS also includes various material models, such as linear elastic, viscoelastic, and elastoplastic models. The following sections highlight some features of the developed FE model. A detailed validation study using field measurements and LVE solutions is also presented.

Modeling Strategy

Critical stresses and strains (peak values) typically tend to occur around the loads, and those should decrease in the far field. In FE modeling, there are two options for increasing the accuracy of results in the region of interest: 1) re-analyze the region of interest with greater mesh refinement or 2) generate an independent, more finely meshed model of only the region of interest, and analyze it. The first option can be time consuming and costly; therefore, the second option was further considered. After comparing several possible approaches, a Global-Local (G-L) hierarchical FE modeling approach was adopted. This approach has several advantages over traditional FE modeling techniques. First, it is a realistic 3-D FE model and can accurately calculate the spatial pavement response to loading. Second, it is capable of handling variable materials such as AC. Finally, through the cut-boundary displacement method, also known as the specified boundary displacement method (ABAQUS 2002), the developed FE model is made very efficient in terms of computing and hardware requirements. It enables users to experiment with different designs (e.g., finer mesh and quasi-static analysis procedure) for the region of interest.

In the first stage (global level) of the G-L approach, the pavement section subjected to loading and boundary conditions was analyzed using a relatively coarse mesh. In the second stage (local level), a more refined mesh was used to model a local part of the pavement section based on interpolation of the solution from the initial, relatively coarse, global model. The size of the local model depends upon the analysis objective and also upon the moving load simulated. The same types of elements as those in the global model analysis were used to mesh the local model. A very fine mesh was applied to the area of interest and to some depth under the pavement surface. The results of the global model were interpolated on the cutting edge of the local model corresponding to different calculation steps, and the interpolation results were applied as boundary conditions to the local model. The interpolated results from the global model solution at the nodes of the local model boundary are known as “driven variables” and define the degrees of freedom at these nodes. The advantage of running FE models in this fashion is that it allows for a convenient way to transfer the results of the global model to the local model. This greatly simplifies the process of simulating almost any area of interest by having to run the global model only once.

Because of symmetry in the transverse direction, only the half width of the truck axle (915 mm) needs to be modeled if an assumption of equal wheel weight is satisfied. Two examples of a comparison of left and right wheel weights are shown in Figure 14. For both Blair and Warren, relatively high R^2 values suggest that it is reasonable to believe the axle weight is evenly distributed to the left and right wheels for these two specific SISSI sites. In the vertical direction, the thickness of the global model was predetermined by the pavement structure (3000 mm). In the longitudinal direction, the finite domain from the infinitely long AC pavement must be properly selected to deliver accurate predictions for stresses and strains in the field.

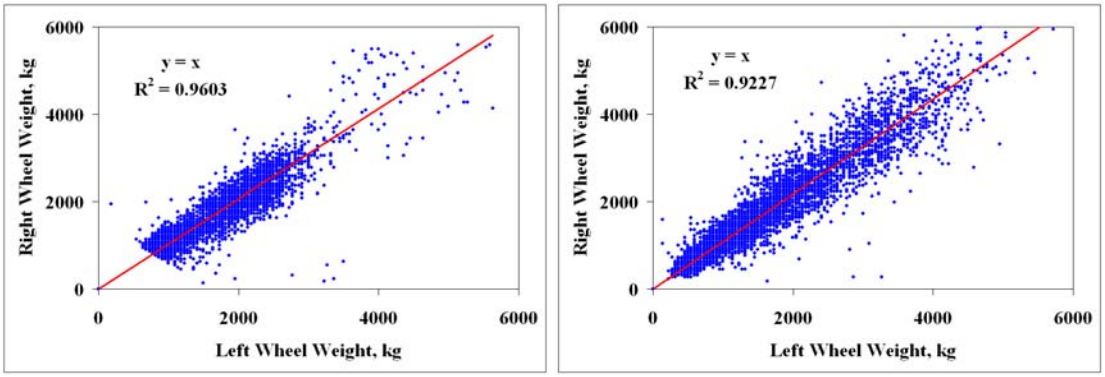

(a) Warren (b) Blair

Figure 14. Comparison of left and right wheel weights

Boundary Conditions

Generally, pavements and their supporting structures are modeled as infinite media in longitudinal and transverse directions; how the unbounded domain is treated is an important issue in FE modeling of pavements. In FE modeling, boundary conditions are usually represented by mathematical models. The mathematical model for the Blair pavement structure is shown in Figure 15. The bottom of the model was prevented from axial movements in the three directions to represent the bedrock (rigid layer) beneath the pavement structure. Kuo et al. (1995) and Zaghloul and White (1993) have successfully adopted such boundary conditions. All the sides of the model were also fixed in all directions except the one at the centerline of the truck axle. This symmetry line was fixed in the y direction, which is perpendicular to the longitudinal direction. This boundary condition setting usually increases the stiffness of the pavement structure and leads to smaller calculated displacements than actual values, especially for points near the truncated boundaries. However, the error due to the boundary effects would be negligible if the model dimensions were chosen to be appropriate. All layers were considered perfectly bonded to one another so that the nodes at the interface of two layers had the same displacement in all three (x, y, and z) directions. This bonding treatment probably represents the interface condition for hot-mix asphalt (HMA) layers more closely than the subbase/subgrade interface, where possibility of slippage is more dominant. These boundary conditions are applicable to the FE models for both Blair and Warren.

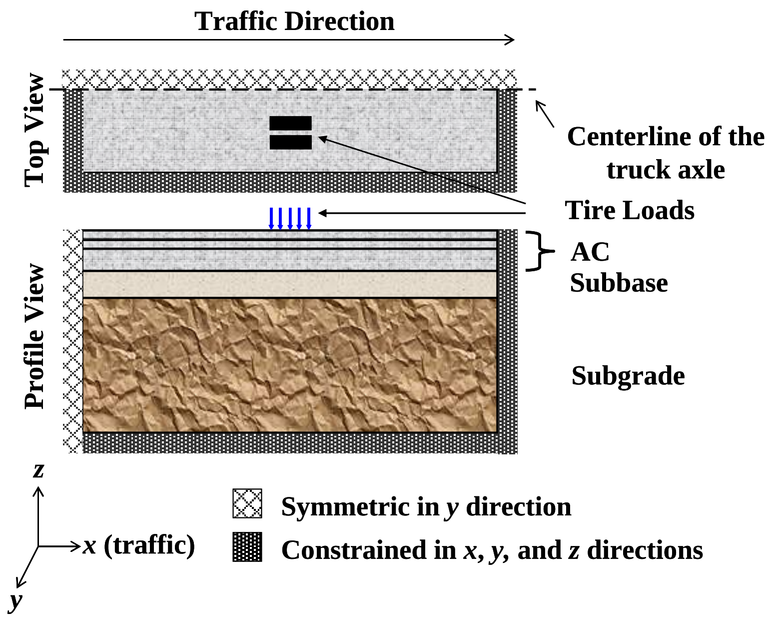

Figure 15. Mathematical model representing the boundary conditions

Material Properties

Among the most important parameters needed as input for mechanistic-empirical pavement design models are the properties of materials used in different pavement layers. In order to obtain properties, the materials were considered in two general categories: bound materials (AC) and unbound materials (fractured PCC at Warren, granular subbase, and subgrade). At high temperatures or under slow loading rates, AC mixtures exhibit a viscous flow, which results in load-associated distresses such as permanent deformation. On the other hand, at low temperatures or under fast cooling rates, an AC mixture becomes stiffer and more brittle, which makes it vulnerable to non-load-associated distresses such as thermal cracking. Fatigue cracking is a more dominant type of distress at intermediate temperatures because a significant part of the traffic load is applied at these temperatures. Granular materials are large conglomerations of discrete macroscopic particles. If they are non-cohesive, then the forces between particles are essentially only repulsive so that the shape of the material is determined by external boundaries and gravity. If they are dry, then any interstitial fluid, such as air, can be neglected in determining many of the flow and static properties. Granular materials typically exhibit a stress-dependent response. The materials become stiffer as higher stress is applied.

Bound Materials

Advances in computing power and material characterization methodologies have led to more sophisticated utilization of constitutive models to realistically predict viscoelastic materials' responses under different loading rates and temperatures. The viscoelastic behavior of AC materials can be represented by a Prony series expansion of the dimensionless shear and bulk relaxation modulus, which is a mathematical formulation for a mechanical analog of viscoelastic materials known as the Wiechert model. The Wiechert model is a parallel combination of sets of springs and dashpots connected in series to each other:

$$E(t) = E_{\infty} + \sum_{1}^{m} E_i e^{-\left(\frac{t}{\rho_i}\right)} \tag{22}$$

where E_{∞} is the long-time relaxation modulus (e.g., at an infinite loading time), E_i are Prony coefficients, and ρ_i are relaxation times that are explicit functions of the dashpot viscosities and corresponding spring stiffnesses. Theoretically, the coefficients E_i can be obtained by assuming a set of ρ_i at regular intervals of one decade (multiples of 10) or one-half decade (half multiples of 10). The advantage that the Prony series has over other viscoelasticity representations is the associated computational efficiency and simplicity. However, owing to experimental constraints such as limitations of machine loading capacity, the relaxation modulus test is rarely conducted in the laboratory. It is well accepted that all linear viscoelastic material functions are mathematically equivalent, and each function contains essentially the same information on the relaxation and creep properties of the material. As a result, a linear viscoelastic material function can be converted into other material functions through appropriate mathematical operations (e.g., from frequency domain to time domain). Consequently, a numerical method was used to obtain shear and bulk relaxation moduli indirectly from frequency-dependent test (complex modulus test) data. Shear and bulk relaxation moduli were computed from $|E^*|$ master curves, as proposed by Schapery and Park (1999):

$$\begin{aligned} G(t) &= \frac{|E^*|\cos\phi}{2\Gamma(1-n)\cos\left(\frac{n\pi}{2}\right)(1+\nu)} \\ K(t) &= \frac{|E^*|\cos\phi}{3\Gamma(1-n)\cos\left(\frac{n\pi}{2}\right)(1-2\nu)} \end{aligned} \tag{23}$$

where *G(t)* is shear relaxation modulus, *K(t)* is bulk relaxation modulus, *ø* is phase angle, *Γ* denotes the gamma function, *υ* is Poisson's ratio, and *n* is the slope of the $|E^*|$ master curve in log-log domain at each point in time. Relaxation moduli at time *t* were also normalized by relaxation moduli at zero time. Shear relaxation modulus and bulk relaxation modulus master curves are plotted in Figures 16 and 17, respectively. At short times, the relaxation modulus is at a high plateau corresponding to the instantaneous response and then falls exponentially to the long-term response as the asphalt molecules gradually accommodate the strain by conformational extension rather than bonding distortion.

One important parameter in Equation 23 is Poisson's ratio. In the infinitesimal deformation of an idealized purely elastic compressible material, one may define a time-independent material constant, called Poisson's ratio, as the ratio of the lateral contraction to the elongation in an infinitesimally small uniaxial extension. In the infinitesimal deformation of any real material (e.g., viscoelastic), the lateral contraction is dependent on loading time or (as is equivalent) frequency. Obtaining the Poisson's ratio of viscoelastic materials is particularly challenging because it requires material testing under both normal and shear stress states under various temperatures and loading rates. Based on recommendations from the MEPDG (ERES 2004), a constant value of 0.30 was assumed for Poisson's ratio of AC mixtures. This magnitude for Poisson's ratio possibly results in smaller strains.

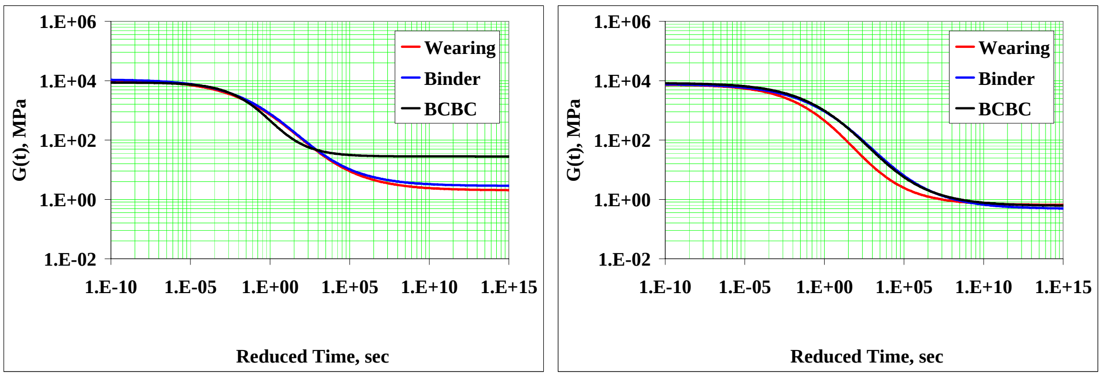

(a) Blair (b) Warren

Figure 16. Shear relaxation modulus master curves

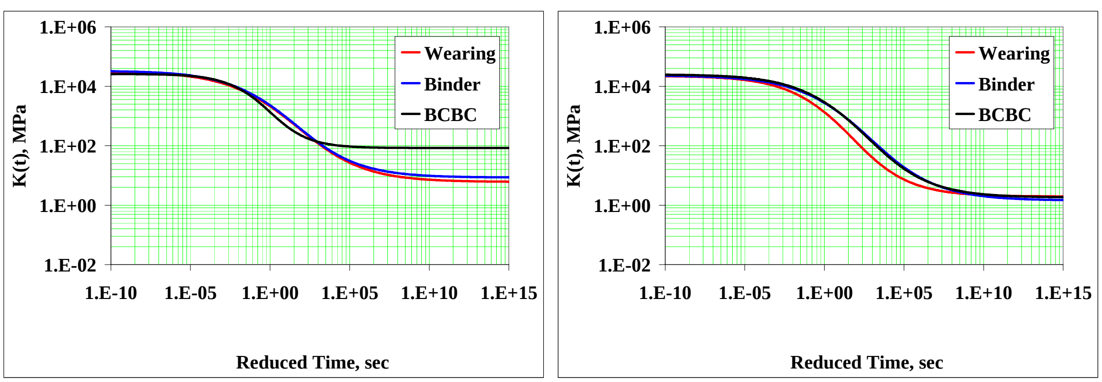

(a) Blair (b) Warren

Figure 17. Bulk relaxation modulus master curves

Unbound Materials

The properties of sublayer materials, such as fractured PCC, subbase and subgrade soils, are often not as well characterized as those of AC. In this study, this difficulty was overcome by backcalculating effective layer moduli from Falling Weight Deflectometer (FWD) data so that the FE model reasonably predicts the response of unbound materials. Backcalculated moduli considering seasonal effects are provided in Tables 8 and Table 9 for Blair and Warren, respectively. These moduli were not varied with depth in the FE model.

Table 8. Summary of backcalculated moduli for unbound materials for Blair

Season	Backcalculated Moduli, MPa		Pavement Temperature, ^{o}C
	Subbase	Subgrade	
Spring	418	106	4-5
Summer	27	209	23-25
Fall	681	114	7-8

Table 9. Summary of backcalculated moduli for unbound materials for Warren

Season	Backcalculated Moduli, MPa		Pavement Temperature, ^{o}C
	PCC	Subgrade	
Spring	278	276	(-3)-(-2)
Summer	456	228	21-23
Fall	159	329	12-13

Simulation of Moving Load

To accurately simulate pavement response to vehicular loading, the contact pressure distribution and dimensions of the contact area between the tire and pavement are required. In the layered theory, because of its use of axisymmetric solutions, the contact area is assumed to be circular although a rectangular shape is more realistic for the tire-pavement contact area. In addition, experimental measurements have shown that the actual loading conditions are non-uniform and depend on the tire construction, tire load, and tire inflation pressure (De Beer 1996). This non-uniform pressure might result because of the stiffening effect of the tire wall. Luo and Prozzi (2005) investigated the effect of the difference between the modeled uniform and the actual distributed pressures on the pavement distress, especially top-down cracking. The authors observed the most significant difference at the pavement surface. Another study by Siddharthan et al. (2002) also reported a significant difference (6 to 30 percent) between the responses computed with uniform and non-uniform contact tire-pavement stress distributions; however, for the case of tensile strain at the bottom of the AC layer, the responses computed with the non-uniform stress distribution are lower. This indicates that the use of uniform load distributions is conservative, at least in the case of the estimation of alligator cracking.

Since it is well documented that the difference in the tire print area configuration is insignificant at greater depths, it was believed that applying a uniform contact pressure over a rectangular tire print area on the pavement surface would be conservative. One advantage of assuming a uniform contact distribution is that the two-solid contact problem was simplified by omitting one of the two solids (i.e., tire) and approximating it by a known stress field. In the field, the actual contact stress between the tire and the pavement is not initially known and depends on the interaction between the tire and the pavement surface. Since pavement responses are of primary interest in this research, the tire was removed, and its interaction was substituted by a known stress field. This allows the local model to be used in different pavement layers, and more realistic time-dependent material properties can be implemented in the analysis.

Contact pressures of the NECEPT truck under different load configurations were calculated from the axle weight and tire print area, as summarized in Table 10. Although different contact pressures may result in different contact areas, for simplicity, averaged dimensions (330 mm by 216 mm) were assumed for all tractor/trailer tires, as shown in Figure 18a. These dimensions correspond to a circular loaded area that has a radius of 150 mm. Uniform contact pressure was then applied on these tire prints.

Table 10. Summary of contact pressure under different load configurations

Axle	Axle Spacing, m			Tire	Contact Pressure, kPa	
					Front Load Configuration	Back Load Configuration
1	4.5			single	454	441
2		1.3		dual	580	384
3			5.8	dual	550	408
4				dual	559	799

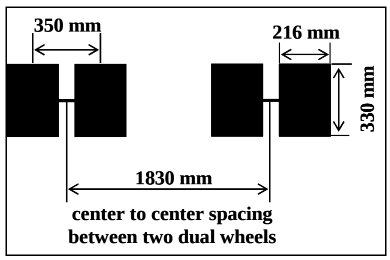

(a) Tire print of the NECEPT truck

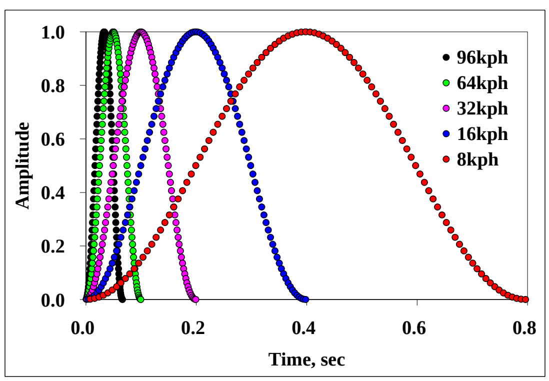

(b) Load amplitude as a function of time

Figure 18. Simulation of moving load

The effect of a moving load on a point in the pavement can be simulated by noting that a time function of the stress can be used to approximate the stress experienced by the point. The relationship between the duration of the moving load and the load amplitude was approximated through a sine function presented by Huang (1993):

$$L(t) = q * \sin^2(\frac{\pi}{2} + \frac{\pi}{d}) \tag{24}$$

where t is the time of loading, d is the load duration, and q is the load amplitude. When the load is at a considerable distance from a given point, or $t = \pm d/2$, the load above the point is zero, or $L(t) = 0$. When the load is directly above the given point, or $t = 0$, the load $L(t) = q$. The duration of the load depends on the vehicle speed V and the tire contact radius a. A reasonable assumption is that the load has practically no effect when it is at a distance of $6a$ from the point under consideration. As a result, the load duration d can be computed as $d = (12*a)/V$. For demonstration purposes, load amplitude curves corresponding to target vehicle speeds in the field are shown in 18b. During FE simulations, actual speeds were used. In the FE model, the duration of the load pulse was assumed to not vary through pavement depths. This assumption is not strictly true for pavements in the field. The AASHTO Road Test (1962) showed that the duration of the load pulse increases with increase in the depth at which it is being observed.

Another concern in simulating moving load is the selection of analysis procedure, quasi-static vs. dynamic. A quasi-static loading assumes any dynamic effects of load are reflected in material properties with arbitrary time histories such as relaxation modulus. On the other hand, dynamic analysis accounts for inertial effects in the pavement structure. It was decided to use quasi-static analysis procedures to simulate the field scenario where the moving load approaches and leaves the area of interest; gradual time-steps were employed. A key component of this method is that all calculations are based entirely on known values from the previous time-step. Consequently, relatively small time-steps are required to provide a stable solution. The time-step taken in ABAQUS is fixed instead of automatically computed by the program in order to ensure an accurate solution.

Element Type

The accuracy of FE solutions depends strongly on the element type used to mesh FE models. In ABAQUS, there are three types of continuum elements available for 3-D FE models: hexahedrons, tetrahedrons, and wedges. There are also linear and quadratic options for each of these basic element shapes. One integration method is "full integration," which refers to the number of Gauss points required to integrate the polynomial terms in an element's stiffness matrix exactly when the element has regular shape. The other integration method is called "reduced integration," which uses one fewer integration point in each direction than the full integration. There is a trade-off between linear and quadratic and also between full integration and reduced integration. In view of the geometric size of the pavement section and preferred accuracy of FE solutions, unbound materials were meshed with 8-node linear brick elements (C3D8R) with reduced integration. This element type has been successfully utilized in FE models for pavement engineering problems (Li and Metcalf 2002, Pirabaroobn et al. 2003). Consequently, these elements act as linear springs to support upper AC layers. Considering the temperature dependency of AC materials, coupled temperature-displacement features that have both displacement and temperature degrees of freedom were also added.

Optimum Element Size

The FE method is an approximation of the exact solution. Element size needs to be carefully selected since it directly affects the level of accuracy obtained from the FE model. The finest mesh is required near the loads to capture the steep stress and strain gradients. Although the local model could have a very fine mesh, the fineness of element mesh for the global model is also important for cost-effectively obtaining accurate response parameters from local models. The "driven variables" for local models are the solutions from the global model. Computational time and data storage space also need to be considered for the desired level of accuracy. The optimum element size was determined through a mesh refinement analysis that evaluates the merits of the FE model's performance in accurately predicting pavement response at multiple depths under a single tire load. It is known that assuming a mesh is convergent just because it has the same element size as a converged mesh in a non-similar model, or at a different location in a similar model, is not valid. Thus, the refinement analysis was performed for Blair and Warren pavement structures separately.

In the FE method, the stresses in an individual element are computed from derivatives of the displacements. The stresses computed from adjacent elements may differ significantly when a coarse element mesh (large element size) is used. The stress differences at the element interfaces (boundaries) decrease as the size of the element is reduced (Bathe 1982). Therefore, a proper FE solution will converge as the number of elements is increased (mesh refinement) to the exact solution. If the stresses are not continuous (large difference) across element boundaries, then the element stresses will not be in equilibrium with externally applied loads. For an ideal continuum pavement system, Bathe's convergence criteria could be employed at the layer interface such that the optimal computational effort would be achieved through appropriate element sizes.

In the mesh refinement analysis, each pavement layer was first meshed with large elements. This coarse element mesh was then refined by subdividing the previous used element into more elements. With this procedure, the new space of FE interpolation functions contains the previously used space. The element mesh is continuously refined until the vertical stress continuity at layer interfaces is obtained. During this mesh refinement process, linear elastic response of pavement materials was assumed, as listed in Tables 11 and 12. Contact pressures of 580 kPa and 790 kPa were uniformly applied over a rectangular tire print area (330 mm by 216 mm) on the pavement surface of Blair and Warren, respectively. These two pressures correspond to the maximum contact pressure values under front and back load configurations.

Table 11. Elastic properties used in mesh refinement analysis for Blair

Layer	Thickness, mm	Elastic Modulus, MPa	Poisson's Ratio
Wearing	54	3000	0.30
Binder	47	2000	0.30
BCBC	162	1000	0.30
Subbase	200	500	0.35
Subgrade	2537	200	0.40

Table 12. Elastic properties used in mesh refinement analysis for Warren

Layer	Thickness, mm	Elastic Modulus, MPa	Poisson's Ratio
Wearing	38	3000	0.30
Binder	62	2000	0.30
BCBC	138	1000	0.30
Leveling	110	2000	0.30
Fractured PCC	250	500	0.35
Subgrade	2402	200	0.40

Mesh performance was evaluated at points along the vertical axis, which is at the center of the loaded area. Tables 13 to 16 summarize the vertical stress differences for different mesh refinements. A graphic presentation of mesh refinement analyses results is shown in Figure 19. It can be seen that the continuity of vertical stresses at a layer interface is highly affected by the element size of the upper layer. Convergence becomes slower when the element size is smaller than a critical size at refinements 3 (R3) and 4 (R4) for the Blair and Warren models, respectively. This critical element size results in a 5 percent stress difference (29.0 and 39.5 kPa) of applied tire load (580 and 790 kPa). The stress difference is further decreased to 1 percent (5.8 and 7.9 kPa) of applied tire load at refinement 6 (R6) for both models. However, the required computational time and data storage space are extremely high for this level of solution accuracy. Therefore, the cut-boundary displacement method was implemented in the mesh refinement analysis. Continuing with a relatively coarse mesh (global model), much smaller elements were used to mesh a local area (local model), which is directly under the wheel load. Mesh refinement analysis results using the G-L modeling approach are presented in Tables 17 and 18. The G-L approach saves a significant amount of the computational time for the current analysis compared with the 3-D FE model without using the cut-boundary displacement method for the same level of accuracy.

Given that an FE model with a 1 percent vertical stress difference at any layer interface would provide an acceptable level of accuracy, optimum element sizes from the G-L approach (Tables 17 and 18) were applied in all developed models in this study to save in computational time while providing an accurate description of the pavement response.

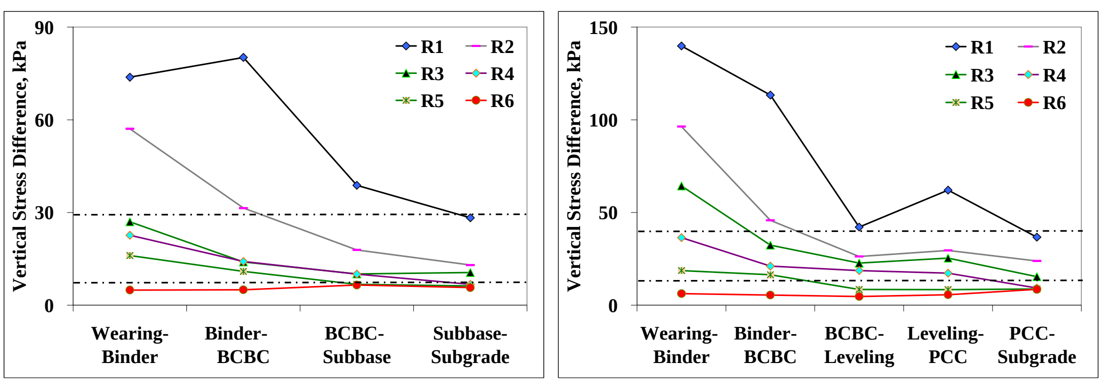

(a) Blair (b) Warren

Figure 19. Results from mesh refinement analysis

Table 13. Mesh refinement analysis results for Blair – I

Mesh Refinement	Layer	Element Size, mm	Number of Elements	Output File Size, Mbytes	Computational Time, sec	Vertical Stress Difference at Layer Interface, kPa			
R1	Wearing	54.0	9180	10.5	49	73.8			
	Binder	47.0					80.2		
	BCBC	54.0						38.8	
	Subbase	100.0							28.3
	Subgrade	253.0							
R2	Wearing	27.0	39400	72.1	279	57.1			
	Binder	23.5					31.4		
	BCBC	27.0						17.9	
	Subbase	40.0							13.0
	Subgrade	126.5							
R3	Wearing	13.5	144096	296.9	3962	27.0			
	Binder	9.4					14.0		
	BCBC	18.0						10.1	
	Subbase	20.0							10.6
	Subgrade	126.5							

Table 14. Mesh refinement analysis results for Blair – II

Mesh Refinement	Layer	Element Size, mm	Number of Elements	Output File Size, Mbytes	Computational Time, sec	Vertical Stress Difference at Layer Interface, kPa			
R4	Wearing	10.8	249228	507.5	12417	22.6			
	Binder	9.4					14.2		
	BCBC	18.0						10.1	
	Subbase	20.0							6.7
	Subgrade	84.3							
R5	Wearing	10.8	353600	1034.8	18520	16.0			
	Binder	9.4					10.9		
	BCBC	9.0						6.8	
	Subbase	20.0							6.2
	Subgrade	84.3							
R6	Wearing	5.4	760240	2156.7	73143	4.9			
	Binder	4.7					5.0		
	BCBC	9.0						6.5	
	Subbase	20.0							5.7
	Subgrade	63.3							

Table 15. Mesh refinement analysis results for Warren – I

Mesh Refinement	Layer	Element Size, mm	Number of Elements	Output File Size, Mbytes	Computational Time, sec	Vertical Stress Different at Layer Interface, kPa				
R1	Wearing	38.1	10530	15.5	77	139.8				
	Binder	62.2					113.3			
	BCBC	46.1						42.2		
	Leveling	110.5							62.1	
	PCC	125.0								36.7
	Subgrade	247.0								
R2	Wearing	19.1	34000	50.8	194	96.4				
	Binder	31.1					45.8			
	BCBC	34.6						26.3		
	Leveling	55.2							29.5	
	PCC	62.5								23.9
	Subgrade	247.0								
R3	Wearing	12.7	86690	168.4	960	64.3				
	Binder	20.7					32.4			
	BCBC	27.7						22.7		
	Leveling	55.2							25.4	
	PCC	50.0								15.4
	Subgrade	123.5								

Table 16. Mesh refinement analysis results for Warren – II

Mesh Refinement	Layer	Element Size, mm	Number of Elements	Output File Size, Mbytes	Computational Time, sec	Vertical Stress Different at Layer Interface, kPa				
R4	Wearing	9.5	185832	481.7	5968	36.4				
	Binder	12.4					21.1			
	BCBC	19.8						18.7		
	Leveling	55.2							17.3	
	PCC	25.0								9.3
	Subgrade	82.3								
R5	Wearing	7.6	341550	982.4	17381	18.7				
	Binder	10.4					16.4			
	BCBC	14.0						8.5		
	Leveling	36.8							8.4	
	PCC	20.8								8.7
	Subgrade	82.3								
R6	Wearing	3.8	910396	3752.4	118590	6.2				
	Binder	6.2					5.5			
	BCBC	9.9						4.7		
	Leveling	22.1							5.6	
	PCC	20.8								8.5
	Subgrade	82.3								

Table 17. G-L-based mesh refinement analysis results for Blair

Mesh Refinement	Layer	Element Size, mm	Number of Elements	Output File Size, Mbytes	Computational Time, sec	Vertical Stress Jump at Layer Interface, kPa			
Global (R3)	Wearing	13.5	144096	296.9	3962	27.0			
	Binder	9.4					14.0		
	BCBC	18.0						10.1	
	Subbase	20.0							10.6
	Subgrade	126.5							
Local	Wearing	5.4	38880	82.6	253	5.0			
	Binder	4.7					4.8		
	BCBC	9.0						6.2	
	Subbase	10.0							2.5
	Subgrade	20.0							

Table 18. G-L-based mesh refinement analysis results for Warren

Mesh Refinement	Layer	Element Size, mm	Number of Elements	Output File Size, Mbytes	Computational Time, sec	Vertical Stress Jump at Layer Interface, kPa				
Global (R4)	Wearing	9.5	185832	481.7	5968	36.4				
	Binder	12.4					21.1			
	BCBC	19.8						18.7		
	Leveling	55.2							17.3	
	PCC	25.0								9.3
	Subgrade	82.3								
Local	Wearing	3.8	37632	79.9	210	6.3				
	Binder	6.2					5.4			
	BCBC	9.9						4.9		
	Leveling	11.0							4.5	
	PCC	12.5								2.6
	Subgrade	20.0								

Model Dimensions

The determination of the global model's longitudinal dimension is presented in this subsection. The same FE models used in the mesh refinement analyses were employed with a length of 6 m. AC layers were modeled as viscoelastic materials. A lower speed produces a larger duration of loading and subsequently larger dimensions of the stress influence zone. A tire load with 8kph vehicle speed was applied on the pavement surface. This was the lowest target speed in the field. Horizontal strain in longitudinal direction and vertical strains were predicted at various spatial locations. Ideally, the change in these two response parameters with increasing distance from the center of loading area will become negligible for a certain set of plane and vertical dimensions. As an example, predictions of response parameters from the Blair FE model are shown in Figure 20. It is clear from Figure 20 that the FE model provides an acceptable description of longitudinal strain response observed in the field, the compression-tension-compression pattern. Both longitudinal and vertical strain curves follow the same trend that the strain magnitude decreases at deeper locations. This trend was also detected in the field response data. Because the tire load has almost no influence on both strain curves at longitudinal distances more than 2 m from the center of loading area, the longitudinal dimension was set at 4 m for both the Blair and Warren FE global models. All layers were modeled with the same shape to preserve the continuity of nodes at the interface of adjacent layers.

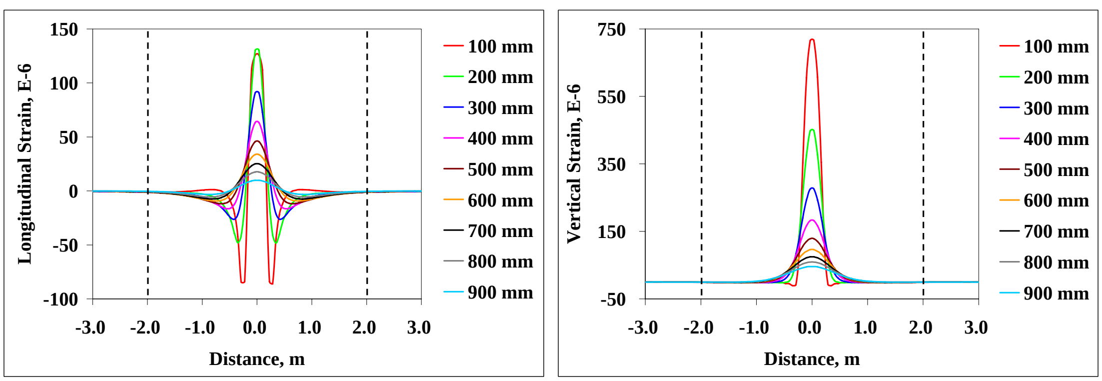

(a) Longitudinal Strain (b) Vertical Strain

Figure 20. Determination of the longitudinal dimension of the global models

Model Validation

Although an effort was made to approach real pavement conditions in the developed FE models based on the available laboratory results and modeling techniques, some approximations were inevitable. Therefore, model validation is an essential step for pavement performance predictions using FE-simulated stress and strain responses. Based on all dynamic measurements collected during the SISSI project, various sets of pavement responses were selected to validate the developed FE models. Selected data sets are shown in Table 19 and Table 20 for Blair and Warren, respectively. These data sets cover various seasons, vehicle speeds, and load configurations. Although strain gauges were also installed at the bottom of the wearing layer at Warren, they stopped responding in 2004. Since other researchers found that the effect of tire wander (between the center of the tire and the instrument) was very significant (Chatti et al. 1996), tire wander was considered in the model validation. An average of two lateral offsets recorded at 7.3 m before and after the centerline of instrumentation was applied in each FE simulation. Both target and actual speeds are reported, but only actual speeds were used to simulate moving loads.

As presented in Chapter 3, all strain gauges were placed in the horizontal plane at the bottom of the AC layers. To provide a thorough evaluation of developed FE models, additional response data (i.e., vertical strains) are desirable. A layered elastic analysis (LEA) program, KENLAYER, was used to compute horizontal strains at the bottom of the wearing and leveling layers at Warren and vertical strains in both bound and unbound layers where measured responses are not available. KENLAYER was selected because it is widely accessible and is included with the textbook *Pavement Analysis and Design* (Huang 1993). With time-temperature superposition, for a specific temperature and actual vehicle speed in the field at the time of pavement response measurement, the elastic modulus was obtained from dynamic modulus master curves. These elastic moduli (Tables 21 and 22) were input in KENLAYER. All locations selected for analyses and comparisons are listed in Tables 23 and 24 for Blair and Warren, respectively. Data sources for each response parameter are also reported.

The effectiveness of developed FE models in simulating pavement response is evaluated in terms of the prediction error at peak strains or stresses, e:

$$e = \frac{R_{FE} - R_{m(KEN)}}{R_{m(KEN)}} * 100 \tag{25}$$

where R_{FE} is the peak response simulated from FE models, R_m is the peak response measured in the field, and R_{KEN} is the peak response calculated from KENLAYER. A positive value of e indicates an over-prediction from FE simulations, while a negative value of e suggests an under-prediction. Although only prediction errors are reported in this section, a complete summary of measured and FE-simulated pavement responses can be found in Appendix B.

Table 19. Selected response data for Blair

Run #	Season	Date	Time	Target Speed, kph	Actual Speed, kph	Load Configuration	Tire Wander, mm
1	Spring	5/4/2004	13:36	32	42	B	38
2	Summer	7/20/2004	10:32	64	61	B	0
3	Summer	7/20/2004	12:25	32	39	F	22
4	Fall	10/21/2004	14:35	32	35	B	0
5	Fall	10/21/2004	15:06	64	68	B	0
6	Spring	3/7/2005	11:22	8	12	B	0
7	Spring	3/7/2005	11:33	32	29	B	0
8	Spring	3/7/2005	11:58	64	64	B	0
9	Spring	3/7/2005	12:57	16	14	F	10
10	Spring	3/7/2005	13:30	32	35	F	25
11	Spring	3/7/2005	13:42	64	66	F	51
12	Summer	8/23/2005	11:32	8	7	F	0
13	Summer	8/23/2005	11:49	64	67	F	0

Table 20. Selected response data for Warren

Run #	Season	Date	Time	Target Speed, kph	Actual Speed, kph	Load Configuration	Tire Wander, mm
1	Summer	6/27/2003	14:00	64	68	B	0
2	Summer	6/27/2003	14:21	96	100	B	0
3	Summer	6/27/2003	14:29	32	36	B	0
4	Summer	8/24/2004	10:33	32	35	F	0
5	Summer	8/24/2004	10:57	64	68	F	29
6	Summer	8/24/2004	11:10	96	101	F	51
7	Summer	8/24/2004	11:56	32	38	B	13
8	Summer	8/24/2004	12:12	64	69	B	32
9	Summer	8/24/2004	12:30	96	99	B	64
10	Fall	11/5/2004	13:06	32	36	F	13
11	Fall	11/5/2004	14:12	64	71	F	38
12	Fall	11/5/2004	14:31	96	96	F	0
13	Fall	11/5/2004	14:54	8	11	B	0
14	Fall	11/5/2004	14:56	32	39	B	38
15	Fall	11/5/2004	15:06	64	65	B	0
16	Fall	11/5/2004	15:16	96	98	B	0
17	Spring	3/17/2005	9:52	32	33	F	25
18	Spring	3/17/2005	10:05	64	66	F	44
19	Spring	3/17/2005	10:32	96	100	F	102
20	Spring	3/17/2005	11:05	32	34	B	22
21	Spring	3/17/2005	11:10	64	68	B	0
22	Spring	3/17/2005	11:29	96	96	B	29

Table 21. Elastic layer moduli for Blair

Run #	Actual Speed, kph	Elastic Layer Moduli					
		Wearing		Binder		BCBC	
		Temp, °C	|E*|, MPa	Temp, °C	|E*|, MPa	Temp, °C	|E*|, MPa
1	42	31	1840	28	2496	18	5288
2	61	31	2106	28	2844	26	2688
3	39	31	1788	28	2428	26	2200
4	35	13	7583	13	8211	12	8464
5	68	13	8717	13	9438	12	10136
6	12	16	4724	12	6866	5	10547
7	29	16	5839	12	8264	5	12636
8	64	17	6697	14	8878	5	14652
9	14	20	3504	17	4939	6	10259
10	35	21	4261	18	5561	6	12560
11	66	21	5057	18	6527	6	14142
12	7	35	613	33	694	29	735
13	67	37	1315	33	1799	29	2076

Table 22. Elastic layer moduli for Warren

Run #	Actual Speed, kph	Elastic Layer Moduli							
		Wearing		Binder		BCBC		Leveling	
		Temp, °C	|E*|, MPa	Temp, °C	|E*|, MPa	Temp, °C	|E*|, MPa	Temp, °C	|E*|, MPa
1	68	39	525	34	2277	32	2763	32	2648
2	100	41	505	35	2395	34	2689	33	2778
3	36	41	301	35	1683	34	1845	33	1987
4	35	31	1015	24	3986	22	4883	22	4489
5	68	32	1228	25	4466	23	5469	23	4993
6	101	32	1441	25	4901	23	5998	23	5448
7	38	38	440	29	2740	27	3340	27	3373
8	69	38	588	29	3269	27	3998	27	3964
9	99	40	561	31	3180	28	4161	28	3866
10	36	11	6350	9	9493	8	10990	8	9792
11	71	12	6950	11	9438	11	10590	10	9737
12	96	13	7066	11	9840	11	11044	10	10136
13	11	12	4469	12	6733	10	8525	9	7932
14	39	12	6086	12	8342	10	10375	9	9549
15	65	12	6848	12	9046	10	11161	9	10239
16	98	12	7428	12	9563	10	11730	9	10741
17	33	7	8243	3	11694	2	13430	1	12503
18	66	7	9256	3	12478	2	14250	1	13245
19	100	10	8511	5	12177	4	14212	3	12960
20	34	11	6222	8	9674	7	11524	5	10848
21	68	11	7253	8	10591	7	12527	5	11725
22	96	14	6403	9	10720	7	9680	6	11847

Table 23. Summary of analysis locations for Blair

Analysis Location	Depth, mm	Response Parameter		
		Horizontal Strain	Vertical Stress	Vertical Strain
Bottom of Wearing	54	Measured	-	KENLAYER
Bottom of Binder	101	Measured	-	KENLAYER
Bottom of BCBC	263	Measured	-	KENLAYER
Top of Subbase	263	-	Measured	KENLAYER
Top of Subgrade	463	-	Measured	KENLAYER

Table 24 Summary of analysis locations for Warren

Analysis Location	Depth, mm	Response Parameter	
		Horizontal Strain	Vertical Strain
Bottom of Wearing	38	KENLAYER	KENLAYER
Bottom of Binder	100	Measured	KENLAYER
Bottom of BCBC	239	Measured	KENLAYER
Bottom of Leveling	349	KENLAYER	KENLAYER
Top of Fractured PCC	349	KENLAYER	KENLAYER
Top of Subgrade	599	KENLAYER	KENLAYER

Comparison of FEA and Measured Responses

Blair FE Model

Based on the function and location of instrumented dynamic sensors, prediction errors are tabulated in Tables 25 and 26 for strains in the AC layers and stresses in the unbound layers, respectively. In general, the Blair FE model seems to under-predict pavement responses in AC materials. The main conclusions of strain predictions can be made as follows:

- FE model is capable of simulating pavement responses under different load configurations.
- FE model results in a slightly larger prediction error at the bottom of the wearing layer. This is possibly due the simplification of contact pressure distribution at the pavement surface.
- FE model predicts smaller strains (a larger prediction error) during warm seasons. Since AC materials are modeled in viscoelastic mode, experiment tests other than the complex modulus test, such as the creep-recovery test, are needed to capture the viscoplastic behavior of AC such that the accuracy of strain predictions at high temperatures can be improved.
- One interesting observation in Table 25 is that strain responses under axle 3 are much smaller than field-measured values, particularly at higher speeds, i.e., 64 kph. This phenomenon is shown in Figure 21a. If the next pass of the tire load comes before the complete relaxation of strains has taken place, the unrecovered inelastic (residual) strains may cause permanent deformation. From the dimensions of the NECEPT truck, the axle spacing between axle 2 (second axle of the tractor) and 3 (first axle of the trailer) is much shorter than the other two axle spacings. At 64 kph, a travel time of 0.073 sec may not be enough for the pavement to rebound before the arrival of the third pass of the tire load.

On the other hand, the Blair FE model always over-predicts response in granular materials. The main conclusions of stress predictions can be made as follows:

- No obvious dependency of prediction error on load configuration, axle, and vehicle speed has been observed.
- The prediction error decreases as deeper points in the pavement are considered.
- Prediction errors are quite large in the summer. This is probably due to the low subbase modulus backcalculated from FWD data. Further improvements on the accuracy of stress response prediction require soil characterization tests, such as the resilient modulus test.

For all the selected response data sets, the FE model accuracy is acceptable, with an overall error of -11.2 percent in predicting longitudinal strains and 14.3 percent in predicting vertical stresses. Hence, the assessment is that the Blair FE model provides a satisfactory prediction of pavement response to vehicular loading.

Warren FE Model

Because no pressure cells were installed at Warren, only strain prediction errors are summarized in Table 27. Similarly to the Blair FE model, the Warren FE model seems to under-predict pavement responses in AC materials. However, an overall prediction error of -7.8 percent suggests a better agreement between measured and predicted longitudinal strains. Several conclusions of strain predictions can be made as follows:

- Load configuration (front vs. back) has no impact on strain predictions.
- The trend that the prediction error is smaller at a deeper location is not clear.
- The inability to simulate strain responses at high temperature is apparent due to the viscoelastic mode included in the FE model.
- Potential permanent deformations occur between the second and third passes of tire load, as shown in Figure 21b. At the highest vehicle speed (96kph), the time gap between the middle two axles of the tractor trailer is only 0.049sec.

Table 25. Summary of strain prediction errors (%) of Blair FE model

Analysis Conditions		Prediction Error, %
Overall		-11.2
Load Configuration	Front	-11.1
	Back	-11.3
Analysis Location	Bottom of Wearing	-13.1
	Bottom of Binder	-10.5
	Bottom of BCBC	-10.0
Season	Spring	-9.5
	Summer	-14.3
	Fall	-9.9
Axle	1	-10.5
	2	-10.5
	3	-13.7
	4	-10.4
Vehicle Speed, kph	8	-10.6
	16	-10.9
	32	-11.2
	64	-12.3

Table 26. Summary of stress prediction errors (%) of Blair FE model

Analysis Conditions		Prediction Error, %
Overall		14.3
Load Configuration	Front	14.3
	Back	14.3
Analysis Location	Top of Subbase	15.1
	Top of Subgrade	13.5
Season	Spring	13.0
	Summer	16.4
	Fall	13.5
Axle	1	14.3
	2	14.2
	3	14.3
	4	14.4
Vehicle Speed, kph	8	14.1
	16	14.5
	32	14.0
	64	14.4

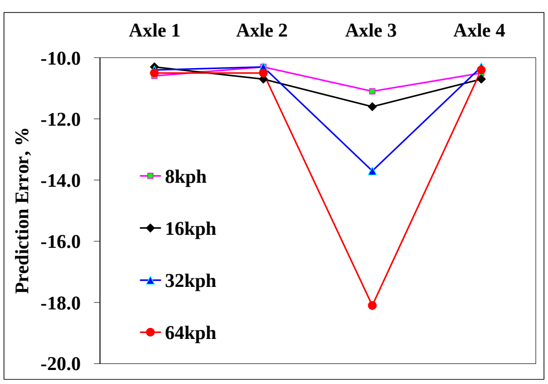

(a) Blair

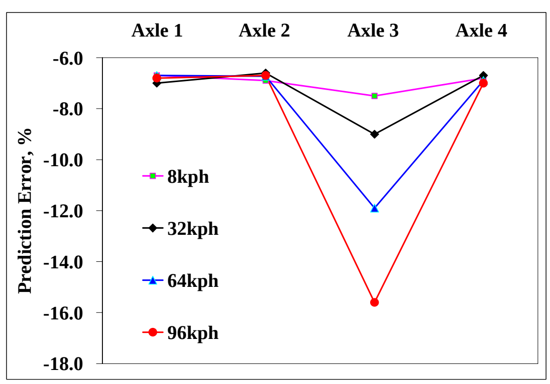

(b) Warren

Figure 21. Prediction errors for different axles and target speeds

Table 27. Summary of strain prediction errors (%) of Warren FE model

Analysis Conditions		Prediction Error, %
Overall		-7.8
Load Configuration	Front	-7.8
	Back	-7.8
Analysis Location	Bottom of Binder	-7.9
	Bottom of BCBC	-7.7
Season	Spring	-6.6
	Summer	-10.5
	Fall	-6.3
Axle	1	-6.8
	2	-6.7
	3	-11.0
	4	-6.9
Vehicle Speed, kph	16	-7.0
	32	-7.3
	64	-8.1
	96	-9.0

Comparison of FEA and KENLAYER

Horizontal strains at deeper locations of bound layers and vertical strains in unbound layers were not captured by field instrumentation at the SISSI sites. To further verify the developed FE models, the responses at these locations from FE solutions were compared with LEA solutions. Comparisons were only made with strain responses under the fourth axle of the NECEPT truck. A radius of 150mm was chosen for the circular contact area in KENLAYER. This radius corresponds to an equivalent contact area as measured for the NECEPT truck.

Tables 28 to 30 summarize the prediction errors of FE models as compared to LEA solutions from KENLAYER. As shown in these tables, FE models have poor agreement with KENLAYER. In general, FE models seem to under-predict both vertical strains and horizontal strains regardless of load configurations. An overall prediction error is about 22 percent for vertical strains and 35 percent for horizontal strains.

Several conclusions on vertical strain predictions can be made as follows:

- No obvious dependency of prediction error on vehicle speed has been observed.
- Prediction errors are relatively larger in summer than in spring and fall.

Several conclusions on horizontal strain predictions can be made as follows:

- Prediction error is highly dependent upon the analysis location, vehicle speed, and pavement temperature.
- The prediction error of horizontal strains decreases as deeper points in the pavement are considered. This is probably due to the viscoelastic nature of AC materials, whereas the elastic mode is incorporated into KENLAYER.

Table 28. Summary of vertical strain prediction errors (%) from Blair FE model

Analysis Conditions		Prediction Error, %
Overall		-22.4
Load Configuration	Front	-23.8
	Back	-21.0
Analysis Location	Top of Binder	-26.0
	Top of BCBC	-22.0
	Top of Subbase	-21.2
	Top of Subgrade	-20.6
Season	Spring	-20.1
	Summer	-26.4
	Fall	-20.6
Vehicle Speed, kph	8	-22.4
	16	-22.5
	32	-22.5
	64	-22.3

Table 29. Summary of horizontal strain prediction errors (%) from Warren FE model

Analysis Conditions		Prediction Error, %
Overall		-35.6
Load Configuration	Front	-35.2
	Back	-36.3
Analysis Location	Bottom of Wearing	-37.4
	Bottom of Leveling	-33.8
Season	Spring	-34.8
	Summer	-39.4
	Fall	-32.8
Vehicle Speed, kph	8	-37.9
	16	-37.1
	32	-34.0
	64	-32.8

Table 30. Summary of vertical strain prediction errors (%) from Warren FE model

Analysis Conditions		Prediction Error, %
Overall		-22.3
Load Configuration	Front	-22.0
	Back	-22.5
Analysis Location	Top of Binder	-26.7
	Top of BCBC	-23.5
	Top of Leveling	-20.8
	Top of Fracture PCC	-20.3
	Top of Subgrade	-20.1
Season	Spring	-20.0
	Summer	-24.1
	Fall	-22.4
Vehicle Speed, kph	8	-21.2
	16	-22.9
	32	-22.9
	64	-22.5

Linearity of Pavement Response

As discussed in previous sections, linear viscoelastic and elastic behaviors were assumed for bound and unbound materials. These assumptions imply that the response (stress or strain) is linearly proportional to the applied load; that is, as the load increases or decreases on the pavement surface, the response at a given point will increase or decrease linearly. In order to verify the above assumption of linearity, two sets of analyses were conducted using the developed Blair and Warren FE models separately. To exclude the tire wander effect, three runs were first selected from each site, Blair (runs #4, 8 and 12) and Warren (runs #3, 13 and 21). These runs cover all three seasons in which dynamic data were collected in the field. Then, for each run, the contact pressure was increased at a 100-kPa interval while vehicle speed and pavement temperature were kept constant. FE-simulated strain responses at various load levels are shown in Figure 22 and Figure 23. Figure 22 shows the tensile strains at the bottom of the BCBC layer, whereas Figure 23 shows the compressive strains at the top of the subgrade as a function of load level. Responses at these two locations are critical for the determination of distresses, such as fatigue cracking and permanent deformation in the respective layers. The linear relationship between the contact pressure and the response clearly validates the assumption of linearity. For both Blair and Warren FE models, as the load increases, the response also increases proportionally. As expected, this trend is pronounced at higher temperatures, which results in lower stiffness of AC materials.

In the case of computing pavement responses under real traffic conditions, the linear relationship between load and response can be used to reduce the computational cost. For example, if the axle load of passing vehicles is known, then the responses for the entire load spectrum can be obtained by load proportionality. More details on such applications are covered in the next chapter.

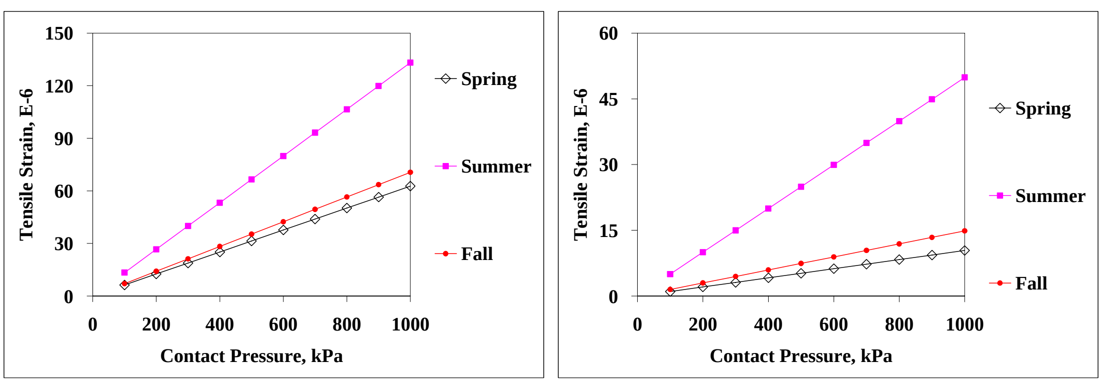

(a) Blair, BCBC

(b) Warren, Leveling

Figure 22. Tensile strains at the bottom of the last AC layer

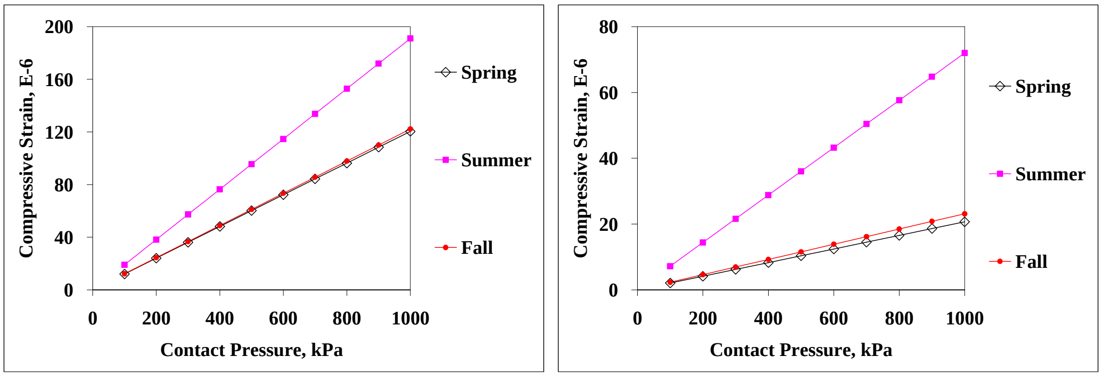

(a) Blair (b) Warren

Figure 23. Compressive strains at the top of subgrade

Summary

This chapter presents an application of 3-D FE models of two AC pavement structures to simulate pavement responses to multiple axle loads with different load configurations, vehicle speeds, and seasons. Key FE modeling parameters such as model dimensions, material properties, load and boundary conditions, element type, and mesh refinement are covered in detail. Each of these factors affects the overall FEA efficiency. In the FE model, bound materials were modeled in a viscoelastic mode, and unbound materials were modeled in an elastic mode. With appropriate element type and mesh density, developed FE models provide acceptable predictions of pavement response as compared to field-measured values and LEA solutions. The adopted Global-Local (G-L) FE modeling strategy has been shown to be effective in reducing computational cost and obtaining accurate predictions.

CHAPTER 6: SIMULATING FLEXIBLE PAVEMENT RESPONSE TO FWD LOADS: A MECHANISTIC APPROACH

Introduction

Mechanistic-empirical design procedures for flexible pavements utilize mechanistic models to predict pavement responses, such as stresses and strains. One of the most important parameters required by the response models is the modulus of each pavement layer. Two basic means of obtaining layer material properties are laboratory and in-situ testing. Typical laboratory tests for asphalt concrete (AC) materials include the complex modulus (E*) test, the indirect tensile test (IDT), and tests related to the shear stiffness (G*) measured using the simple shear tester (SST) at low, intermediate, and high test temperatures. The resilient modulus test is performed to determine the moduli of granular materials (e.g., base, subbase, and subgrade). For decades, pavement engineers have worked with both laboratory and in-situ data, often using the laboratory results for new design and new layers, and the in-situ results from nondestructive testing for rehabilitation and pavement management.

The use of in-situ layer moduli has become an integral part of structural evaluation and rehabilitation design for pavements. It provides valuable information on the behavior or response of pavement structures subjected to traffic loads and the interaction between pavement layers. The in-situ layer moduli are typically obtained by falling weight deflectometer (FWD) testing and backcalculation analysis. Most of the backcalculation analyses in use today are based upon layered elastic theory to calculate the modulus of elasticity for each pavement layer, such that the difference between the measured and predicted deflection basins is minimal. Some backcalculation programs also account for the viscoelastic and/or nonlinear material behavior. Backcalculated layer moduli from FWD deflection data can be used to determine the resilient modulus of different pavement layers. There are some uncertainties related to the backcalculation because only one single modulus value per pavement layer can be obtained with no sufficient discrimination of the near-surface AC moduli. Furthermore, various studies reported that backcalculated moduli usually differ significantly from those obtained through laboratory testing; no consensus exists regarding which procedure provides the most appropriate moduli values for pavement design.

The goal of this research is to integrate in-situ tests, laboratory material characterization, backcalculation, and FEA in a rational manner such that flexible pavements' responses to FWD loads can be numerically simulated. At this stage, only one instrumented full-depth AC pavement was studied, and the laboratory characterization was focused on the bituminous layers. To achieve the research goal, a three-phase mechanistic approach was taken, as illustrated in Figure 24.

Pavement Response Predictions

The general purpose finite element software ABAQUS was used to compute surface deflections, horizontal strains in the AC layers, and vertical stresses in the subbase and subgrade. The same pavement structure used in backcalculation was utilized. Key considerations of 3-D FE modeling, such as boundary conditions, analysis procedures, and element selection are detailed elsewhere (14) since the FE model was developed for other analyses of the pavement section. Both backcalculated and laboratory-derived AC moduli were used in FE simulations such that broad conclusions can be drawn. Measured and simulated pavement responses to FWD loads are tabulated in Tables 31 to 38.

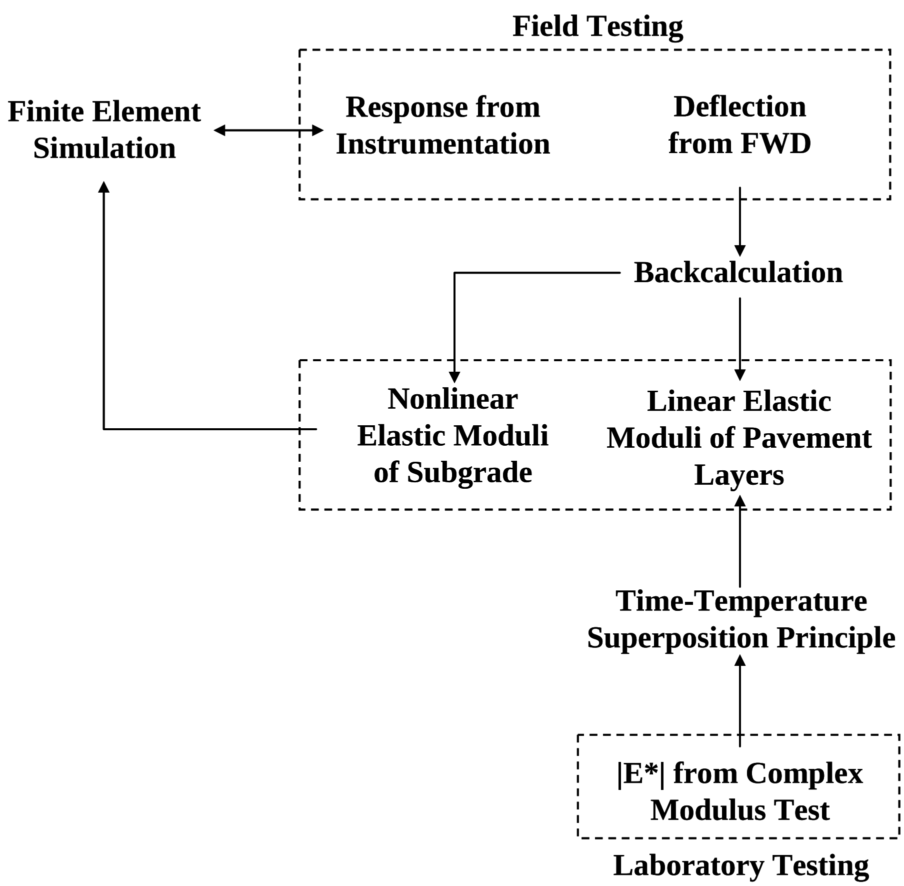

Figure 24. Research approach

Table 31. Summary of measured and predicted deflections at location 1

Measurement Repetition	Distance from Load, mm (in)	Load Level 1			Load Level 2			Load Level 3			Load Level 4		
		M[a]	P_B[b]	P_L[c]	M	P_B	P_L	M	P_B	P_L	M	P_B	P_L
1	0 (0)	0.096	0.097	0.107	0.136	0.132	0.145	0.192	0.177	0.195	0.259	0.227	0.231
	12 (305)	0.070	0.075	0.082	0.102	0.103	0.113	0.146	0.139	0.153	0.199	0.179	0.197
	24 (610)	0.047	0.052	0.056	0.070	0.071	0.077	0.102	0.095	0.105	0.140	0.123	0.136
	36 (914)	0.030	0.036	0.040	0.045	0.049	0.055	0.066	0.067	0.075	0.092	0.087	0.097
	48 (1219)	0.018	0.025	0.029	0.028	0.035	0.040	0.041	0.048	0.054	0.058	0.063	0.071
	60 (1524)	0.011	0.019	0.022	0.017	0.027	0.030	0.025	0.037	0.041	0.036	0.048	0.054
2	0 (0)	0.096	0.095	0.103	0.137	0.129	0.140	0.193	0.173	0.189	0.259	0.221	0.224
	12 (305)	0.070	0.073	0.080	0.103	0.100	0.109	0.147	0.135	0.148	0.200	0.174	0.191
	24 (610)	0.047	0.050	0.055	0.070	0.069	0.075	0.102	0.094	0.102	0.140	0.119	0.132
	36 (914)	0.030	0.034	0.038	0.045	0.047	0.053	0.067	0.065	0.072	0.092	0.084	0.094
	48 (1219)	0.018	0.025	0.028	0.028	0.034	0.038	0.042	0.047	0.052	0.058	0.061	0.068
	60 (1524)	0.011	0.019	0.021	0.017	0.026	0.029	0.025	0.036	0.040	0.036	0.046	0.052
3	0 (0)	0.095	0.092	0.101	0.137	0.126	0.137	0.193	0.169	0.185	0.258	0.217	0.220
	12 (305)	0.070	0.071	0.078	0.102	0.097	0.107	0.146	0.132	0.145	0.198	0.171	0.188
	24 (610)	0.047	0.049	0.054	0.070	0.067	0.073	0.102	0.091	0.099	0.140	0.117	0.129
	36 (914)	0.030	0.033	0.037	0.045	0.046	0.052	0.066	0.063	0.071	0.092	0.082	0.092
	48 (1219)	0.018	0.024	0.027	0.028	0.033	0.037	0.041	0.046	0.051	0.058	0.060	0.067
	60 (1524)	0.011	0.018	0.020	0.017	0.025	0.028	0.025	0.034	0.039	0.036	0.045	0.051

[a] Measured deflection
[b] Predicted deflection using backcalculated AC moduli
[c] Predicted deflection using laboratory-derived AC moduli

Table 32. Summary of measured and predicted deflections at location 2

Measurement Repetition	Distance from Load, mm (in)	Load Level 1			Load Level 2			Load Level 3			Load Level 4		
		M[a]	P_B[b]	P_L[c]	M	P_B	P_L	M	P_B	P_L	M	P_B	P_L
1	0 (0)	0.093	0.096	0.105	0.134	0.129	0.142	0.189	0.173	0.190	0.254	0.222	0.226
	12 (305)	0.071	0.074	0.081	0.102	0.101	0.111	0.146	0.136	0.149	0.197	0.175	0.193
	24 (610)	0.047	0.051	0.055	0.070	0.070	0.076	0.101	0.093	0.103	0.138	0.120	0.134
	36 (914)	0.030	0.035	0.039	0.045	0.048	0.054	0.065	0.066	0.073	0.090	0.086	0.095
	48 (1219)	0.018	0.025	0.028	0.027	0.035	0.039	0.040	0.047	0.053	0.056	0.062	0.069
	60 (1524)	0.011	0.019	0.021	0.017	0.026	0.030	0.025	0.036	0.040	0.034	0.047	0.053
2	0 (0)	0.094	0.094	0.103	0.134	0.127	0.138	0.190	0.171	0.186	0.254	0.219	0.239
	12 (305)	0.071	0.072	0.079	0.102	0.098	0.107	0.146	0.132	0.145	0.197	0.171	0.188
	24 (610)	0.047	0.049	0.055	0.070	0.067	0.073	0.101	0.091	0.099	0.138	0.119	0.129
	36 (914)	0.030	0.034	0.038	0.045	0.046	0.052	0.065	0.063	0.070	0.090	0.082	0.092
	48 (1219)	0.018	0.024	0.027	0.027	0.033	0.037	0.040	0.046	0.051	0.056	0.060	0.067
	60 (1524)	0.011	0.018	0.021	0.017	0.025	0.028	0.025	0.035	0.039	0.035	0.046	0.051
3	0 (0)	0.093	0.092	0.101	0.134	0.123	0.135	0.189	0.166	0.181	0.254	0.214	0.234
	12 (305)	0.070	0.070	0.077	0.102	0.095	0.104	0.146	0.128	0.141	0.197	0.167	0.184
	24 (610)	0.047	0.048	0.053	0.070	0.065	0.072	0.101	0.089	0.096	0.138	0.116	0.126
	36 (914)	0.030	0.033	0.036	0.045	0.045	0.050	0.065	0.061	0.068	0.090	0.080	0.089
	48 (1219)	0.018	0.023	0.026	0.027	0.032	0.036	0.040	0.044	0.049	0.055	0.058	0.065
	60 (1524)	0.011	0.018	0.020	0.016	0.024	0.027	0.025	0.033	0.037	0.034	0.044	0.049

[a] Measured deflection
[b] Predicted deflection using backcalculated AC moduli
[c] Predicted deflection using laboratory-derived AC moduli

Table 33. Summary of measured and predicted deflections at location 3

Measurement Repetition	Distance from Load, mm (in)	Load Level 1			Load Level 2			Load Level 3			Load Level 4		
		M[a]	P_B[b]	P_L[c]	M	P_B	P_L	M	P_B	P_L	M	P_B	P_L
1	0 (0)	0.119	0.146	0.106	0.169	0.198	0.180	0.236	0.265	0.241	0.315	0.341	0.287
	12 (305)	0.096	0.112	0.082	0.137	0.154	0.140	0.191	0.207	0.189	0.256	0.268	0.245
	24 (610)	0.070	0.077	0.056	0.101	0.106	0.096	0.142	0.144	0.130	0.191	0.183	0.169
	36 (914)	0.049	0.053	0.039	0.071	0.073	0.068	0.101	0.100	0.093	0.136	0.130	0.121
	48 (1219)	0.034	0.038	0.029	0.049	0.053	0.050	0.070	0.072	0.068	0.095	0.095	0.088
	60 (1524)	0.023	0.029	0.022	0.034	0.040	0.038	0.048	0.055	0.052	0.065	0.072	0.068
2	0 (0)	0.119	0.147	0.107	0.171	0.200	0.182	0.237	0.268	0.226	0.315	0.320	0.292
	12 (305)	0.096	0.114	0.083	0.138	0.156	0.143	0.192	0.211	0.193	0.255	0.273	0.250
	24 (610)	0.070	0.079	0.057	0.102	0.107	0.098	0.143	0.145	0.134	0.191	0.189	0.174
	36 (914)	0.049	0.054	0.041	0.072	0.075	0.070	0.102	0.103	0.096	0.137	0.134	0.125
	48 (1219)	0.034	0.039	0.029	0.050	0.054	0.051	0.071	0.074	0.069	0.095	0.097	0.091
	60 (1524)	0.023	0.030	0.022	0.034	0.041	0.039	0.049	0.056	0.053	0.066	0.074	0.069
3	0 (0)	0.119	0.145	0.106	0.172	0.197	0.179	0.238	0.263	0.240	0.315	0.339	0.286
	12 (305)	0.095	0.111	0.081	0.138	0.152	0.139	0.192	0.205	0.188	0.256	0.266	0.244
	24 (610)	0.070	0.076	0.056	0.102	0.105	0.095	0.143	0.142	0.129	0.192	0.182	0.168
	36 (914)	0.049	0.052	0.039	0.072	0.072	0.067	0.102	0.098	0.091	0.137	0.128	0.119
	48 (1219)	0.034	0.037	0.028	0.050	0.052	0.048	0.070	0.070	0.066	0.095	0.093	0.086
	60 (1524)	0.023	0.028	0.021	0.034	0.039	0.037	0.049	0.053	0.050	0.066	0.070	0.066

[a] Measured deflection
[b] Predicted deflection using backcalculated AC moduli
[c] Predicted deflection using laboratory-derived AC moduli

Table 34. Summary of measured and predicted horizontal strains at the bottom of wearing layer (E-6)

Testing Location	Measurement Repetition	LL-1[a] M[b]	LL-1 P_B[c]	LL-1 P_L[d]	LL-2 M	LL-2 P_B	LL-2 P_L	LL-3 M	LL-3 P_B	LL-3 P_L	LL-4 M	LL-4 P_B	LL-4 P_L
1	1	6.8	10.1	11.2	8.8	12.5	16.9	11.9	17.9	19.6	15.4	23.9	26.4
1	2	7.2	10.2	11.1	9.3	12.5	16.7	11.6	17.8	19.3	15.8	23.8	26.0
1	3	7.5	10.1	11.2	8.9	12.4	16.7	11.9	17.6	19.3	15.6	23.5	26.0
2	1	7.2	10.7	11.9	8.1	12.9	14.0	11.5	18.2	19.9	15.2	24.2	26.8
2	2	6.8	10.2	10.9	8.6	12.3	13.0	12.1	17.6	18.9	15.7	23.6	25.7
2	3	6.8	10.0	11.1	8.7	12.2	13.1	12.2	17.3	18.9	16.4	23.3	25.7
3	1	6.9	10.3	11.0	8.9	12.7	13.3	11.5	18.1	19.2	14.7	24.2	26.1
3	2	6.0	10.7	11.7	8.4	13.0	14.0	11.2	18.5	20.0	16.0	24.6	27.0
3	3	7.4	10.0	10.9	9.4	12.4	13.2	11.7	17.7	19.1	15.4	23.8	26.0

[a] FWD load level
[b] Measured horizontal strain
[c] Predicted horizontal strain using backcalculated AC moduli
[d] Predicted horizontal strain using laboratory-derived AC moduli

Table 35 . Summary of measured and predicted horizontal strains at the bottom of binder layer (E-6)

Testing Location	Measurement Repetition	LL-1[a] M[b]	LL-1 P_B[c]	LL-1 P_L[d]	LL-2 M	LL-2 P_B	LL-2 P_L	LL-3 M	LL-3 P_B	LL-3 P_L	LL-4 M	LL-4 P_B	LL-4 P_L
1	1	3.0	3.9	5.1	4.4	5.2	6.8	6.5	7.7	8.9	9.2	10.9	11.2
1	2	2.9	3.8	5.0	4.2	5.1	6.6	6.2	7.4	8.7	8.6	10.6	10.8
1	3	2.9	3.7	4.9	4.6	5.0	6.5	7.0	7.3	8.5	8.9	10.3	10.6
2	1	3.0	3.8	5.0	4.3	5.0	6.6	6.7	7.3	8.6	8.8	10.4	10.7
2	2	3.0	3.9	5.0	4.4	5.1	6.6	6.5	7.4	8.6	9.2	10.6	10.8
2	3	2.8	3.8	4.9	4.6	5.0	6.5	6.4	7.2	8.5	9.6	10.3	10.6
3	1	3.0	3.9	5.1	4.1	5.2	6.7	6.6	7.6	8.8	9.5	10.9	11.1
3	2	3.0	3.9	5.0	3.8	5.2	6.7	6.2	7.5	8.8	9.8	10.8	11.0
3	3	3.0	3.9	5.1	4.3	5.2	6.8	6.4	7.7	8.9	8.9	10.9	11.2

[a] FWD load level
[b] Measured horizontal strain
[c] Predicted horizontal strain using backcalculated AC moduli
[d] Predicted horizontal strain using laboratory-derived AC moduli

Table 36. Summary of measured and predicted horizontal strains at the bottom of BCBC layer (E-6)

Testing Location	Measurement Repetition	LL-1[a] M[b]	LL-1 P_B[c]	LL-1 P_L[d]	LL-2 M	LL-2 P_B	LL-2 P_L	LL-3 M	LL-3 P_B	LL-3 P_L	LL-4 M	LL-4 P_B	LL-4 P_L
1	1	1.4	1.7	2.2	2.2	2.7	3.0	3.6	4.3	5.1	5.4	7.0	7.8
1	2	1.3	1.7	2.1	2.2	2.6	2.9	3.7	4.3	5.0	5.0	6.9	7.7
1	3	1.3	1.6	2.1	2.1	2.6	2.9	3.7	4.2	4.9	5.7	6.8	7.6
2	1	1.4	1.7	2.2	2.2	2.6	3.0	3.4	4.3	5.0	5.3	6.9	7.7
2	2	1.3	1.7	2.2	2.1	2.6	2.9	3.6	4.3	4.9	5.9	6.9	7.7
2	3	1.3	1.6	2.1	2.3	2.6	2.9	3.5	4.2	4.9	5.3	6.8	7.6
3	1	1.3	1.7	2.2	2.4	2.7	3.0	3.6	4.4	5.0	5.8	7.0	7.8
3	2	1.4	1.7	2.2	2.3	2.7	3.0	3.8	4.3	5.0	4.7	7.0	7.8
3	3	1.2	1.7	2.2	2.1	2.7	3.0	3.6	4.3	5.0	5.3	7.0	7.8

[a] FWD load level
[b] Measured horizontal strain
[c] Predicted horizontal strain using backcalculated AC moduli
[d] Predicted horizontal strain using laboratory-derived AC moduli

Table 37. Summary of measured and predicted vertical stresses at the top of subbase (kPa)

Testing Location	Measurement Repetition	LL-1[a] M[b]	LL-1 P_B[c]	LL-1 P_L[d]	LL-2 M	LL-2 P_B	LL-2 P_L	LL-3 M	LL-3 P_B	LL-3 P_L	LL-4 M	LL-4 P_B	LL-4 P_L
1	1	1.9	2.2	2.2	2.6	3.0	3.1	3.3	4.1	4.1	4.2	5.3	5.3
1	2	1.9	2.3	2.3	2.5	3.1	3.1	3.5	4.2	4.2	4.2	5.4	5.4
1	3	1.9	2.2	2.3	2.5	3.1	3.1	3.2	4.1	4.2	4.1	5.4	5.4
2	1	1.8	2.3	2.3	2.5	3.1	3.1	3.3	4.1	4.2	4.0	5.4	5.4
2	2	1.9	2.4	2.4	2.7	3.2	3.2	3.4	4.4	4.4	3.9	5.6	5.7
2	3	1.9	2.4	2.4	2.7	3.3	3.3	3.2	4.4	4.5	4.1	5.7	5.8
3	1	1.8	2.3	2.3	2.5	3.1	3.1	3.3	4.2	4.2	4.1	5.4	5.4
3	2	2.0	2.1	2.1	2.6	2.9	2.9	3.2	3.9	3.9	4.5	5.0	5.1
3	3	2.0	2.2	2.2	2.7	3.0	3.0	3.2	4.1	4.1	4.1	5.3	5.3

[a] FWD load level
[b] Measured vertical stress
[c] Predicted vertical stress using backcalculated AC moduli
[d] Predicted vertical stress using laboratory-derived AC moduli

Table 38. Summary of measured and predicted vertical stresses at the top of subgrade (kPa)

Testing Location	Measurement Repetition	LL-1[a] M[b]	LL-1 P_B[c]	LL-1 P_L[d]	LL-2 M	LL-2 P_B	LL-2 P_L	LL-3 M	LL-3 P_B	LL-3 P_L	LL-4 M	LL-4 P_B	LL-4 P_L
1	1	0.8	1.0	1.1	1.1	1.4	1.5	1.4	1.9	2.1	1.8	2.4	2.7
1	2	0.8	1.0	1.1	1.0	1.4	1.5	1.4	1.9	2.1	1.7	2.5	2.7
1	3	0.9	1.0	1.1	1.1	1.4	1.5	1.4	1.9	2.1	1.7	2.5	2.7
2	1	0.9	1.0	1.1	1.1	1.4	1.5	1.5	1.9	2.1	1.9	2.5	2.7
2	2	0.8	1.1	1.2	1.2	1.5	1.6	1.4	2.0	2.2	1.5	2.6	2.8
2	3	0.8	1.1	1.2	1.0	1.5	1.6	1.3	2.0	2.2	1.6	2.6	2.8
3	1	0.8	1.0	1.1	1.1	1.4	1.5	1.4	1.9	2.1	1.9	2.5	2.7
3	2	0.8	1.0	1.1	1.1	1.4	1.5	1.4	1.8	2.0	1.9	2.4	2.5
3	3	0.9	1.0	1.1	1.1	1.4	1.5	1.4	1.9	2.0	1.8	2.4	2.6

[a] FWD load level
[b] Measured vertical stress
[c] Predicted vertical stress using backcalculated AC moduli
[d] Predicted vertical stress using laboratory-derived AC moduli

The effectiveness of developed FE models in simulating pavement response is evaluated in terms of the prediction error at each load levels was defined as given in Equation 25. The first response parameter discussed here is the surface deflection. Prediction errors of surface deflections at all FWD load levels are summarized in Table 39. A corresponding graphic illustration is given in Figure 25a. A general observation of the deflection prediction is that the prediction error drops as the FWD load level increases regardless of the source of AC moduli. Prediction errors are also much higher at further distances from the load. At 60 in (1524 mm) from the FWD load, the maximum prediction errors are -55.1 percent and 58.3 percent for backcalculated and laboratory-derived AC moduli, respectively. As indicated by the average prediction errors (-9 percent and -12 percent), both sources of AC moduli result over-predictions of surface deflections.

Prediction errors of horizontal strains and vertical stresses at all FWD load levels are summarized in Table 40. As demonstrated in Figures 25b through 25f, the FE model always over-predicts strain and stress responses directly under the FWD load in all pavement layers regardless of the FWD levels. On the other hand, the response location has a considerable impact on the magnitude of the prediction error. For all load levels, the prediction errors in the wearing HMA layer and subbase layer are constantly higher than those in other pavement layers. The possible causes for this observation are noted, as follows. In this study, the wearing and binder layers were combined as a single surface layer in the backcalculations and FE simulations. First of all, although both mixtures have the same binder PG grade (PG 64-22), different nominal maximum aggregate size (9.5 mm vs. 19.0 mm) could result in a large variation in mixture stiffness at high temperatures. Also, during the FWD testing, the temperature in the wearing layer was considerably higher than the binder layer. The use of one single modulus value backcalculated from FWD deflections may not be appropriate for a thin surface layer, as in the case of selected Blair pavement structure, if responses in that thin layer are to be predicted. One possible solution to reduce the prediction error in the subbase would be the laboratory material characterization (e.g., the resilient modulus test) such that the model constants (K_1 and K_2) can be more accurately determined.

Although the predicted responses exceed the measured responses, it would be valuable if a relationship between predictions using backcalculated and laboratory-derived AC moduli could be established. In some new pavement designs where laboratory-derived properties are not available, backcalculated AC moduli from FWD deflections could be used, or when FWD tests are not yet available for rehabilitation design, laboratory results could be employed. Linear regression analyses were conducted using the predicted responses from Tables 31 to 38; the results are summarized in Tables 39 and 40. As shown in Figure 26, strong correlations were observed for the surface deflections, horizontal strains in AC layers, and vertical stresses in the subbase and subgrade.

Table 39. Summary of deflection prediction errors (cross-FWD testing locations)

Distance from FWD load, mm (in)	Load Level 1 Prediction Error (%)		Load Level 2 Prediction Error (%)		Load Level 3 Prediction Error (%)		Load Level 4 Prediction Error (%)		Average Prediction Error (%)	
	P_B[a]	P_L[b]	P_B	P_L	P_B	P_L	P_B	P_L	P_B	P_L
0 (0)	-7.5	-2.6	-1.6	-4.0	2.9	1.5	7.5	9.9	0.3	1.2
12 (305)	-8.0	-4.2	-1.7	-4.7	2.9	0.1	6.7	3.9	0.0	-1.2
24 (610)	-6.9	-3.9	0.4	-2.3	6.0	3.3	10.8	7.4	2.6	1.1
36 (914)	-12.1	-11.6	-3.8	-9.5	2.3	-3.0	6.9	2.1	-1.7	-5.5
48 (1219)	-28.1	-29.4	-17.9	-25.4	-10.2	-17.1	-4.2	-10.6	-15.1	-20.6
60 (1524)	-55.1	-58.3	-40.9	-50.9	-31.4	-40.4	-23.5	-31.7	-37.8	-45.3
Average	-19.6	-18.3	-10.9	-16.1	-4.6	-9.3	0.7	-3.1	-8.6	-11.7

[a] Prediction error using backcalculated AC moduli
[b] Prediction error using laboratory-derived AC moduli

Table 40. Summary of strain and stress prediction errors (cross-FWD testing locations)

Response Location	Load Level 1 Prediction Error (%)		Load Level 2 Prediction Error (%)		Load Level 3 Prediction Error (%)		Load Level 4 Prediction Error (%)		Average Prediction Error (%)	
	P_B[a]	P_L[b]	P_B	P_L	P_B	P_L	P_B	P_L	P_B	P_L
Bottom of Wearing	-48.1	-61.9	-43.1	-65.4	-52.3	-65.2	-53.4	-68.3	-49.3	-65.2
Bottom of Binder	-30.1	-69.4	-19.3	-55.0	-14.9	-34.0	-16.2	-19.1	-20.1	-44.4
Bottom of BCBC	-27.2	-63.2	-19.8	-33.3	-18.9	-37.7	-29.3	-44.1	-23.8	-44.6
Top of Subbase	-23.1	-35.6	-31.0	-41.6	-36.7	-48.6	-42.9	-54.3	-33.4	-45.0
Top of Subgrade	-19.5	-20.1	-19.4	-20.2	-26.8	-27.8	-30.7	-31.7	-24.1	-24.9
Average	-29.6	-50.0	-26.5	-43.1	-29.9	-42.7	-34.5	-43.5	-32.5	-52.7

[a] Prediction error using backcalculated AC moduli
[b] Prediction error using laboratory-derived AC moduli

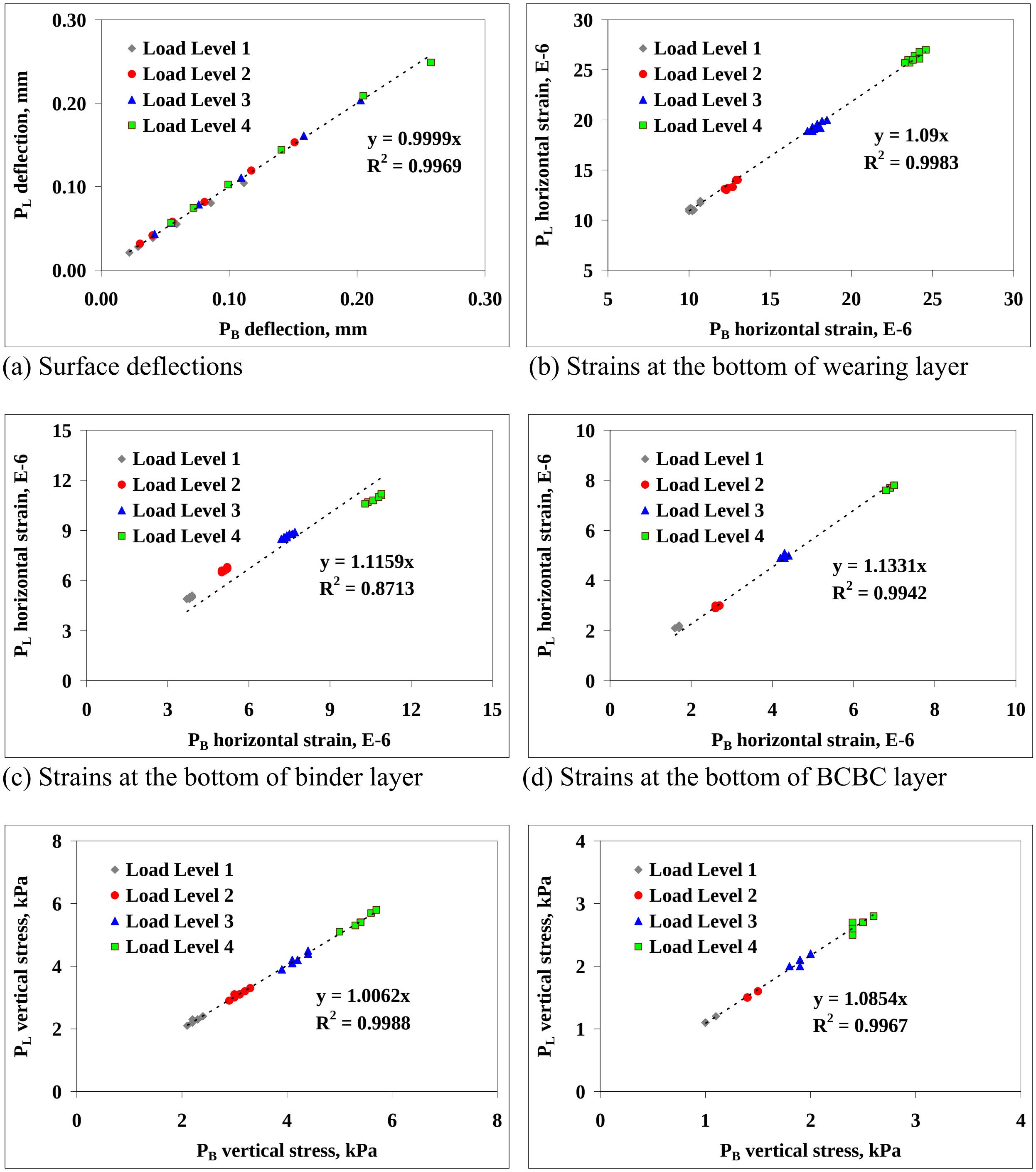

(a) Surface deflections

(b) Strains at the bottom of wearing layer

(c) Strains at the bottom of binder layer

(d) Strains at the bottom of BCBC layer

(e) Stresses at the top of subbase

(f) Stresses at the top of subgrade

Figure 25. Relationship between predicted pavement responses using backcalculated and laboratory-derived AC moduli

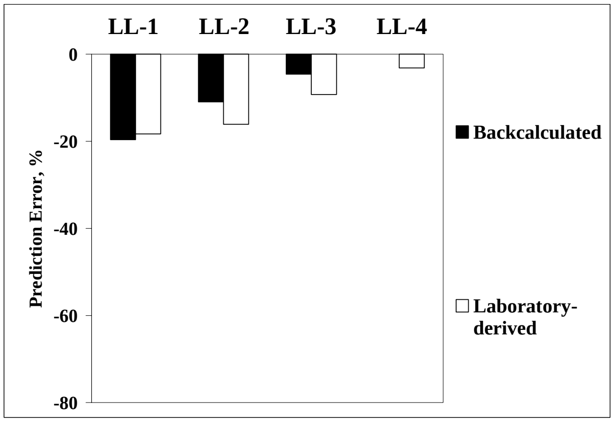

(a) Surface deflections

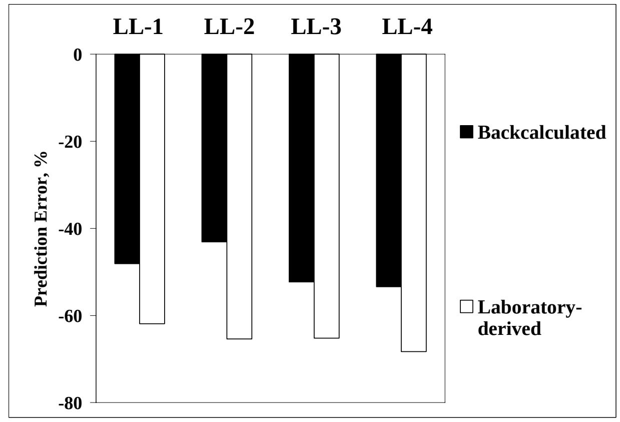

(b) Strains at the bottom of wearing layer

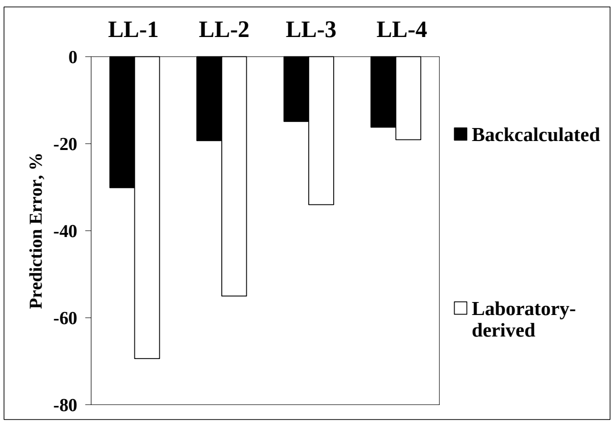

(c) Strains at the bottom of binder layer

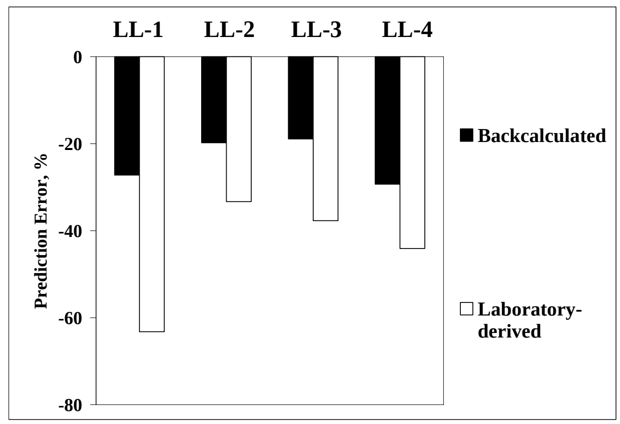

(d) Strains at the bottom of BCBC layer

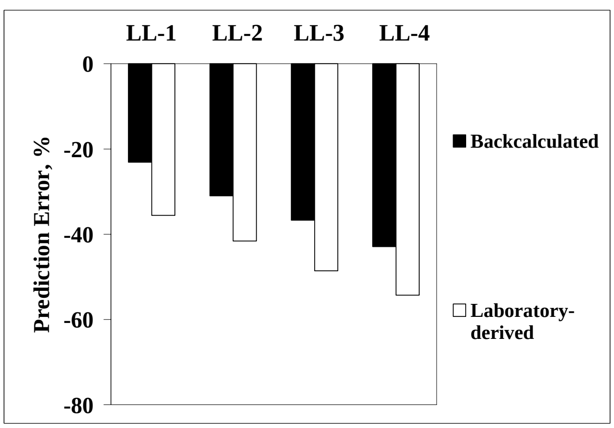

(e) Stresses at the top of subbase

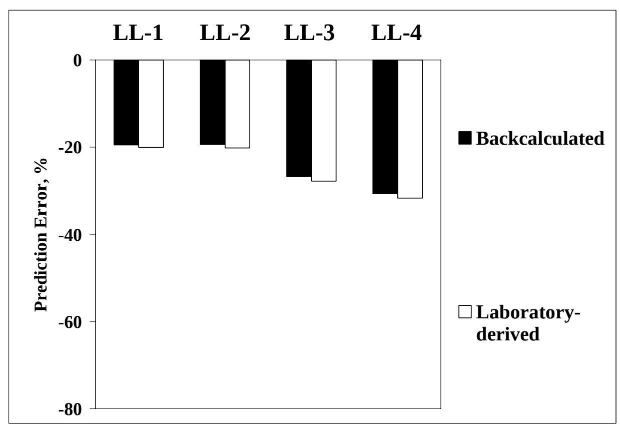

(f) Stresses at the top of subgrade

Figure 26. Comparison of measured and predicted pavement responses

Conclusions

Pavement deflection data coupled with backcalculation analysis are widely used to estimate the layer moduli of pavement structures for rehabilitation design and for pavement asset management. This paper presents a mechanistic approach to simulate full-depth flexible pavement responses when subjected to Falling Weight Deflectometer (FWD) loads. The FWD testing is conducted at pavement locations instrumented with strain gages, pressure cells, and thermocouples. For the selected full-depth asphalt concrete (AC) pavement structure, layer moduli are first backcalculated from FWD data, assuming that the AC and subbase materials are linear elastic and that the subgrade can be treated as a nonlinear elastic material. The backcalculated AC moduli are compared to laboratory values and then adjusted for load duration and temperature. The adjusted laboratory values for the surface layers are consistently lower, averaging about 70 percent of the backcalculated values. The adjusted laboratory values for the bituminous concrete base course (BCBC) are about 10 percent higher than the backcalculated values. Both backcalculated and laboratory-derived AC layer moduli are then employed to predict horizontal strains in bound materials, vertical stresses in unbound materials, and deflections at the surface of pavement through three-dimensional (3-D) finite element (FE) simulations. Finally, a comparison of simulated responses and measured pavement responses from embedded instrumentation devices during the FWD loading is made. For surface deflections, average prediction errors were 9 percent and 12 percent for predictions using backcalculated and laboratory-derived AC moduli, respectively. For the strain and stress responses, the average prediction error increased to 30 percent and 50 percent accordingly, with the predicted responses constantly exceeding the measured responses. Linear regression analyses were also performed to establish the relationship between predicted responses using different sources of AC moduli. A strong correlation was observed for every case. Findings from this study would be useful for pavement engineering applications when laboratory-derived properties are not yet available.

CHAPTER 7: PREDICTING STRAIN RESPONSE OF FLEXIBLE PAVEMENT USING INSTRUMENTATION AND SIMULATION DATA

A major application of instrumentation data is for validating existing or novel design and analysis approaches. This is accomplished by verifying field-measured parameters with theoretically calculated parameters from pavement response models. This type of work is well documented in the literature. As previously discussed, it is possible to perform theoretically rigorous 3-D FEA, incorporating a rich set of sophisticated modeling features, to estimate strains and stresses within a pavement structure. However, computational practicality (e.g., the ability to perform the calculations in an acceptable amount of time) nonetheless remains a major reason not to use 3-D FEA (MEPDG 2004). The damage accumulation scheme incorporated in the Mechanistic Empirical Pavement Design Guide (MEPDG) would require thousands of FE simulations for a single case of performance prediction. Thus, it is desirable to develop a procedure that can accurately and rapidly predict strain response with known traffic and environment information, particularly axle load and configuration, vehicle speed, and pavement temperature.

Simulation of Pavement Response

The effectiveness of any mechanistic-based pavement design depends on the accuracy of employed mechanistic parameters, such as stress and strain. The general purpose finite element software ABAQUS (version 6.6) was used in this study to simulate strain responses in the field. Key features of the developed FE model, such as model dimensions, boundary conditions, material properties, and element type, were presented in earlier sections of this report.

Prediction of Pavement Response

In previous sections, a comprehensive validation study on the developed FE model suggested good agreement between measured and FE-simulated tensile strains for the two load configurations, front and back. Verification analysis on the linearity of strain response also suggested that as the axle load (contact pressure over a rectangular contact area) increases, the strain response increases proportionally. These two conclusions reveal that at the same vehicle speed and pavement temperature, pavement response under one load configuration can be estimated from another; therefore, only response data under one load configuration are needed for strain predictions.

The following sections present an analytical procedure developed to predict pavement response using a mix of measured and FE-simulated response data. A total of nine sets of field response data were used to establish a response database such that the compiled response data are representative of a wide range of vehicle speeds and pavement temperatures.

Exploratory Data Analysis

Exploratory data analysis is an approach to data analysis that postpones the usual assumptions about what kind of model the data follow with the more direct approach of allowing the data itself to reveal its underlying structure and model. Response data in the analysis database were first divided into different groups corresponding to all combinations of analysis locations and pavement temperatures. One set of response data at the bottom of wearing layer is plotted in

Figure 27. These graphs show that for a certain load configuration and analysis location, strain response in AC layers is highly dependent upon the vehicle speed and pavement temperature. EDA suggests a nonlinear function to describe the dependency of the strain response on the vehicle speed and pavement temperature.

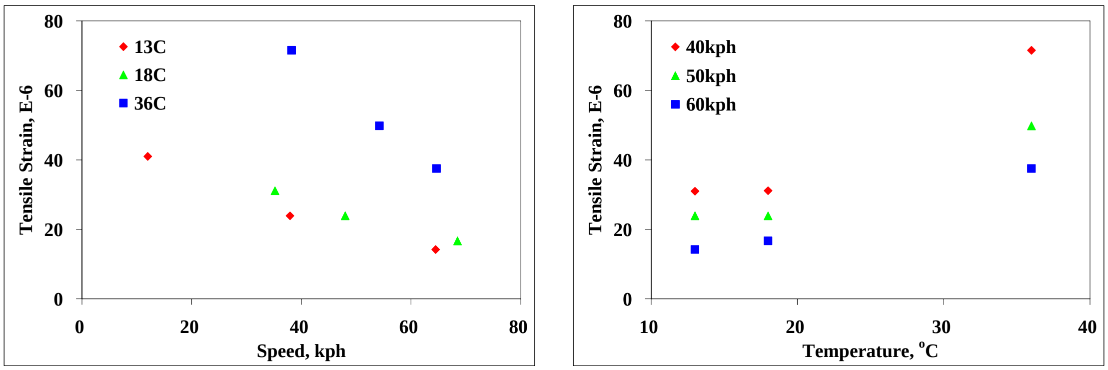

(a) Speed effect (b) Temperature effect

Figure 27. Speed and temperature dependence of tensile strains

Nonlinear Regression Analysis

Speed Effect on Strain Response

Based on the conclusion from exploratory data analysis, a nonlinear regression model was used to model the relationship between the strain response and vehicle speed:

$$\varepsilon = a * EXP(b * S) + e \tag{26}$$

where ε is tensile strain, S is vehicle speed, a and b are nonlinear model coefficients, and e is random normal error with mean 0 and variance σ^2. Estimates of Eq. (26) are summarized in Table 41. Opposite signs of model coefficient a and b suggest that the strain response decreases with the increase in speed. This is because when speed increases, there is a decrease in the time of contact between the tire and the pavement surface. Excellent R^2 values indicate the appropriateness of the selected model form. Before proceeding with further prediction on strain response, for each combination of analysis location and pavement temperature, strain responses were extrapolated to a wide range of vehicle speeds at a 5-kph interval. This range covers the vehicle operational speeds at the Blair site. One such example is graphically shown in Figure 28.

Table 41. Nonlinear tensile strain - speed model coefficients

Analysis Location	Temperature, ^{o}C	Model Coefficient		R^2
		a	*B*	
Bottom of Wearing	13	51.97	-0.0202	1.000
	36	182.70	-0.0243	0.997
	18*	59.42	-0.0186	0.998
Bottom of Binder	15	21.96	-0.0121	0.952
	33	80.96	-0.0216	0.971
	13*	20.98	-0.0207	0.999
Bottom of BCBC	12	20.17	-0.0059	0.997
	29	30.92	-0.0114	0.959
	5*	12.33	-0.0119	0.994

*NOTE: from FE simulations

Temperature Effect on Strain Response

To account for the effect of pavement temperature on strain response, strain response at a field temperature was shifted to the reference temperature:

$$\varepsilon_T = \varepsilon_0 * SF \tag{27}$$

where ε_0 is the tensile strain at the reference temperature, and ε_T is the tensile strain at a field temperature. For a particular vehicle speed (e.g., 70 kph), the duration of mechanical loading was assumed to be constant throughout pavement depths. The lowest temperature was arbitrarily chosen as the reference temperature for each combination in the analysis database. For the sake of brevity, one set of shift factors is given in Table 42 and plotted in Figure 28. It can be seen that *SF* is always larger than unity because the strain response increases as the temperature increases.

Table 42. Shift factors of tensile strain at the bottom of wearing layer of the Blair site

Pavement Temperature, °C	Vehicle Speed, kph	Tensile Strain, E-6	Tensile Strain *SF*
13	60	15.5	1.0
18	60	19.5	1.3
36	60	42.5	2.7
13	70	12.6	1.0
18	70	16.2	1.3
36	70	33.3	2.6
13	80	10.3	1.0
18	80	13.4	1.3
36	80	26.1	2.5
13	90	8.4	1.0
18	90	11.1	1.3
36	90	20.5	2.4
13	100	6.9	1.0
18	100	9.2	1.3
36	100	16.1	2.3

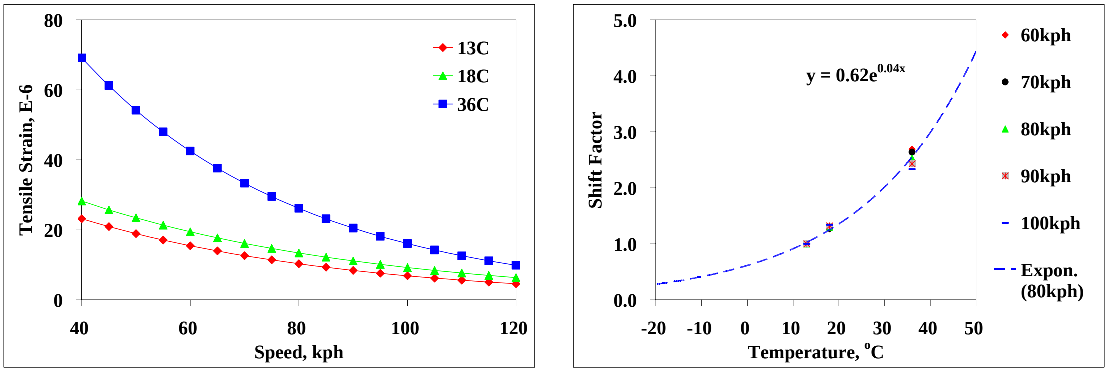

(a) Strain extrapolation (b) Temperature vs. shift factor

Figure 28. Strain prediction (bottom of wearing layer)

Finally, a nonlinear regression model was used to model the relationship between the shift factor and pavement temperature for each vehicle speed:

$$SF = c * EXP(d * T) + e \tag{28}$$

where T is pavement temperature, c and d are nonlinear model coefficients, and e is random normal error with mean 0 and variance σ^2. An average R^2 value of 0.95 was observed for all combinations in the analysis database (Figure 28).

Evaluation of Response Prediction

Figure 29 presents a comparison of predicted tensile strains to the measured values for the bottom of wearing, binder, and BCBC layers, respectively. Overall, the developed analytical procedure predicts tensile strains reasonably well. It is also noticeable that the analytical procedure tends to under-predict strain response. There is a fair amount of deviation between predictions and measurements at high strain magnitudes, especially for the upper layers (Figures 29a and 29b).

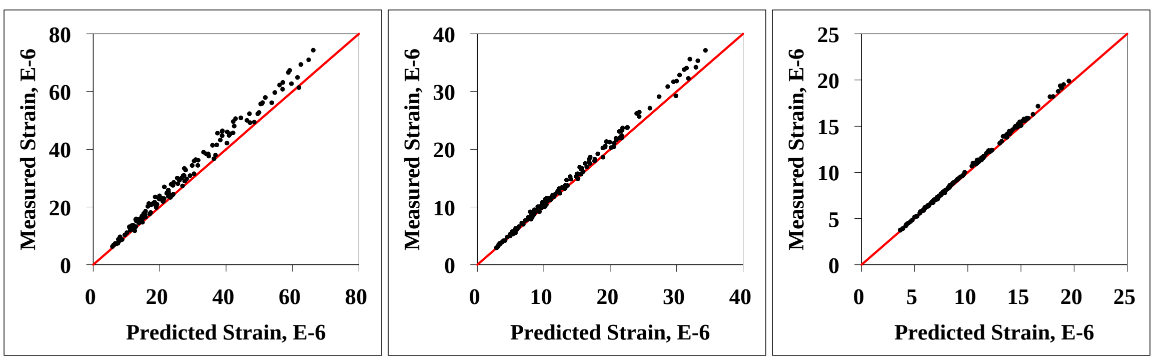

(a) Bottom of wearing layer (b) Bottom of binder layer (c) Bottom of BCBC layer

Figure 29. Predicted vs. measured strain responses

To further investigate this phenomenon, response differences (predictions-measurements) were plotted for individual axles at various vehicle speeds and pavement temperatures. As illustrated in Figures 30 through 32, a better concurrence at lower strain magnitudes implies that the effects of extremely low vehicle speeds, high pavement temperatures, and heavy axle loads on the strain response are not accounted for precisely. These conditions result in a difference between predicted and measured strains of approximately 9 microstrain, suggesting a still reasonable prediction. At high strain magnitudes, it can be seen that under-prediction of tensile strains occurs at the bottom of the AC layers. One possible source of this response difference is from the inability of the developed FE model to properly capture the viscoplastic behavior of AC at high temperatures and slow loading rates.

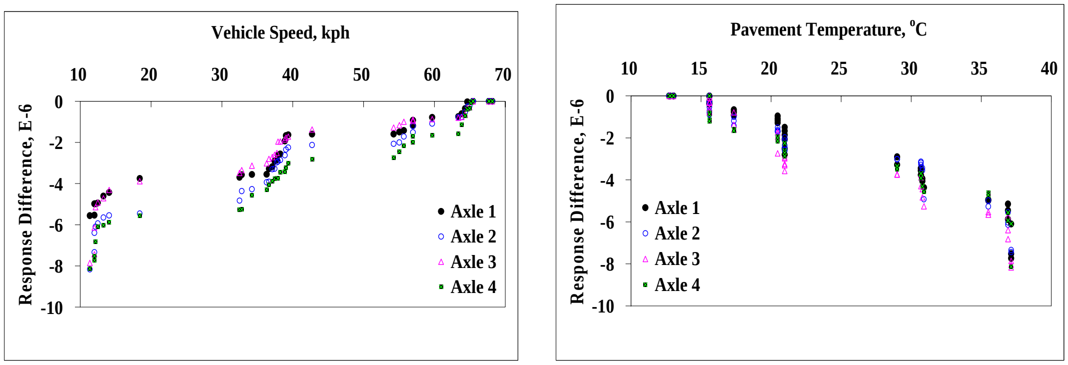

(a) Speed effect (b) Temperature effect

Figure 30. Speed and temperature dependency of response differences, bottom of wearing layer

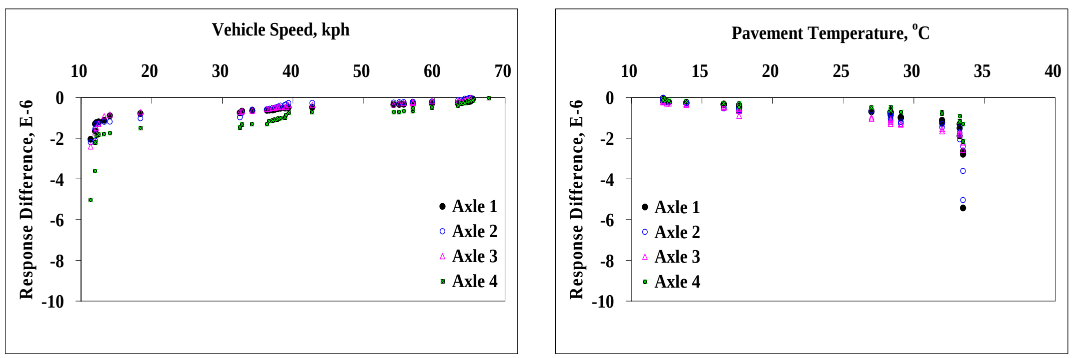

(a) Speed effect (b) Temperature effect

Figure 31. Speed and temperature dependency of response differences, bottom of binder layer

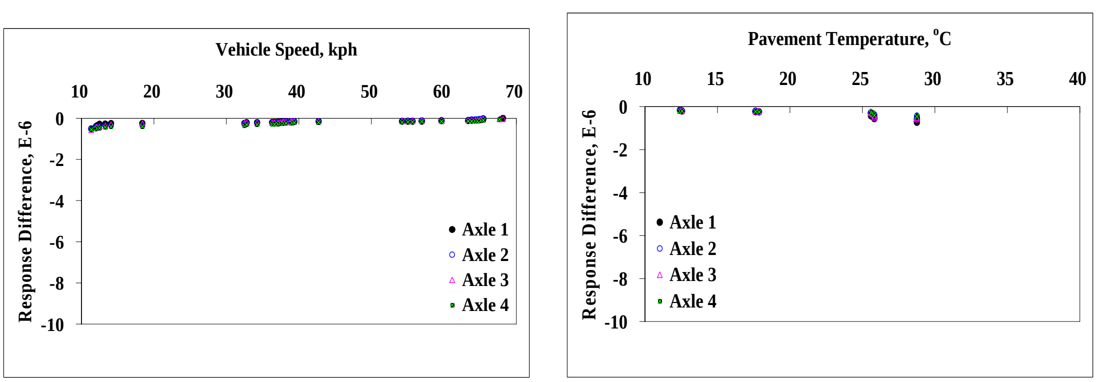

(a) Speed effect (b) Temperature effect

Figure 32 Speed and temperature dependency of response differences, bottom of BCBC layer

Response Superposition

The previous nonlinear regression analyses were only made for the single axle configuration (axle 4) of the SISSI truck. In the field, however, the traffic conditions are much more complicated, including different axle spacings and loads.

In the development of 3-D FE models, the effect of a moving load on a point in the pavement was simulated by noting that a time function of the stress can be used to approximate the stress experienced by the point (Huang 1993). With the same sine function, the load amplitude of a single axle load can be estimated from the load duration calculated from the axle spacing and vehicle speed.

For a single axle load, tensile strains were directly predicted using the nonlinear strain response models and the linearity of strain response. For multiple axle loads, each axle load is multiplied by the load amplitude so that the axle load can be transformed to an “equivalent” axle load under an axle of interest. In a prior study (Yin 2007), it was found that the tire load has almost no influence on the strain response at distances more than 2 m from the center of loading area; therefore, it is reasonable to only consider axle spacings smaller than 2 m. Finally, the total strain response is calculated using superposition to account for multiple axles.

Demonstration Example

Previous sections have presented details of the developed analytical procedure for the strain response prediction. In this section, an example is provided to demonstrate this procedure. The instrumentation data collected at 07:05:00 a.m. on 07/23/2004 are summarized in Table 43. The following steps were used to calculate the total tensile strain at the bottom of the wearing layer for each axle:

- Step 1. Calculate the shift factor from the field vehicle speed and pavement temperature. From Table 7 and Eq. (28), *SF* is 1.4.
- Step 2. Calculate strain responses at the field vehicle speed (i.e., 76 kph) and reference temperature. With Eq. (26), the tensile strain is 10.3 microstrain.
- Step 3. Predict strain response under a single axle load (axle 4 of the SISSI truck) using results from Step 1 and Step 2. With Eq. (26), the tensile strain is 14.4 microstrain.
- Step 4. Calculate strain responses with the actual axle load for each axle based on the linearity of response. Results are shown in Table 44. These strain values take into consideration both speed and temperature effects on the strain response.
- Step 5. Because the axle spacings for axles 1-2 and 3-4 are larger than the minimum requirement of 2 m, the response superposition is only needed for axles 2 and 4. Based on the vehicle speed and axle spacing, it requires 0.062 sec for axle 3 to reach the location of axle 2 and 0.058 sec for axle 5 to reach the location of axle 4. Consequently, the load amplitudes are 0.077 and 0.162 for axles 3 and 5, respectively. Hence, the equivalent axle load of axles 3 and 5 are 233 kg and 434 kg, respectively.
- Step 6. Calculate strain responses due to multiple axles for axle 2 and 4.
- Step 7. Calculate the total tensile strain using response superposition (Table 44).

Table 43. Example of instrumentation data

<table>
<tr><td rowspan="11">Traffic Information</td><td>Vehicle Class</td><td colspan="2">9</td></tr>
<tr><td>Vehicle Speed, kph</td><td colspan="2">76</td></tr>
<tr><td rowspan="5">Axle Load, kg</td><td>Axle 1</td><td>5896.7</td></tr>
<tr><td>Axle 2</td><td>3356.6</td></tr>
<tr><td>Axle 3</td><td>3039.1</td></tr>
<tr><td>Axle 4</td><td>2857.6</td></tr>
<tr><td>Axle 5</td><td>2676.2</td></tr>
<tr><td rowspan="4">Axle Spacing, m</td><td>Axle 1-2</td><td>5.3</td></tr>
<tr><td>Axle 2-3</td><td>1.3</td></tr>
<tr><td>Axle 3-4</td><td>10.6</td></tr>
<tr><td>Axle 4-5</td><td>1.2</td></tr>
<tr><td>Pavement Temperature, ^{o}C</td><td>Mid-depth of wearing layer</td><td colspan="2">21.0</td></tr>
</table>

Table 44. Summary of calculated tensile strains

Axle	Strain Response Due to a Single Axle, E-6	Need Response Superposition?	Strain Response Due to Multiple Axles, E-6	Total Strain Response, E-6
1	10.4	NO	-	10.4
2	5.9	YES	0.4	6.3
3	5.3	NO	-	5.3
4	5.0	YES	0.8	5.8
5	4.7	NO	-	4.7

Concluding Comments

Utilizing sound, reliable computational techniques to determine pavement response under diverse loading and environment conditions could be very useful in designing pavement structures or predicting long-term performance. The objective of this study is to develop an analytical procedure with which tensile strains in AC layers can be accurately and quickly predicted for future research on fatigue cracking prediction.

First, a 3-D FE model was developed to simulate pavement response under various load configurations, traffic speeds, and environmental conditions. Analysis results from a validation study suggest that the developed FE model provides acceptable predictions of tensile responses at multiple depths within AC layers as compared to field measurements. Although many unbound materials are not linear but stress dependent, the assumption of linearity of strain response still provides acceptable levels of accuracy for the range of stress levels produced by typical truck loads on typical full depth flexible pavement structures.

Despite its high capabilities, the 3-D FEA is not regarded as a practical tool for accumulated damage analysis and performance prediction because of high computational cost and time. Consequently, an analytical procedure was developed using measured and simulated response data to predict the strain response. General trends in the mixed response data were first identified through exploratory data analysis. Nonlinear regression models were then utilized to describe the dependency of strain response on the vehicle speed and pavement temperature. For a single axle load, the strain response at field conditions was calculated from the strain response at the reference temperature using the shift factor. Following the linearity of response, for various axle loads, tensile strains at multiple depths of AC layers were computed.

The effectiveness of the developed analytical procedure was evaluated using field measurements. Although predicted strains are always smaller than measured values, the maximum response difference of 9 microstrain implies a reasonable accuracy of the analytical procedure. A demonstration example of predicting tensile strains under multiple axle loading conditions is also provided to facilitate application of the procedure to other data sets. The developed procedure for strain prediction has substantial potential benefit for pavement fatigue cracking predictions because such predictions usually require an incremental damage analysis.

CHAPTER 8: THE IMPACT OF STRAIN GAGE INSTRUMENTATION ON LOCALIZED STRAIN RESPONSES IN ASPHALT CONCRETE PAVEMENTS

In the previous sections, a 3-D viscoelastic based finite element (FE) model was developed to capture flexible pavement response to vehicular loading. Partial validation analyses indicated a prediction error varying from 20 to 30 percent from FE simulations as compared to response data collected from strain gages installed in asphalt concrete (AC) layers. A vital assumption in the previous FE model was that AC layers were homogenous continuum media. The work presented here extends the previous work through assessing the impact of strain gage instrumentation on localized strain responses in AC layers. The materials characterizations used for this study were those from the three asphalt concrete layers at the Blair site. The other pavement structure parameters were also taken from Blair.

Strain Gages in AC Pavements

Fundamentally, all strain gages are designed to convert mechanical motion into an electronic signal. A change in capacitance, inductance, or resistance is proportional to the strain experienced by the sensor. If a wire is held under tension, it gets slightly longer and its cross-sectional area is reduced. This changes its resistance *(R)* in proportion to the strain sensitivity *(S)* of the wire's resistance. When a strain is introduced, the strain sensitivity, which is also called the gage factor *(GF)*, is given by:

$$GF = \Delta R / S \tag{29}$$

If the gage factor were due entirely to dimensional change, Poisson's ratio would suggest that the gage factor for any wire would be approximately 1.7 (Omega 1996). However, different types of strain gages with different gage factors are commercially available, each having been developed in response to a demand for a gage to meet or withstand specific conditions.

The Dynatest PAST II strain gages used in the SISSI project are characteristic of typical H-type AC strain gages. These were chosen for dynamic strain measurements because of their success in earlier flexible pavement instrumentation projects ((Baker 1994, Loulizi et al. 2001, Sargand et al. 1997, and Timm et al. 2004). The gages are 102 mm in length with 75-mm-wide arms, as illustrated in Figure 33. The gages are a quarter bridge with a resistance of 120 ohms and have a gage factor of 2.0. They have a physical range of up to 1500 microstrains and a thermal range from -30°C to 150°C. An elastic modulus of 2.2GPa was assumed for the gage. The stainless steel arms (for stainless steel, typical elastic modulus is about 29GPa) are fastened at each end of the mid-section and serve as anchors to the pavement. The gage produces a strain measurement when the mid-section is compressed or elongated. Therefore, when the AC is subjected to a force, the mid-section follows any deformation in the material and gives a measurement of strain.

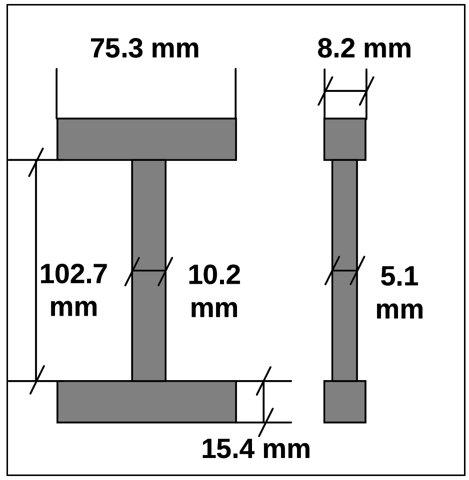

Figure 33. Dimensions of modeled AC strain gage, characteristic of the Dynatest PAST II

Finite Element Model

The finite element model previously described and validated was used for this investigation. However, an additional factor was that one of the main challenges related to the finite element modeling is the quality (the degree) of adhesion between two very different components, soft material (AC) and hard material (strain gage assembly). If two materials do not adhere well to each other, the predicted pavement response at the center of the mid-section of the strain gage can be seriously affected (Figure 34a). Although the 8-node hexahedral element is the most common element used in 3-D FE modeling, a complex solid model/interface, as the case in this study, can be broken down into tetrahedral elements more easily when compared to hexahedral elements. To improve the rate of convergence and the compatibility at the AC material – strain gage (SG) interface, 10-node quadratic tetrahedron elements were used (Figure 34b). Considering the temperature dependency of AC materials, coupled temperature-displacement features that have both displacement and temperature degrees of freedom were also added into the elements.

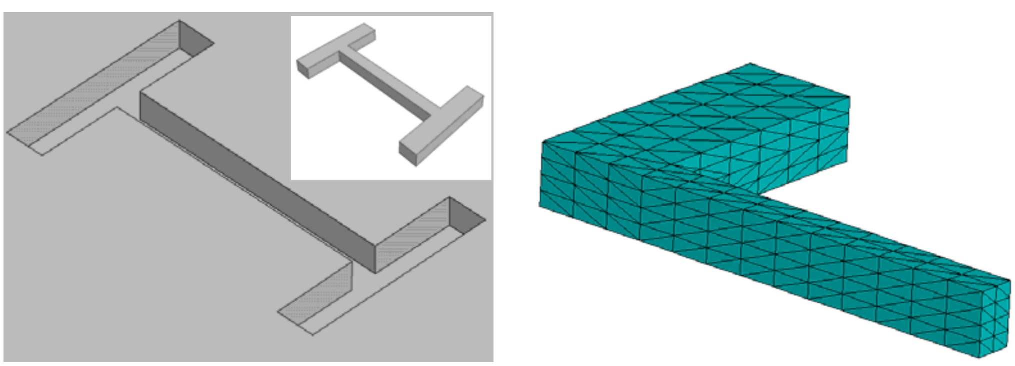

(a) Bonding AC and SG (b) A quarter strain gage

Figure 34. Modeling AC-SG interface

Resulting Typical Pavement Dynamic Responses

Compared to the FE model without strain gage, inclusion of a strain gage always results in predicting smaller strain responses. The time retardation of the viscoelastic behavior of AC materials is not present in Figure 35. The longitudinal and transverse strains reach their peak values at the same time. Finally, the longitudinal strain does not show the compression-tension-compression pattern, and the transverse strain does not preserve unrecovered strain at the end of loading time. All of these dissimilarities may result from the elastic behavior of the strain gage.

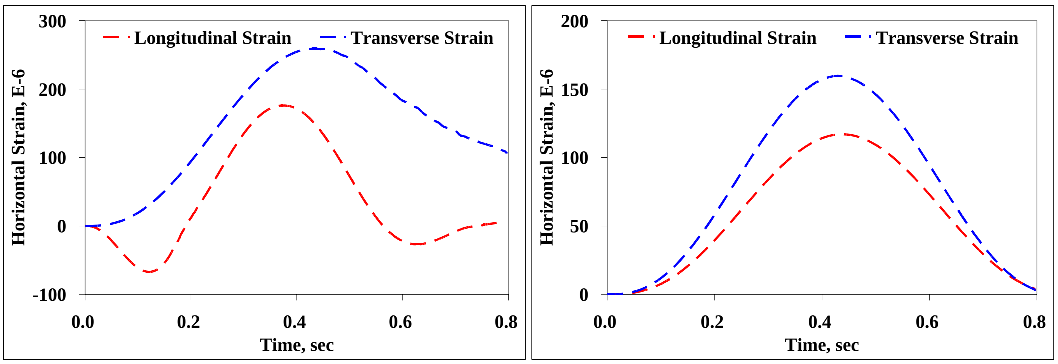

(a) without strain gage (b) with strain gage

Figure 35. Typical pavement responses at 50mm depth (mix 2, pavement temperature=40°C, vehicle speed = 8 kph, contact pressure = 800 kPa)

Summary

A key assumption in the FEA presented in previous sections was that AC layers were homogenous continuum media. In this section, the FE model was revised to evaluate the impact of embedded strain gages on localized strain responses in the AC layers. With a three-layer conventional flexible pavement structure, strain gages were modeled in both longitudinal and transverse directions at multiple depths in AC layers. Elastic material properties were assumed for these gages. It was also assumed that AC materials and strain gages were fully bonded. Extensive FE simulations under different loading and environmental conditions revealed that including an elastic strain gage in viscoelastic AC materials results in appreciably lower strain responses. This is manifested at high pavement temperature, low vehicle speed, and high contact pressure. The presence of a strain gage may result in a prediction error up to -84 percent.

CHAPTER 9: THE EFFECT OF LOADING TIME ON FLEXIBLE PAVEMENT DYNAMIC RESPONSE: A FINITE ELEMENT ANALYSIS

Accurate prediction of flexible pavement response requires the pavement temperature and the loading time. To predict pavement response, the MEPDG utilizes both pavement temperature and loading time in layered elastic analyses. Although the MEPDG approach is very comprehensive, it may not be as efficient as the approach presented herein to evaluate the loading time itself, if needed. The objective of this study was to develop a single factor which represents both temperature and time dependency of AC materials. This single factor is referred to as "effective temperature." With only one factor (effective temperature) instead of two (temperature and time), more advanced theoretical analysis tools, such as the finite element method, can be readily utilized. The stand-alone impact on the pavement response from the loading time can be also assessed.

Duration of Loading Time

The simplest way to characterize the behavior of a flexible pavement under moving loads is to consider it as a homogeneous half-space. A half-space is the space bound by an infinite plane on which the loads are applied. The original Boussinesq theory was based on a concentrated (point) load applied on an elastic half-space. Later work by Ahlvin and Ulery (1962) presented a series of equations and tables so that response parameters at any given location could be computed. In this work, following Ahlvin and Ulery's method, vertical stresses due to a circular moving load at various vehicle speeds (16, 32, 64, and 96 kph) were first computed at different times and spatial locations. Again, this circular load was assumed to have a radius '*a*' of 150 mm and a uniform contact pressure *q* of 0.5 MPa. Further, the calculated vertical stresses were normalized to obtain the load amplitude at different times. An example is given in Figure 36.

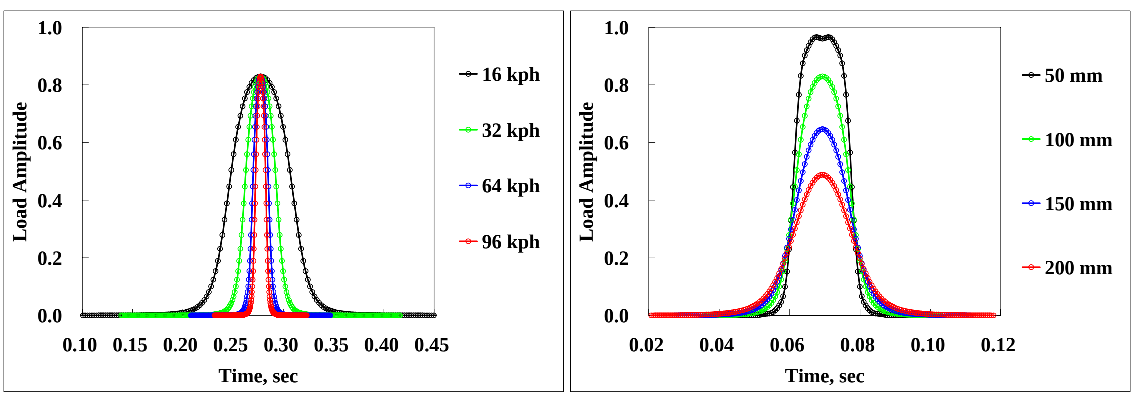

(a) 100 mm depth (b) 64 kph

Figure 36. Dependency of the duration of moving load on vehicle speed and depth

It was noted that the load amplitude fluctuates around zero at locations away from the center of the loading area (Figure 37a). Because stress pulses last for only a short period of time, a small variation of load magnitude may have a significant impact on induced stresses when the load magnitude is very close to zero. Such sensitivity of stresses to load magnitude variation will affect the perceived duration of the moving load. In this study, the duration of moving load was defined as the time between two critical points on the load amplitude curve. The first point is taken as the last point with zero load magnitude when the load approaches and the second as the first point with zero magnitude when the load leaves, as demonstrated in Figure 37b. Calculated durations of moving load are summarized in Table 45. A graphic representation is given in Figure 38a. The change in moving load duration is more pronounced at lower vehicle speeds. Figure 37a also suggests that the duration of moving load is significantly higher at pavement locations deeper than 50 mm.

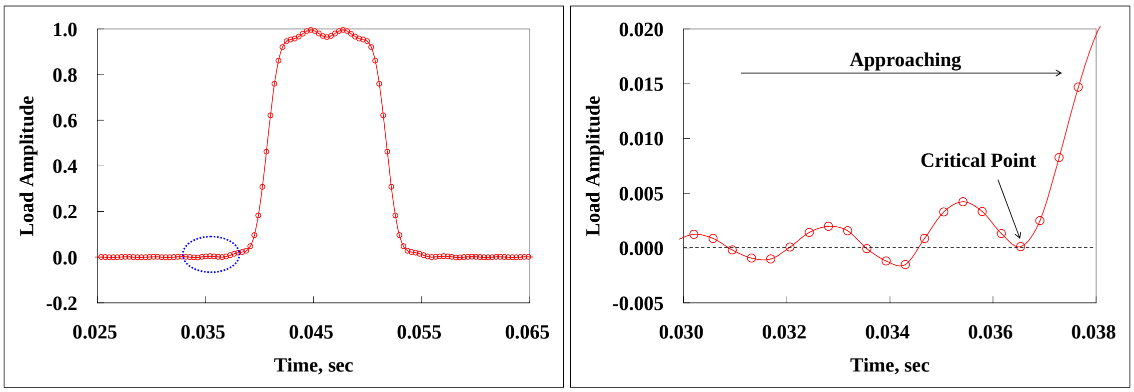

(a) Load amplitude on approach (b) Critical point at last zero amplitude

Figure 37. Determination of the duration of moving load

To simplify the process of simulating a moving load in FEA, a haversine function proposed by Huang (1993) was adopted to describe the relationship between the duration of moving load and the load amplitude at the pavement surface:

$$L(t) = q * \sin^2\left(\frac{\pi}{2} + \frac{\pi t}{d}\right) \tag{30}$$

where t is the time of interest, q is the load amplitude, and d is the duration of moving load, which is referred to as the time between two zero load amplitudes. The durations of moving load versus the load amplitude for different vehicle speeds are plotted in Figure 38b.

Table 45. Duration of moving load at different vehicle speeds and depths

Depth, mm	Duration of Moving Load, sec				
	8 kph	16 kph	32 kph	64 kph	96 kph
0	0.143	0.072	0.036	0.018	0.012
5	0.152	0.076	0.038	0.019	0.013
15	0.152	0.076	0.038	0.019	0.013
25	0.215	0.107	0.058	0.027	0.018
35	0.235	0.116	0.058	0.029	0.019
45	0.349	0.175	0.087	0.044	0.029
55	0.405	0.201	0.108	0.051	0.034
65	0.421	0.210	0.105	0.053	0.035
75	0.465	0.235	0.116	0.058	0.039
85	0.492	0.246	0.123	0.062	0.041
95	0.528	0.264	0.132	0.066	0.044
105	0.555	0.277	0.139	0.069	0.046
115	0.582	0.291	0.145	0.073	0.049
125	0.608	0.304	0.152	0.077	0.051
135	0.626	0.313	0.157	0.079	0.052
145	0.653	0.327	0.163	0.082	0.054
155	0.680	0.340	0.170	0.085	0.057
165	0.698	0.349	0.175	0.087	0.058
175	0.725	0.362	0.181	0.091	0.060
185	0.745	0.371	0.186	0.093	0.062
195	0.770	0.385	0.192	0.096	0.064

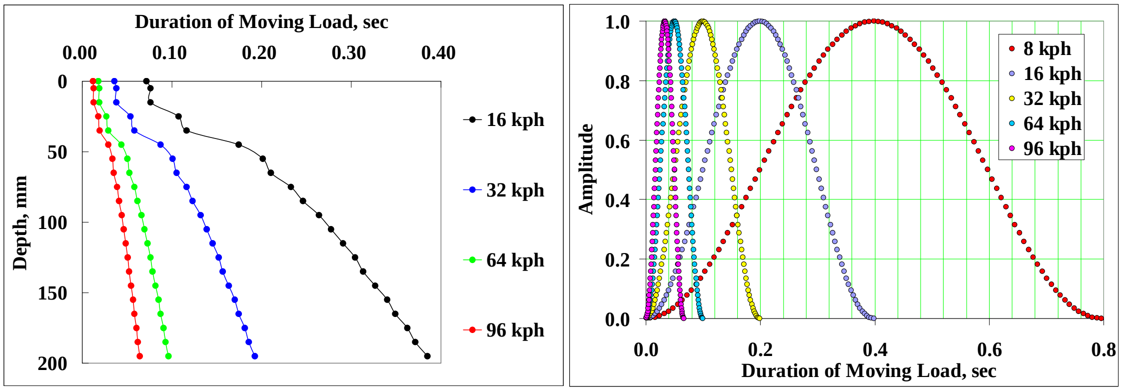

(a) At different pavement depths (b) At pavement surface

Figure 38. Duration of moving load

Effective Temperature

Under a traffic load, the slope of the stress distribution in a pavement structure is a function of the stiffness of the layers. It is well accepted that the time-temperature superposition principle is valid in both frequency and time domains. The MEPDG uses the "effective length" and "effective depth" to determine the slope value and subsequent loading time at a given AC layer depth. This method is based upon an assumption that the stresses and strains below a layer depend on the stiffness of that layer only. If the thickness and Poisson's ratio of a layer are changed but the stiffness remains unchanged, the stresses and strains below the layer remain unchanged. In this study, a new analytical procedure was developed to account for the effect on pavement response of varying loading time across the depth. The developed method is based on the fact that in viscoelastic materials, the effect of time of mechanical loading can be transferred to the effect of temperature loading and vice versa. Consequently, the viscoelastic behavior of AC materials is incorporated systematically in the response analysis. The transfer factor, T, in time domain, at the depth of interest was first calculated from the duration of moving load:

$$T = \frac{t_0}{t_D} \tag{31}$$

where t_D is the duration of load application at the depth of interest and t_0 is the duration of load application at the pavement surface. Transfer factor T is always smaller than unity because the duration of moving load increases as the depth increases. Different vehicle speeds result in different loading times at the pavement surface and at different depths; however, the transfer factor T remains the same.

Because the dynamic modulus ($|E^*|$) obtained from the complex modulus test is required for response predictions, a *material dependent* parameter, pseudo temperature (T_S), was defined to transfer the loading time in the time domain to the frequency domain. At a depth of interest, T_S was determined from the polynomial fit of the log shift factor vs. temperature curve. Such a fit for two AC mixtures is shown in Figure 39. The effective temperature (T_E) at the depth of interest was calculated as the following:

$$T_E = T_M + (T_S - T_R) \tag{32}$$

where T_M is the measured pavement temperature at a specific depth, and T_R is the reference temperature used in the construction of the dynamic modulus master curve.

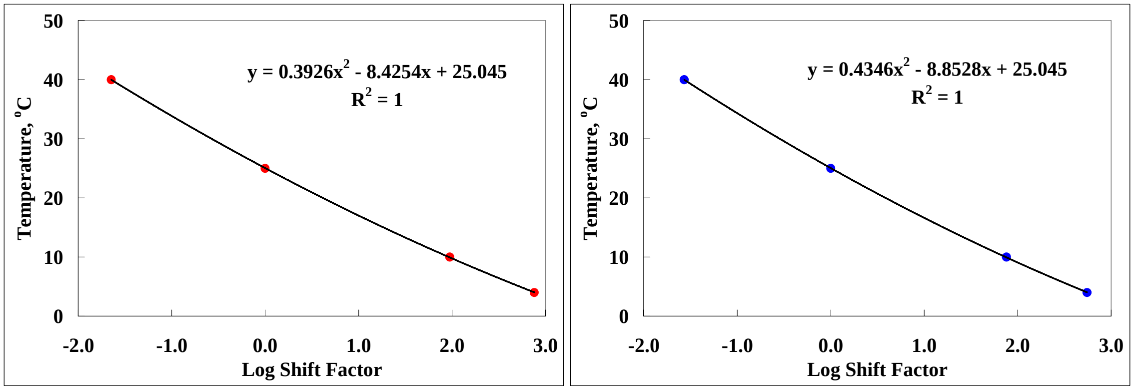

(a) Mixture 1 (b) Mixture 2

Figure 39. Polynomial fit of the log shift factor vs. temperature

In this study, 25°C was selected as T_R. In Equation 32, the effective temperature contains three components, T_M, T_S, and T_R. Measured pavement temperature was extrapolated from a second order polynomial fit of measured pavement temperature vs. depth curve (Figure 40). Since the focus of this study was the impact of loading time on the viscoelastic behavior of AC materials, only the pavement temperatures in AC layers were considered. It was assumed that the AC materials of the wearing, binder, and BCBC layers had similar thermal conductivity. Consequently, the relationship between AC layer temperature and depth (Figure 40) can be rationally applied to a pavement structure with only one single AC layer. For demonstration purposes, only the hottest (12:59 p.m.) and coldest (10:30 a.m.) temperatures during the day were selected and used for calculating the effective temperature. The positive term, T_S - T_R, exclusively reflects the effect of loading time in terms of temperature. In other words, the increase in the duration of moving load has been transformed to the increase in pavement temperature.

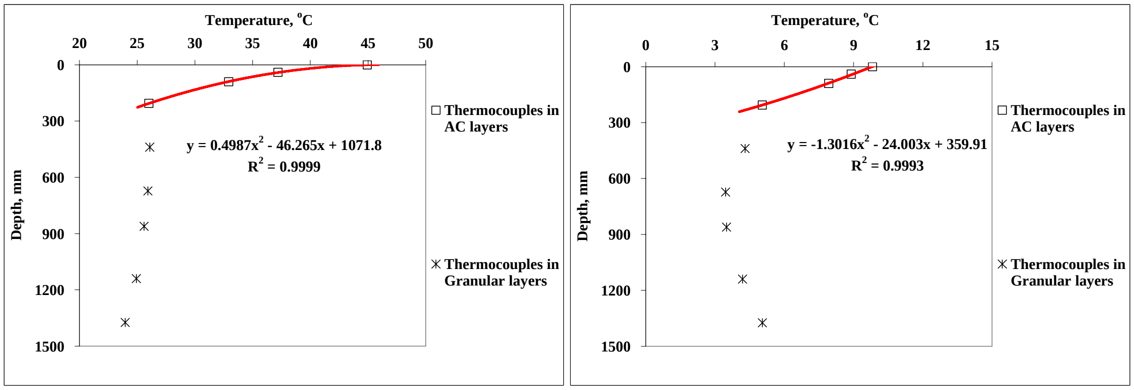

a) Summer (b) Spring

Figure 40. Polynomial fit of measured temperatures in AC layers

A summary of T_M, T_S, and T_E values are given in Table 46. A comparison of T_M and T_E is shown in Figures 47a and 47b for the summer and spring, respectively. The two mixtures described earlier produced similar values for effective temperature. As the pavement temperature profile in the summer has a larger variation, the effective temperature is also more variable than for the spring. The discrepancy between measured and effective temperatures becomes substantial as the depth increases, especially for the summer. The largest discrepancy, 6.5°C between T_M and T_E, exists at the bottom of the AC layer for both seasons. This feature is observed for both mixtures.

Table 46. Summary of measured (T_M), pseudo (T_S), and effective (T_E) temperature, °C

Depth, mm	Log Transfer Factor	T_S		Summer			Spring		
		Mix 1	Mix 2	T_M	T_E, Mix 1	T_E, Mix 2	T_M	T_E, Mix 1	T_E, Mix 2
5	-0.026	25.3	25.3	43.6	43.9	43.9	9.7	10.0	10.0
15	-0.026	25.9	25.9	42.0	42.2	42.3	9.5	10.4	10.4
25	-0.176	26.5	26.6	40.4	42.0	42.0	9.3	10.8	10.9
35	-0.211	26.8	26.9	38.9	40.8	40.9	9.1	11.0	11.1
45	-0.387	28.4	28.5	37.6	40.5	40.6	8.9	12.3	12.5
55	-0.449	28.9	29.1	36.2	40.1	40.3	8.8	12.7	12.9
65	-0.468	29.1	29.3	35.0	39.1	39.3	8.6	12.7	12.9
75	-0.512	29.5	29.7	33.8	38.3	38.5	8.4	12.9	13.1
85	-0.536	29.7	29.9	32.8	37.4	37.7	8.2	12.9	13.2
95	-0.567	29.9	30.2	31.8	36.7	37.0	8.1	13.0	13.3
105	-0.588	30.1	30.4	30.9	36.0	36.3	7.9	13.1	13.3
115	-0.609	30.3	30.6	30.0	35.3	35.6	7.8	13.1	13.4
125	-0.628	30.5	30.8	29.3	34.8	35.0	7.6	13.1	13.4
135	-0.641	30.6	30.9	28.6	34.2	34.5	7.5	13.1	13.4
145	-0.659	30.8	31.1	28.0	33.8	34.1	7.3	13.1	13.4
155	-0.677	30.9	31.2	27.5	33.4	33.7	7.2	13.1	13.4
165	-0.688	31.0	31.3	27.0	33.1	33.4	7.1	13.1	13.4
175	-0.704	31.2	31.5	26.7	32.9	33.2	6.9	13.1	13.4
185	-0.715	31.3	31.6	26.4	32.7	33.0	6.8	13.1	13.4
195	-0.730	31.4	31.7	26.2	32.6	33.0	6.7	13.1	13.4

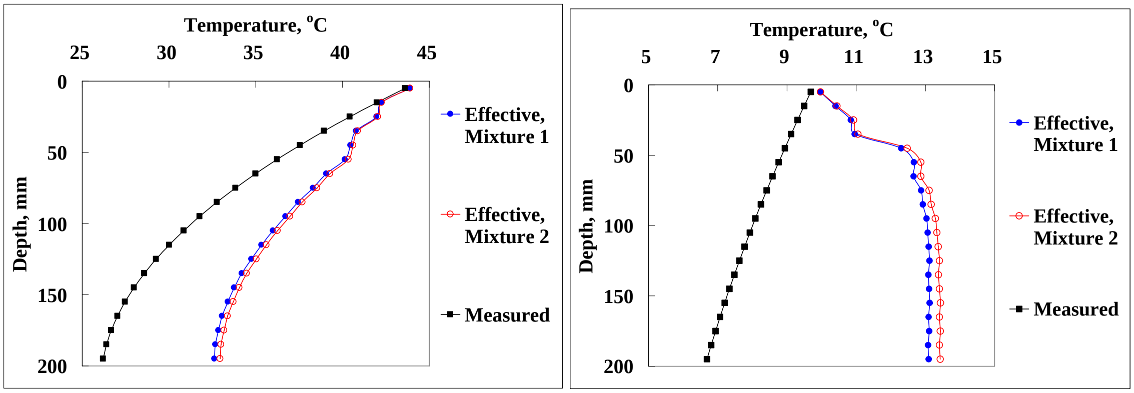

(a) Summer (b) Spring

Figure 41. Measured temperature vs. effective temperature

Pavement Response from Finite Element Analyses

The preceding finite element model has been used to generate a database of strain responses under a variety of pavement structures and loading scenarios. In mechanistic pavement response models, different response parameters such as stress, strain and deflection must be evaluated at the critical location within the pavement layer where the parameter is at its most extreme value. For a single wheel loading, the critical locations are along the vertical axis directly beneath the center of the wheel. In this study, horizontal and vertical strains were predicted using effective temperatures only at the middle of each AC layer. Some results from simulations of a moving load with a time period of 0.0358 seconds corresponding to a vehicle speed of 32 kph are presented. Figures 42 and 43 show tensile and compressive strain histories (as well as stresses) for different mixtures and seasons. Figures 42 and 43 provide a description of the viscoelastic behavior of AC materials under applied vertical stresses. The strain response contains two parts: elastic strain (resilient strain) and inelastic (residual) strain. The latter is only partly recoverable if the duration of moving load is short.

In Figures 42 and 43, the differences between strain responses from measured and effective temperatures represent the effect of loading time. In general, vertical compressive strain is much higher than horizontal tensile strain at the same depth. In the summer, the loading time has a considerable impact on both tensile and compressive strains. Consequently, a more pronounced time lag between the applied stress and the resulting strain is observed. In the spring, strain responses predicted from the effective temperature and measured temperature are almost identical. In other words, the pavement response during a cold season is barely influenced by the loading time. A possible reason is that the AC is stiffer in spring compared to summer, and therefore the impact of the loading time is less pronounced.

The preceding conclusions are applicable for both AC mixtures. For brevity, only the maximum strain responses predicted from finite element analyses are summarized in Table 47. In the summer, the loading time (difference between the measured and the effective temperature) can result in as much as 300 percent increase in tensile strain and 350 percent increase in compressive strain. However, in the spring, minimal changes in strain responses are observed. From Figure 41, it can also be concluded that Mixture 1 has better resistance to rutting than

Mixture 2 since it has a higher shear relaxation modulus under extended loading times. However, the same cannot be concluded for resistance to thermal cracking since the shear relaxation modulus at very short loading times is nearly the same for both mixtures.

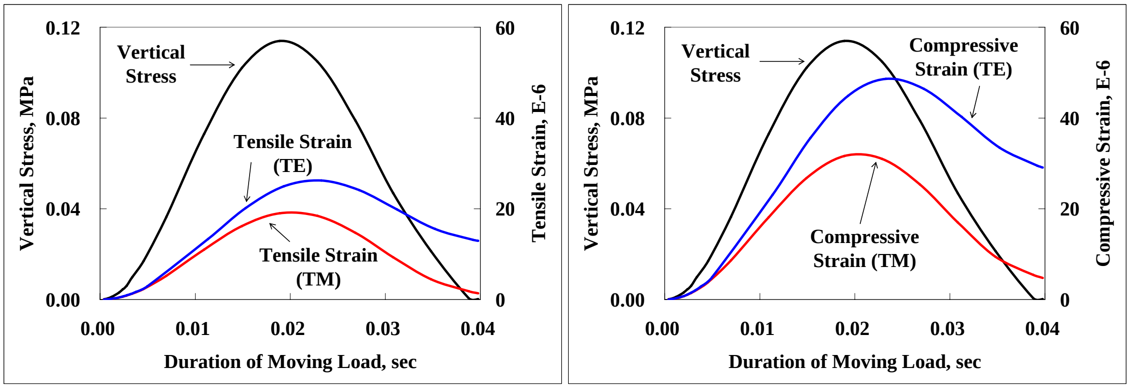

(a) Tensile Strain (b) Compressive Strain

Figure 42. Strain responses of mixture 1 at 145-mm depth in the summer

.

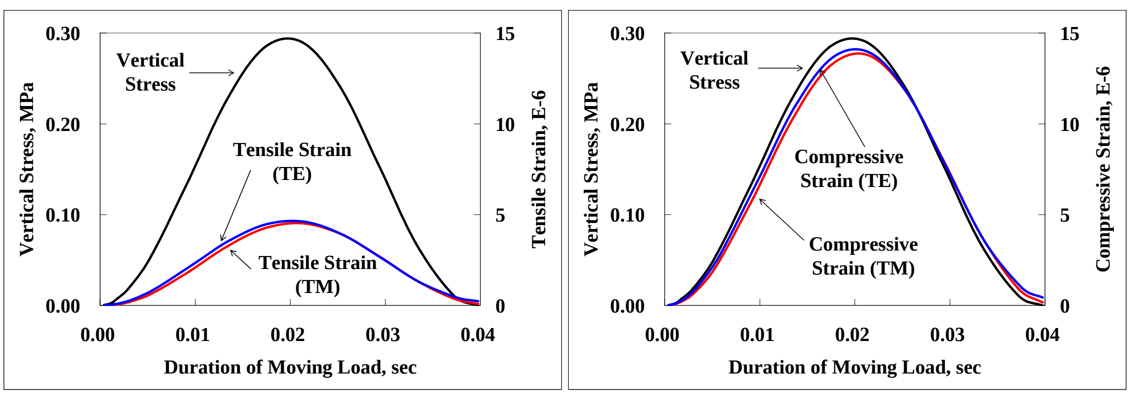

(a) Tensile Strain (b) Compressive Strain

Figure 43. Strain responses of mixture 2 at 95-mm depth in the spring

Table 47. Summary of predicted maximum strain responses

Mixture	Season	Temperature	Tensile Strain, E-6	Compressive Strain, E-6
1	summer	T_M	90	163
		T_E	282	572
	spring	T_M	26	38
		T_E	26	38
2	summer	T_M	51	75
		T_E	74	124
	spring	T_M	35	49
		T_E	37	53

Concluding Remarks

Asphalt concrete is a viscoelastic material. To properly predict flexible pavement response under moving loads, both time and temperature dependencies of AC materials have to be considered. In this paper, these two dependencies are combined through the proposed concept of effective temperature. The main characteristic of the effective temperature is addressing the time dependency of AC materials in terms of the temperature. The effective temperature contains three components: the measured temperature, the pseudo temperature, and the reference temperature. The measured temperature was collected from the field-instrumented thermocouples. Pseudo and reference temperatures reflect the effect of loading time on pavement response. These two temperatures were analytically obtained by applying the time-temperature superposition principle in both time and frequency domains. In particular, pseudo temperature is a material-dependent parameter, while reference temperature incorporates the effects of the load amplitude and vehicle speed. In the developed viscoelastic-based 3-D FE model, the effective temperature was applied to AC materials through relaxation moduli. FE analysis was conducted for two different AC mixtures in a simplified pavement structure at two different seasons. Analysis results suggest that the loading time has a more significant impact on pavement response in the summer for both pavements. This study provides some insight on how the loading time influences the dynamic response of flexible pavements. Adequate design, which can be decided based on proposed approach, will help pavement designers in making necessary changes such as using a different binder grade, thickness of layers, or a different mixture.

CHAPTER 10: SUMMARY

The SISSI data were utilized in the Mechanistic-Empirical Pavement Design Guide (MEPDG), and the predicted condition parameters were compared to those measured in the field. Overall, it was found that the MEPDG only made somewhat reasonable predictions for rutting. It is therefore essential to perform local calibration. The SISSI data provide a valuable source of both response and performance data for that purpose.

In order to further understand the sources of differences between measured and predicted performance, it is important to evaluate the differences in mechanistic responses. Therefore, independent mechanistic analysis was conducted in order to compare the responses from finite element analysis to those measured from the instrumentation in the field. In order to correct the finite element responses to correspond to field conditions under a variety of environment and loading conditions, a site-specific procedure was developed to extrapolate the results.

Finite element analysis was also utilized to model loading with the falling weight deflectometer. A comparison of the responses from embedded instrumentation devices during the FWD loading was also made. For surface deflections, the average prediction errors were 9 and 12 percent when using backcalculated and laboratory AC moduli, respectively. For the strain and stress responses, the predicted responses consistently exceeded the measured responses, with a prediction error of 30 to 50 percent.

Finally, parametric studies were conducted to examine possible sources of error in the SISSI experiment. The variation of loading pulse with depth was examined and correction procedures utilized. An additional concern was that the strain gages themselves might alter the pavement structure and affect the overall response. Therefore, detailed finite element analysis was performed to examine the potential magnitude of the strain gage effects. It was found that the strain gages might result in an error of up to about 80 percent, depending upon other conditions.

As the Pennsylvania Department of Transportation moves to adopt and implement the MEPDG, these analyses provide a basis for utilizing the SISSI data in its understanding and calibration. It will be important that reliable performance data from other sites also be used for the calibration effort.

REFERENCES

AASHO Road Test: Report 6 – Special Studies. HRB Spec. Report 61F (1962).

ABAQUS/Standard User's Manual. (2002): Finite Element Computer Program. Hibbitt, Karlsson and Sorenson, Inc., Pawtucket, RI, USA, Version 6.3.

ARA, Inc., ERES Division: APPENDIX CC-3, (2003): "Updated Traffic Frequency Calculation for Asphalt Layers." *Final Report NCHRP 1-37A, 505 West University Avenue, Champaign, IL.*

Ahlvin, R.G. and Ulery, H.H., (1962):" Tabulated Values for Determining the Complete Pattern of Stresses, Strains, and Deflections Beneath a Uniform Circular Load on a Homogeneous Half Space." *Bulletin 342*, *Highway Research Board.*

Akram, T., Scullion, T., and Smith, R. E., (1994): "Comparing Laboratory and Backcalculated Layer Moduli on Instrumented Pavement Sections." *Special Technical Publication (STP) 1298*, *ASTM, Philadelphia, PA.*

Al-Qadi, I.L., Elseifi, M., and Yoo, P.J., (2004): "Pavement Damage Due to Different Tires and Vehicle Configurations." *Final Report, Virginia Tech Transportation Institute, Blacksburg, VA.*

American Association of State Highway and Transportation Officials (AASHTO), (1993): Guide for Design of Pavement Structures, Vol. II. *Joint Task Force on Pavement, Highway Subcommittee on Design, Washington, D.C.*

Anderson, D.A., Solaimanian, M., Hunter, D. and Soltani, A., (2003): "Superpave Validation Studies: SISSI Instrumentation, Operating Instructions and Baseline Measurements." *Final Report. Pennsylvania Transportation Institute, University Park, PA.*

Beer, M., Johnson, G., Van Deusen, D., (1997): "Performance of MnRoad Load Response and Environmental Instrumentation." Presented at *76th Transportation Research Board Annual Meeting, Washington, D.C.*

Baker, H. B., Buth, M. R., and Van Deusen, D. A., (1994): "Minnesota Road Research Project: Load Response Instrumentation Installation and Testing Procedures." *Final Report, 1992-94, Report No. MN/PR-94/01, Minnesota Dept. of Transportation, Maplewood, MN.*

Bao, W., (2000): "Calibration of Flexible Pavement Structural Model Using MnRoad Field Data." MS Thesis, Department of Civil Engineering, University of Minnesota, Minneapolis, MN.

Bathe, K. J., (1982): "Finite Element Procedures in Engineering Analysis." Prentice-Hall, NJ.

Carvalho, R.L. and Schwartz, C.W., (2006): "Comparisons of Flexible Pavement Designs: AASHTO Empirical versus NCHRP Project 1-37A Mechanistic-Empirical." *Transportation Research Record*, 1947, Transportation Research Board, Washington, D.C.

Chatti, K., Kim, H.B., Yun, K.K., Mahoney, J.P. and Monismith, C.L., (1996): “Field Investigation into Effects of Vehicle Speed and Tire Pressure on Asphalt Concrete Pavement Strains.” *Transportation Research Record*, 1539, Transportation Research Board, Washington, D.C.

Chehab, G. R., (2002): “Characterization of Asphalt Concrete in Tension Using a ViscoElastoPlastic Model.” Ph.D. Dissertation, North Carolina State University, NC.

Chen, D.H., Zaman, M., Laguros, J., and Soltani, A., (1995): “Assessment of Computer Programs for Analysis of Flexible Pavement Structures.” *Transportation Research Record*, 1539, Transportation Research Board, Washington, DC.

Cho, Y.H., McCullough, B.F., and Weissmann, J., (1996): “Considerations on Finite-Element Method Application in Pavement Structural Analysis.” *Transportation Research Record,* 1539, Transportation Research Board, Washington, DC.

Colombo, D., Giglio, M., and Manes, A., (2007): “3D Fatigue Crack Propagation Analysis of a Helicopter Component.” *International Journal of Materials and Product Technology*, Vol. 30, No. 1/2/3.

Cormier, N.G., Smallwood, B.S., Sinclair, G.B., and Meda, G., (1999): “Aggressive Submodelling of Stress Concentrations.” *International Journal for Numerical Methods in Engineering*, Vol. 46, Issue 6.

Daleiden, J. F., Killingsworth, B. M., Simpson, A. L., and Zamora, R. A., (1994): “Analysis of Procedures for Establishing In-situ Subgrade Moduli.” Transportation Research Record: Journal of the Transportation Research Board, No. 1462, Transportation Research Board of the National Academies, Washington, D.C.

De Beer, M., (1996): “Measurement of Tyre/Pavement Interface Stresses under Moving Wheel Loads.” *International Journal of Vehicle Design*. Vol. 3.

De Jong, D.L., Peatz, M.G.F., and Korswagen, A. R., (1973): “Computer Program Bisar Layered System Under Normal and Tangential Loads.” Konin Klijke Shell-Laboratorium, Amsterdam, Netherlands.

ERES Consultants Division. (2004): “Guide for Mechanistic-Empirical Design of New and Rehabilitated Pavement Structures.” Final Report NCHRP 1-37A, Champaign, IL.

El-Basyouny, M.M. and Witczak, M.W., (2005): “Calibration of Alligator Fatigue Cracking Model for 2002 Design Guide.” *Transportation Research Record*, 1919, Transportation Research Board, Washington, D.C.

El-Basyouny, M.M., Witczak, M.W., El-Badawy, S., Timm, D., Dongre, R., Heitzman, M., and Dunning, R., (2005a): “Verification for the Calibrated Permanent Deformation Models for the 2002 Design Guide.” *Journal of the Association of Asphalt Paving Technologists*, Vol. 74.

Elseifi, M.A., Al-Qadi, I.L., and Yoo, P.J., (2006): "Viscoelastic Modeling and Field Validation of Flexible Pavements." *Journal of Engineering Mechanics*, Vol. 132, No. 2.

Fagan, M. J., (1992): "Finite Element Analysis: Theory and Practice." John Wiley, New York.

Fanous, F., Coree, B., and Wood, D., (1999): "Response of Iowa Pavements to Heavy Agricultural Loads." Interim Report, Department of Civil and Construction Engineering, Iowa State University, IA.

Freeman, T., Uzan, J., Zollinger, D., and Park, E., (2005): "Sensitivity Analysis of and Strategic Plan Development for the Implementation of the M-E Design Guide in TXDOT Operations." Report No. 0-4714-1, Texas Transportation Institute, College Station, TX.

Galal, K. and Chehab, G.R., (2005): "Implementation of the 2002 M-E Design Procedure Using a HMA Rehabilitated Pavement Section in Indiana." *Transportation Research Record*, 1919, Transportation Research Board, Washington, D.C.

Hjelmsted, K.D., Kim, J., and Zuo, Q., (1997): "Finite Element Procedures for Three Dimensional Pavement Analysis." Aircraft/Pavement Technology: In the Midst of Change, *Proceedings, ASCE Airfield Pavement Conference*, Seattle, WA.

Huang, Y., (1993) "Pavement Analysis and Design." Prentice Hall, NJ.

Huhtala, M., Pihlajamaki, J., (1992): "Strain and Stress Measurements in Pavements." *Proceedings, Road and Airport Pavement Response Monitoring Systems*, ASCE, West Lebanon, NH, pp. 229-243.

Irwin, L. H., (2000): "MODCOMP." *Cornell Local Roads Program, Ithaca, NY.*

Kim, S., Ceylan, H., and Heitzman, M., (2005) "Sensitivity Study of Design Input Parameters for Two Flexible Pavement Systems Using the Mechanistic-Empirical Pavement Design Guide." *Proceedings, the 2005 Mid-Continent Transportation Research Symposium*, Ames, IA.

Kuo, M. C., Hall, K. T., and Darter, M., (1995): "Three-dimensional Finite Element Model for Analysis of Concrete Pavement Support." *Transportation Research Record,* 1505, Transportation Research Board, Washington, D.C.

Lakes, R.S. and Wineman, A., (2006): "On Poisson's Ratio in Linearly Viscoelastic Solids." *Journal of Elasticity*, 85.

Li, Y. and Metcalf, J.B., (2002): "Crack Initiation Model from Asphalt Slab Tests." *Journal of Materials in Civil Engineering*, ASCE.

Loulizi, A., Al-Qadi, I. L., and Elseifi, M., (2006): "Difference Between In-situ Flexible Pavement Measured and Calculated Stresses and Strains." *ASCE Journal of Transportation Engineering*, Vol. 132, No. 7.

Loulizi, A. and Al-Qadi, I. L., (2004): "Inability of the Elastic-layered Theory to Predict Pavement Vertical Stresses." *Proceedings, 2nd International Conference on Accelerated Pavement Testing, Minneapolis*, MN.

Loulizi, A., Al-Qadi, I. L., Lahouar, S., and Freeman, T.E., (2001): "Data Collection and Management of the Instrumented Smart Road Flexible Pavement Sections." *Transportation Research Record,* 1769, Washington, DC.

Prozzi, J. and R. Luo, (2005): "Quantification of the Joint Effect of Wheel Load and Tire Pressure on Pavement Performance." *Transportation Research Record*, 1919, Transportation Research Board, Washington, D.C., pp. 134-141.

Lytton, L.R., Uzan, J., Fernando, E. G., Roque, R., Hiltunen, D., and Stoffels, S. M., (1993): "Development and Validation of Performance Prediction Models and Specifications for Asphalt Binders and Paving Mixes." SHRP-A-357 Report. Strategic Highway Research Program, National Research Council, Washington, D.C.

Masad, S.A. and Little, D. N., (2004): "Sensitivity Analysis of Flexible Pavement Response and AASHTO 2002 Design Guide for Properties of Unbound Layers." Report No. ICAR 504-1, International Center for Aggregates Research, Austin, TX.

Mikhail, M. Y., Seeds, S. B., Alvavi, S. H., and Ott, W. C., (1999): "Evaluation of Laboratory and Backcalculated Resilient Moduli from the WesTrack Experiment." *Transportation Research Record,* 1687, Transportation Research Board, Washington, D.C.

Moreno, A.M., (2000): "Load Equivalency Factors From the Structural Response of Flexible Pavements." MS Thesis, Department of Civil Engineering, University of Minnesota, MN.

Newcomb, D.E., Bu-bushait, A. A., Mahoney, J. P. and Sharma, J., (1983): "State-of-the-Art on Pavement Overlay Design Procedures. Vol. 1." Report WA-RD 65.1, Washington State Department of Transportation, Olympia, WA.

Omega Press LLC, (1996): "The Pressure, Strain, and Force Handbook."

Ongel, A. and Harvey, J., (2004): "Analysis of 30 Years of Pavement Temperatures using the Enhanced Integrated Climate Model (EICM)." Draft report prepared for the California Department of Transportation, Pavement Research Center, Institute of Transportation Studies, University of California Berkeley, University of California, Davis, CA.

Pirabaroobn, S., Zaman, M., and Tarefder, R.A., (2003): "Evaluation of Rutting Potential in Asphalt Mixes Using Finite Element Modeling." *Proceedings, Annual Conference of the Transportation Association of Canada*, St. John's, Newfoundland and Labrador, USA

Quintus, H. V. and Killingsworth, B., (1998): "Analysis Relating Pavement Material Characterizations and Their Effects on Pavement Performance." Report FHWA-RD-97-085, Federal Highway Administration, McLean, VA.

Sargand, S. M., Green, R., and Khoury, I., (1997): "Instrumentation Ohio Test Pavement." Transportation Research Record No.1596, Washington, D.C.

Schapery, R. and Park, S., (1999): "Methods of Interconversion Between Linear Viscoelastic Material Functions. Part II – An Approximate Analytical Method." *International Journal of Solids and Structures*, Vol. 36.

Schwartz, C. W., Gibson, N., and Schapery, R. A., (2002): "Time-Temperature Superposition for Asphalt Concrete at Large Compressive Strains." *Transportation Research Record*, 1789, Transportation Research Board, Washington, D.C.

Sebaaly, P. E. and Mamlouk, M., (1987): "Prediction of Pavement Response to Actual Traffic Loading." *Transportation Research Board*, Washington, D.C.

Sebaaly, P.E., Tabatabaee, N., (1991): "Field Evaluation of Strain Gauges in Asphalt Concrete Pavements." *Proceedings, Second International Symposium on Pavement Response Monitoring Systems for Road and Airfields*, ASCE, Hanover, NH.

Shoukry, S., (1998a): "3D Finite Element Modeling for Pavement Analysis and Design." *Proceedings, First National Symposium on 3D Finite Element Modeling for Pavement Analysis and Design*, Charleston, WV.

Siddharthan, Raj V., Krishnamenon, N., El-Mously, M., and Sebaaly, Peter E., (2002): "Investigation of Tire Contact Stress Distributions on Pavement Response." *Journal of Transportation Engineering*, Vol. 128, Issue 2.

Solaimanian, M., Hunter, D., and Stoffels, S. M., (2006): "Design and Construction Report for Superpave In-Situ Stress-Strain Instrumentation Sites, State Route 1001, Blair County, Pennsylvania." Final Report. Pennsylvania Transportation Institute, University Park, PA.

Solaimanian M., Hunter, D.A., Shah, J., and Stoffels, S. M., (2006): Characterization of Materials for Superpave In-Situ Stress/Strain Investigation. Final Report, Pennsylvania Transportation Institute, University Park, PA.

Solaimanian, M., Stoffels, S.M., Hunter, D.A., Morian, D., Sadasivam, S., Yin, H., (2006): "Detailed Final Report for Superpave In-Situ Stress/Strain Investigation." Pennsylvania Transportation Institute*, PA.*

Stoffels, S. M., Solaimanian M., and Morian, D., (2006): Seasonal Variations for Superpave In-Situ Stress/Strain Investigation. Final Report, Pennsylvania Transportation Institute, University Park, PA.

Stolle, D., and Hein, D., (1989): "Parameter Estimates of Pavement Structure Layers and Uniqueness of the Solution. In Nondestructive Testing of Pavements and Backcalculation of Moduli." *Special Technical Publication (STP)*, 1026, ASTM, Philadelphia, PA.

Timm, D. H., Bower, J. M., and Turochy, R. E., (2006): "Effect of Load Spectra on Mechanistic-Empirical Flexible Pavement Design." *Transportation Research Record*, 1947, Transportation Research Board, Washington, D.C.

Timm, D. H., Priest, A. L., and McEwen, T. V., (2004): "Design and Instrumentation of The Structural Pavement Experiment at The NCAT Test Track." NCAT Report 04-01. National Center for Asphalt Technology, Auburn University, Auburn, AL.

Timm, D. H. and Newcomb, D. E., (2003): "Calibration of Flexible Pavement Performance Equations." *Transportation Research Record*, 1853, Transportation Research Board, Washington, D.C.

Uddin, W., (1998): "Application of 3D Finite Element Dynamic Analysis for Pavement Evaluation." *Proceedings, First National Symposium on 3D Finite Element Modeling for Pavement Analysis and Design*, Charleston, WV.

Wang, J,. (2001): "Three-Dimensional Finite Element Analysis of Flexible Pavements." MS Thesis, Department of Civil Engineering, University of Maine, ME.

Whitcomb, J. D. and Woo, K., (1993): "Application of Iterative Global/Local Finite Element Analysis, Part 1: Linear Analysis." *Communications in Numerical Methods in Engineering*, Vol. 9.

White, T., (1998): "Application of Finite Element Analysis to Pavement Problems." *Proceedings, First National Symposium on 3D Finite Element Modeling for Pavement Analysis and Design*, Charleston, WV.

Wu, Z. and Hossain, M., (2003): "Pilot Instrumentation of A Superpave Test Section at the Kansas Accelerated Testing Laboratory." Final Report, Report No. KTRAN: KSU-98-2, Department of Civil Engineering, Kansas State University, Manhattan, KS.

Yin, H., Solaimanian, M., Kumar, T., and Stoffels, S., (2008): "The Effect of Loading Time on Flexible Pavement Dynamic Response: A Finite Element Analysis." *Journal of Mechanics of Time-Dependent Materials*, January, PP. 265-288.

Yin, H., Stoffels, S., Solaimanian, M., (2008): "Optimization of Asphalt Pavement Modeling Based on the Global-Local 3D FEM Approach." *Journal of Road Materials and Pavements Design*. Volume 9, Issue 2.

Yin, H., (2007) “Integrating Instrumentation Data in Probabilistic Performance Prediction of Flexible Pavements”. Ph.D. Dissertation. The Pennsylvania State University, University Park, PA.

Yin, H., Chehab, G., and Stoffels, S., (2006): “Sensitivity of Thermal Cracking Prediction to AC Mixture Properties Using the M-E Pavement Design Guide.” *Proceedings, 10th International Conference on Asphalt Pavements*, Quebec, Canada.

Yin, H., Chehab, G., and Stoffels, S., (2006): “A Case Study: Assessing the Sensitivity of the Coefficient of Thermal Contraction of AC Mixtures on Thermal Crack Prediction.” *ASCE Geotechnical Special Publication,* No.146.

Zaghloul, S. M., and White, T. D., (1993): “Use of a Three-dimensional, Dynamic Finite Element Program for Analysis of Flexible Pavement.” *Transportation Research Record,* 1388, Transportation Research Board, Washington, D.C.

Zhou, H., (2000): “Comparison of Backcalculated and Laboratory Measured Moduli on AC and Granular Base Layer Materials.” *Nondestructive Testing of Pavements and Backcalculation of Moduli,* Third Volume, ASTM STP 1375, West Conshohochen, PA.

Appendix A – Dynamic Modulus

Table A-1. Summary of adjusted |E*| values of Tioga site, MPa

AC layer	Temperature, °C	Frequency, Hz					
		0.1	0.5	1	5	10	25
Wearing	-10	16808	18598	19329	20925	21566	22372
	4	8863	10841	11705	13707	14557	15660
	20	2865	4180	4827	6493	7269	8337
	40	743	1338	1674	2656	3167	3921
	52	271	570	758	1360	1699	2228
Binder	-10	13361	14150	14443	15030	15247	15502
	4	9715	11051	11573	12657	13070	13568
	20	2777	4182	4843	6439	7131	8032
	40	501	1105	1468	2548	3106	3911
	52	111	343	514	1128	1495	2077
BCBC	-10	24025	25706	26346	27650	28140	28726
	4	11701	14553	15753	18412	19485	20828
	20	4542	6882	8005	10777	12007	13636
	40	849	1824	2409	4166	5084	6427
	52	206	593	871	1861	2453	3396

Table A-2. **Summary of adjusted |E*| values of Mercer East site, MPa**

AC layer	Temperature, °C	Frequency, Hz					
		0.1	0.5	1	5	10	25
Wearing	-10	13673	15097	15672	16917	17412	18030
	4	8598	10252	10957	12550	13211	14055
	20	2189	3273	3810	5197	5845	6736
	40	506	962	1228	2019	2437	3058
	52	165	378	516	979	1248	1672
Binder	-10	22692	25267	26316	28601	29517	30663
	4	10451	13209	14434	17306	18537	20143
	20	3195	4898	5759	8022	9095	10586
	40	679	1338	1731	2931	3579	4558
	52	209	499	694	1363	1760	2400
BCBC	-10	24624	26382	27061	28465	29000	29648
	4	14061	16800	17938	20440	21448	22708
	20	5292	7643	8752	11465	12665	14253
	40	1263	2407	3054	4906	5843	7191
	52	392	936	1290	2449	3102	4106

Table A-3. **Summary of adjusted |E*| values of Mercer West site, MPa**

AC layer	Temperature, °C	Frequency, Hz					
		0.1	0.5	1	5	10	25
Wearing	-10	20382	22651	23573	25574	26373	27372
	4	9054	11509	12601	15165	16265	17700
	20	2896	4444	5225	7273	8242	9586
	40	609	1207	1564	2657	3246	4135
	52	185	446	623	1230	1592	2173
Binder	-10	16464	18701	19614	21601	22396	23388
	4	7442	9722	10746	13159	14197	15550
	20	1327	2346	2905	4478	5266	6397
	40	158	406	578	1182	1545	2133
	52	71	165	261	666	946	1443
BCBC	-10	17814	19434	20072	21416	21937	22575
	4	8396	10537	11464	13577	14457	15581
	20	2836	4355	5106	7029	7915	9118
	40	551	1146	1504	2598	3182	4054
	52	148	393	565	1169	1532	2115

Table A-4. **Summary of adjusted |E*| values of Warren site, MPa**

AC layer	Temperature, °C	Frequency, Hz					
		0.1	0.5	1	5	10	25
Wearing	-10	16562	18820	19743	21751	22554	23557
	4	7419	9711	10741	13173	14220	15586
	20	1327	2350	2910	4490	5282	6419
	40	158	405	577	1182	1546	2135
	52	75	103	163	416	591	901
Binder	-10	17682	19273	19899	21216	21725	22349
	4	8429	10554	11471	13558	14426	15532
	20	2838	4354	5104	7018	7898	9093
	40	552	1148	1507	2600	3184	4055
	52	148	393	565	1171	1534	2118
BCBC	-10	19093	20675	21285	22545	23023	23601
	4	9542	11896	12894	15122	16029	17169
	20	2911	4616	5464	7627	8616	9950
	40	466	1069	1449	2646	3298	4278
	52	101	316	479	1093	1478	2112

Table A-5. **Summary of adjusted |E*| values of Perry site, MPa**

AC layer	Temperature, °C	Frequency, Hz					
		0.1	0.5	1	5	10	25
Wearing	-10	16578	18133	18757	20097	20628	21287
	4	8701	10597	11416	13289	14073	15082
	20	3120	4508	5179	6878	7655	8711
	40	814	1469	1836	2897	3442	4237
	52	291	622	829	1493	1864	2437
Binder	-10	20813	22941	23800	25654	26391	27309
	4	10310	12774	13851	16338	17390	18750
	20	3407	5073	5897	8017	9003	10357
	40	796	1508	1920	3144	3788	4745
	52	262	596	813	1535	1951	2608
BCBC	-10	20813	22941	23800	25654	26391	27309
	4	10310	12774	13851	16338	17390	18750
	20	3407	5073	5897	8017	9003	10357
	40	796	1508	1920	3144	3788	4745
	52	262	596	813	1535	1951	2608

Table A-6. **Summary of adjusted |E*| values of Delaware site, MPa**

AC layer	Temperature, °C	Frequency, Hz					
		0.1	0.5	1	5	10	25
Wearing	-10	22719	24672	25445	27083	27723	28510
	4	12651	15238	16337	18807	19825	21119
	20	4416	6405	7361	9756	10841	12303
	40	1099	2036	2565	4094	4878	6018
	52	369	829	1122	2070	2605	3431
Binder	-10	26088	28782	29867	32202	33127	34277
	4	12596	15728	17100	20271	21612	23346
	20	4027	6101	7135	9811	11062	12782
	40	873	1712	2208	3703	4499	5690
	52	268	642	892	1744	2245	3044

Table A-7. **Summary of adjusted |E*| values of Somerset site, MPa**

AC layer	Temperature, ^oC	Frequency, Hz					
		0.1	0.5	1	5	10	25
Wearing	-10	26799	29161	30090	32047	32806	33735
	4	15715	19248	20754	24145	25541	27314
	20	5071	7654	8920	12131	13600	15587
	40	1056	2128	2761	4662	5664	7147
	52	302	764	1081	2168	2809	3827
Binder	-10	26791	28987	29838	31603	32277	33093
	4	14189	17410	18769	21791	23019	24562
	20	4437	6850	8034	11032	12394	14227
	40	807	1742	2311	4057	4989	6375
	52	198	563	827	1778	2355	3286
BCBC	-10	24850	27862	29095	31789	32873	34232
	4	10791	14109	15617	19221	20794	22868
	20	3418	5391	6407	9122	10427	12258
	40	655	1351	1778	3119	3859	4993
	52	187	472	670	1378	1810	2519

Table A-8. **Summary of adjusted |E*| values of Blair site, MPa**

AC layer	Temperature, ^oC	Frequency, Hz					
		0.1	0.5	1	5	10	25
Wearing	-10	21696	24906	26258	29290	30541	32138
	4	9103	11908	13198	16328	17714	19564
	20	2127	3459	4169	6131	7107	8510
	40	384	806	1071	1930	2419	3185
	52	109	275	393	822	1091	1541
Binder	-10	22448	25746	27131	30231	31508	33134
	4	9527	12548	13942	17329	18831	20837
	20	2290	3744	4519	6666	7735	9270
	40	403	856	1143	2076	2608	3445
	52	111	287	412	874	1165	1653
BCBC	-10	20154	23896	25502	29165	30698	32673
	4	8718	12160	13809	17953	19846	22421
	20	1367	2529	3200	5202	6264	7852
	40	155	398	572	1209	1609	2279
	52	73	172	271	695	997	1545

Appendix B – Creep Compliance and Tensile Strength

Table B-1. Summary of creep compliance and tensile strength of Tioga site

Time, sec	Creep Compliance, 1/MPa			Tensile Strength @ -10^{o}C, MPa
	-20^{o}C	-10^{o}C	0^{o}C	
1	5.0E-05	5.7E-05	7.6E-05	4.2
2	5.1E-05	5.9E-05	8.2E-05	
5	5.3E-05	6.3E-05	9.2E-05	
10	5.5E-05	6.7E-05	1.0E-04	
20	5.6E-05	7.1E-05	1.1E-04	
50	6.0E-05	7.8E-05	1.4E-04	
100	6.2E-05	8.4E-05	1.6E-04	

Table B-2. Summary of creep compliance and tensile strength of Mercer East site

Time, sec	Creep Compliance, 1/MPa			Tensile Strength @ -10^{o}C, MPa
	-20^{o}C	-10^{o}C	0^{o}C	
1	5.4E-05	5.9E-05	8.3E-05	4.9
2	5.5E-05	6.2E-05	9.0E-05	
5	5.8E-05	6.6E-05	1.0E-04	
10	6.1E-05	7.0E-05	1.1E-04	
20	6.3E-05	7.5E-05	1.3E-04	
50	6.8E-05	8.2E-05	1.5E-04	
100	7.2E-05	9.0E-05	1.8E-04	

Table B-3. Summary of creep compliance and tensile strength of Mercer West site

Time, sec	Creep Compliance, 1/MPa			Tensile Strength @ -10^{o}C, MPa
	-20^{o}C	-10^{o}C	0^{o}C	
1	4.9E-05	5.7E-05	8.0E-05	5.1
2	5.1E-05	6.0E-05	8.8E-05	
5	5.3E-05	6.5E-05	1.0E-04	
10	5.6E-05	7.0E-05	1.1E-04	
20	5.9E-05	7.6E-05	1.3E-04	
50	6.3E-05	8.5E-05	1.6E-04	
100	6.8E-05	9.4E-05	1.9E-04	

Table B-4. **Summary of creep compliance and tensile strength of Warren site**

Time, sec	Creep Compliance, 1/MPa			Tensile Strength @ -10°C, MPa
	-20°C	-10°C	0°C	
1	6.4E-05	8.2E-05	1.2E-04	4.4
2	6.6E-05	8.7E-05	1.3E-04	
5	7.0E-05	9.6E-05	1.5E-04	
10	7.4E-05	1.0E-04	1.7E-04	
20	7.8E-05	1.2E-04	2.0E-04	
50	8.5E-05	1.3E-04	2.5E-04	
100	9.1E-05	1.5E-04	3.0E-04	

Table B-5. **Summary of creep compliance and tensile strength of Perry site**

Time, sec	Creep Compliance, 1/MPa			Tensile Strength @ -10°C, MPa
	-20°C	-10°C	0°C	
1	3.4E-05	3.7E-05	5.3E-05	5.3
2	3.5E-05	3.9E-05	5.9E-05	
5	3.7E-05	4.2E-05	7.0E-05	
10	3.8E-05	4.5E-05	8.1E-05	
20	4.1E-05	4.9E-05	9.4E-05	
50	4.5E-05	5.7E-05	1.2E-04	
100	4.9E-05	6.4E-05	1.4E-04	

Table B-6. **Summary of creep compliance and tensile strength of Delaware site**

Time, sec	Creep Compliance, 1/MPa			Tensile Strength @ -10°C, MPa
	-20°C	-10°C	0°C	
1	3.6E-05	4.0E-05	4.2E-05	5.7
2	3.7E-05	4.2E-05	4.5E-05	
5	3.7E-05	4.4E-05	5.0E-05	
10	3.8E-05	4.7E-05	5.5E-05	
20	3.9E-05	5.2E-05	6.3E-05	
50	4.2E-05	6.0E-05	7.8E-05	
100	4.4E-05	6.9E-05	9.5E-05	

Table B-7. **Summary of creep compliance and tensile strength of Somerset site**

Time, sec	Creep Compliance, 1/MPa			Tensile Strength @ -10°C, MPa
	-20°C	-10°C	0°C	
1	4.4E-05	5.0E-05	7.5E-05	4.8
2	4.5E-05	5.3E-05	8.3E-05	
5	4.7E-05	5.7E-05	9.6E-05	
10	4.9E-05	6.0E-05	1.1E-04	
20	5.1E-05	6.5E-05	1.3E-04	
50	5.4E-05	7.2E-05	1.5E-04	
100	5.8E-05	8.0E-05	1.8E-04	

Table B-8. **Summary of creep compliance and tensile strength of Blair site**

Time, sec	Creep Compliance, 1/MPa			Tensile Strength @ -10°C, MPa
	-20°C	-10°C	0°C	
1	2.8E-05	3.3E-05	4.2E-05	5.5
2	2.8E-05	3.5E-05	4.7E-05	
5	3.0E-05	3.9E-05	5.5E-05	
10	3.1E-05	4.2E-05	6.3E-05	
20	3.2E-05	4.6E-05	7.4E-05	
50	3.5E-05	5.4E-05	9.6E-05	
100	3.8E-05	6.3E-05	1.2E-04	